2022

Tumor Suppression by a TRNA Synthetase

Maria Passarelli

TUMOR SUPPRESSION BY A TRNA SYNTHETASE

A Thesis Presented to the Faculty of
The Rockefeller University
in Partial Fulfillment of the Requirements for
the degree of Doctor of Philosophy

by
Maria Passarelli
June 2022

TUMOR SUPPRESSION BY A TRNA SYNTHETASE

Maria Passarelli, Ph.D.
The Rockefeller University 2022

Despite substantial progress in treatment, breast cancer remains a leading cause of cancer mortality among women. During malignant transformation, healthy mammary cells must bypass tumor suppressive checkpoints and activate pro-growth pathways. Enhanced protein translation is one such hallmark of tumor transformation and cancer progression; many oncogenes promote translation by driving synthesis and activity of translational machinery.

In the first part of this thesis, we report the surprising finding that leucyl-tRNA synthetase (LARS), a tRNA synthetase responsible for ligating leucine to corresponding leucyl-tRNAs, becomes strongly repressed during mammary cell transformation and in breast cancer. Monoallelic genetic inactivation of LARS in mouse mammary glands enhanced tumor formation and proliferation. LARS repression reduced the abundance of specific leucyl-tRNA isoacceptors tRNA-Leu^{CAG}, tRNA-Leu^{AAG} and tRNA-Leu^{TAG}. This repression resulted in decreased leucine codon-dependent translation and expression of key leucine-rich, growth suppressive genes. We uncovered two candidate tumor suppressor genes, EMP3 and GGT5, that act downstream of LARS. This work uncovers a tumor suppressive tRNA synthetase and reveals that its repression, along with its downstream tRNAs, can modulate translation to enhance breast tumorigenesis and proliferation in a codon-dependent manner.

Modulation of translation by tRNAs and their associated factors can affect not only cancer transformation, but also normal cell physiology. In the second half of this thesis, we describe work on mammary epithelial cells which, in the context of oxidative stress, exhibited a stress-

induced tRNA fragmentation response. Though tRNA fragmentation is classically not thought to occur at high enough levels to deplete mature tRNA pools, we demonstrated that tyrosyl-tRNA fragmentation depleted mature tRNA-Tyr^{GUA} following 24 hours of oxidative stress. tRNA-Tyr^{GUA} depletion was sufficient to reduce translation and expression of growth-promoting, tyrosine-enriched transcripts in a codon-dependent manner, contributing to the restriction of cell growth in response to stress. We further demonstrated that the tRNA fragment, tRF-Tyr^{GUA}, was generated in a DIS3L2 exoribonuclease-dependent manner and acted in *trans* with RNA binding proteins, including HNRNPA1, to inhibit HNRNPA1-mediated transcript destabilization. These findings uncover and characterize a second adaptive, codon-based regulatory response that can contribute to cellular stress responses in physiology and disease.

To family and friends, supporting my scientific endeavors as relentlessly as I pursued them

ACKNOWLEDGMENTS

Words cannot describe the gratitude I feel for all those who made this journey, and these discoveries, possible.

I'd first like to thank Sohail Tavazoie, for welcoming me with open arms into the lab and allowing me the freedom to pursue my ideas, even when they took many twists and turns. Thanks for giving me the opportunity to learn how to rigorously execute a scientific project, how to ask the right questions, and how to mentor other lab members and technicians in that regard. Finally, thank you for encouraging me when I needed a reminder that I DID have it in me to accomplish all that I did.

Thank you to everyone in the Tavazoie lab, for providing the best kind of support I could've asked for in lab colleagues. Thank you for showing up to the social outings I planned, for eating my cakes when we celebrated birthdays. And for your scientific support, over coffee or drinks or lunch. I need to give a special shout out to Alexandra Pinzaru, my chief conspirator and consultant in publishing this project. Thanks also to King Faisal Yambire, the most fun of collaborators as we worked side by side through some tricky experiments that the reviewers insisted on.
I'm also grateful for Maria Liberti's help with some critical metabolomics studies, as well as to Lisa Noble and Doowon Huh, two very important mentors who helped me get my feet on the ground as I started in the lab.

This project would not have been possible without our collaborators: First, to Hani Goodarzi and his lab at UCSF, especially Hosseinali Asgharian, thank you for all of your help with sequencing and translation analyses. Your insights into what 'omics' can do in the field of translation helped these projects evolve tremendously, and we're very grateful for your expertise. Thank you also to Henrik Molina and Søren Heissel at the Rockefeller University Proteomics Resource Center, for their assistance with performing and analyzing proteomics by Label Free Quantitation and by Tandem Mass Tag.

Thank you also to Josh Mendell for generously providing the HEK293T DIS3L2 knockout cells, as well as to Cori Bargmann and the Bargmann laboratory for generous help on *C. elegans* work as well as providing the RNAi clones used for tyrosyl-tRNA studies.

We thank the Rockefeller University resource venters: Alison North and staff at the Bio-Imaging Resource Center, Connie Zhao and Cristine Lai form the Genomics Resource Center, Vaughn Francis from the Comparative Bioscience Center and the veterinary staff for animal husbandry and care.

Finally, thanks to the stalwart guidance of my thesis committee: my chair, Kivanc Birsoy, Charlie Rice, and Ping Chi. I've appreciated all of the scientific and career advice that each of you have offered me. Thank you all for joining my mentorship team and encouraging me, through committee meetings and otherwise, to become the strongest physician-scientist I can be. Thank you also to Siavash Kurdistani, for joining us from the west coast as my external examiner for this thesis defense.

Thank you also to the Tri-Institutional MD-PhD program: our funding (T32GM007739) and my F30 (1F30CA247026-01), as well as the unwavering support of the program leadership and students. Catharine, Ben, Hanna, Renee, Kathy, Ruthie and Olaf: thanks for all of the encouragement, support, questions answered, and candy offered in the bottomless bowl in the office (and sometimes hand delivered!).

Finally, some personal notes: to my fellow MD-PhD classmates, thanks for the late night chats, the after-work drinks, and the innumerable hikes, ski trips and other adventures around NYC to break up the weeks and to put life into perspective. This journey has truly been so much more fun because we're on it together. To my family; from dad, letting me tag along on the LIRR to start my scientific journey at Rockefeller as a high school student, to the whole family understanding my extra work hours and holiday schedules built around animal experiments. I'm incredibly grateful for how unconditionally you listened and supported me through this journey, and consider myself so lucky that you're here to celebrate with me. And to my partner, Andrew Griswold: thank you for always lifting me up, for supporting and encouraging me to be the very best version of myself. I wouldn't be where I am without you today.

TABLE OF CONTENTS

LIST OF FIGURES

LIST OF TABLES

LIST OF ABBREVIATIONS

aaRS – Aminoacyl tRNA Synthetase

AARS – Alanyl-tRNA Synthetase

ANG - Angiogenin

ANOVA – Analysis Of Variance

ARM-Seq – AlkB-facilitated RNA Methylation Sequencing

ASNS – Asparagine Synthetase

ATM – Ataxia Telangiectasia Mutated

ATP – Adenosine Triphosphate

ATR – ATM and Rad3 Related

BCKD – Branched Chain Ketoacid Dehydrogenase

C57BL/6 – C57 Black 6

CLIP-Seq – Crosslinking Immunoprecipitation-Sequencing

CLP1 – Cleavage Factor Polyribonucleotide Kinase Subunit 1

CRISPRi – CRISPR (Clustered Regularly Interspersed Short Palindromic Repeats) Interference

DARS – Aspartyl-tRNA Synthetase

DIRICORE – Differential Ribosome Codon Reading

DIS3L2 - DIS3 Like 3'-5' Exoribonuclease 2

DM-tRNAseq – Demethylase tRNA Sequencing

DNA – Deoxyribonucleic Acid

EGF – Epidermal Growth Factor

eIF4A – Eukaryotic Initiation Factor-4A

eIF4E – Eukaryotic Initiation Factor-4E

EMP3 – Epithelial Membrane Protein 3

EPCAM – Epithelial Cell Adhesion Molecule

ERBB2 – Erythroblastic Oncogene B 2

GAPDH – Glyceraldehyde-3-Phosphate Dehydrogenase

GARS – Glycyl-tRNA Synthetase

GCN2 – General Control Nonderepressible 2

GGT5 – Gamma Glutamyl Transferase Proenzyme 5

GO – Gene Ontology

H_2O_2 – Hydrogen Peroxide

HARS – Histidyl-tRNA Synthetase

HITS-CLIP – High Throughput Sequencing – Cross-Linking Immunoprecipitation

HLA – Human Leukocyte Antigen

hnRNPA0 – Heterogeneous Nuclear Ribonucleoprotein A0

hnRNPA1 – Heterogeneous Nuclear Ribonucleoprotein A1

HSC70 – Heat Shock Cognate 71 kDa Protein

IARS – Isoleucyl-tRNA Synthetase

KARS – Lysyl-tRNA Synthetase

LARS – Leucyl-tRNA Synthetase

Leu – Leucine

LNA – Locked Nucleic Acid

MARS – Methionyl-tRNA Synthetase

MMTV-PyMT – Mouse Mammary Tumor Virus – Polyoma Middle-T Antigen

mRNA – Messenger RNA

MSC – Multi-Synthetase Complex

mTOR – Mammalian Target Of Rapamycin

$NaIO_4$ – Sodium Periodate

NARS – Asparaginyl-tRNA Synthetase

PAR-CLIP – Photoactivatable Ribonucleoside-enhanced Cross-linking and Immunoprecipitation

PCR – Polymerase Chain Reaction

PFT – pifithrin-α

PI3K – Phosphatidylinositol-3-Kinase

PNK – Polynucleotide Kinase

PyMT – Polyoma Middle-T

QARS – Glutamyl-tRNA Synthetase

qRT-PCR – Real Time Quantitative Reverse Transcription PCR

RBP – RNA Binding Protein

RELL1 – Receptor Expressed in Lymphoid-Like Tissues 1

RNA – Ribonucleic Acid

RNAi – RNA Interference

RNases - Ribonucleases

RPF – Ribosome Protected Fragment

RT – Reverse Transcriptase

SCD – Stearoyl-CoA Desaturase

SDS-PAGE – Sodium Dodecyl Sulfate Polyacrylamide Gel Electrophoresis

Ser - Serine

shRNA – Short Hairpin RNA

SLFN11 – Schlafen 11

SSB – Sjögren Syndrome Antigen B

TCA – Tricarboxylic Acid

TCGA – The Cancer Genome Atlas

TGIRT-Seq – Thermostable Template-Switching Group II Intron RT Sequencing

Thr – Threonine

TMT – Tandem Mass Tag

tRF – tRNA fragment

tRNA – Transfer Ribonucleic Acid

TSC2 – Tuberous Sclerosis Complex 2

TSEN2 – tRNA Splicing Endonuclease Subunit 2

Tyr – Tyrosine

USP3 – Ubiquitin Specific Protease 3

UTR – Untranslated Region

VE-cadherin – Vascular Endothelial Cadherin

WARS – Tryptophanyl-tRNA Synthetase

WT – Wild-Type

YAMAT-Seq – Y-shaped Adapter-ligated Mature tRNA sequencing

YARS – Tyrosyl-tRNA Synthetase

YBX1 – Y-box Binding Protein 1

CHAPTER 1. Introduction

1.1 Breast cancer: a consistent leading cause of cancer mortality

1.1.1 Cellular changes facilitating breast tumorigenesis

Despite advances in therapeutics, breast cancer remains a leading cause of cancer mortality among US women; in 2020, breast cancer was the second most common cause of cancer-related deaths[1]. Its high incidence and continued mortality rate highlight a need for study of mammary transformation and the genetic changes that preclude it. Studies of this kind remain crucial, as they lay the foundation for novel therapeutic strategies to prevent and treat breast cancer.

To initiate and progress to malignancy, healthy cells typically undergo a myriad of cellular changes to both evade physiologic anti-tumor barriers and promote growth through enhanced metabolism, nutrient uptake, and overall cellular fitness. At minimum, successful transformation typically involves induction of one or several pro-growth oncogenes, as well as inhibition of growth-inhibitory tumor suppressor genes such as p53[2–4]. A third critical step involves reactivation of telomerase, to avoid replicative senescence due to over-shortening of DNA strands during replication[3]. This combination of changes enables replicative immortality.

Oncogenes and tumor suppressor genes can exert their respective pro- and anti-tumor effects through a variety of pathways and mechanisms. These include pathways related to cellular metabolism, nutrient uptake, interaction with the tumor microenvironment and immune system, cell death resistance, and induction of angiogenesis[3].

1.1.2 Evolution of experimental breast cancer modeling: from 2-dimensional culture to genetic mouse models

During malignant transformation, healthy cells must overcome a myriad of physiological barriers, in the realms of bypassing anti-tumor checkpoints and gain of functions that improve growth opportunities and survival under stress conditions. Many models exist that facilitate study of such tumor suppressor genes and oncogenes. In principle, study of these processes can simply and rapidly be conducted *in vitro* using immortalized, transformed cancer cell lines, and a variety of cancer cell lines and *in vitro* assays have been developed and optimized to this end. Classical cancer biology experiments include transformation experiments, in which immortalized mammary epithelial cell lines were infected with oncogenes and rendered p53-null, to facilitate transformation[5–8]. Transformation competence could be assessed by colony formation in 2-dimensions on low-attachment plates or in soft agar, and allowed for identification of signaling pathways that enhanced mammary transformation downstream of induced oncogenes[7–9]. A major limitation of these approaches, however, is the inability of 2-dimensional cell culture in liquid media to mimic the physiologic tumor microenvironment in which cells must transform and progress in a human host.

More recent advances in 3-dimensional organoid cell culture approaches overcome some of these limitations[10–13]. In principle, organoids are cultured in 3-dimensional Matrigel domes with supplemental growth factors, allowing for more physiologic structures to form in culture. This approach has shown promise in propagating and studying not only primary human tissue structures[11,14,15], but also in patient and mouse-derived tumor samples[16–20]. Three-dimensional culture offers many advantages in breast cancer, including the opportunity for formation of more

physiologic ductal structures from cell clusters, as well as for three-dimensional co-culture experiments and visualization of the interaction of cancer cells with other factors and cell types in the microenvironment.

Still, the gold standard for tumor modeling warrants *in vivo* animal studies. Typically conducted in mice, these often complementary experiments fall into three main categories; xenograft, syngeneic and genetically initiated tumor models[21]. Xenograft experiments involve transplantation of human cancer cells into immune-compromised mice to monitor *in vivo* growth and progression. An immune compromised animal is required to avoid haplotype rejection of human cells on the basis of HLA mismatch. While useful in modeling human cancer *in vivo*, these studies are limited in their ability to dissect the role of immune evasion and the tumor immune microenvironment in cancer cell growth and progression. For this reason, xenograft studies are often conducted in parallel with syngeneic transplantation experiments. In a syngeneic experiment, murine-derived tumor cells are transplanted into mice of the same genetic background as the original host, to avoid HLA mismatch and immune rejection of the transplant. Another limitation of all transplantable *in vivo* tumor modeling is the steps of oncogenic progression that can be monitored; though transplantation of cancer cell lines into an animal – particularly orthotopic studies, with cellular transplant in the organ of origin - easily facilitates studies of gene manipulation on tumor growth, invasive potential, and other downstream factors related to cellular metastatic fitness, it is comparatively difficult to study tumor initiation or transformation in this context. For this purpose, genetically initiated mouse models of cancer exist, where mice harbor a transgene that will spontaneously or inducibly result in formation of primary tumors[22–25]. These models, though more time-consuming than transplantable studies,

easily facilitate study of tumor formation and progression from inception, and are thus a critical tool in the examination of transformation.

In breast cancer, the most commonly used genetically initiated model for breast cancer is the MMTV-PyMT model[24], driven by the polyomavirus middle-T antigen, facilitating tumor initiation at up to 10 distinct mammary fat pads as early as 12 weeks of age in C57/BL6 mice. Spontaneous lung metastases form from these tumors at up to 24 weeks in age, enabling study of gene deletion on tumor initiation, growth and metastatic potential within the same experiment. Therefore, these models can offer powerful evidence of gene manipulation in cancer transformation and progression.

1.2 Protein translation is a coordinately (dys)regulated process in cancer transformation

The role of protein translation in cellular transformation and oncogenic progression has been extensively explored[26–28]. In general, enhanced translation is found to be positively correlated with cellular oncogenic potential. Enhanced global translation in tumorigenesis occurs through a few mechanisms: enhancement of signaling pathways such as mTOR to upregulate global translation[29–31], direct phosphorylation and activation of translation machinery components directly to bypass control checkpoints, such as eIF4A[32], eIF4E phosphorylation[33], and direct mutation or alteration in ribosomal component availability[34]. Though processes targeting initiation have been closely studied, some groups have also implicated translation elongation as a crucial regulatory step in transformation[35].

Intriguingly, modulation of translation can also occur through alteration of available resources for the process, such as tRNAs[36,37]. Notably, Gingold et al. found that differential tRNA

availability facilitated a proliferative program compared to a differentiation program within cells, based on codon usage across genes[36]. This work further suggests that tRNAs can coordinately regulate specific translation programs. By extension, translation may also be uniquely controlled by a variety of other physiologic factors that directly affect available tRNA pools, including regulation of tRNA charging and amino acid availability[38–41]. In some notable examples, Gobet et al. correlate ribosome dwell times with availability of charged tRNA and overall codon usage within the genome, demonstrating that increased dwell time can be either explained by high levels of codon usage throughout the genome or reduction in charging of the cognate tRNAs[38]. Pavlova et al. demonstrate that nutrient stress results in specific reductions in charged glutamyl-tRNAs, consequently reducing translation of poly-glutamine tract-containing proteins[39]. Similarly, Darnell et al. demonstrate that arginine depletion reduces charged arginyl-tRNA, resulting in increased ribosome pausing and premature termination events[42]. Loayza-Puch et al. use differential ribosome codon reading (DIRICORE) to assess potential nutrient limitation, uncovering proline and asparagine availability differences in cancers that may affect progression[40]. Lastly, Knott et al. find that modulation of asparagine availability via asparagine synthetase (ASNS) can directly affect cancer metastasis[41]. Taken together, these studies imply that regulation of availability of translation-adjacent elements can itself modulate translation, particularly in the context of cancer.

1.3 Aminoacyl tRNA synthetases (aaRS) play adaptive roles in translation and disease

Aminoacyl tRNA synthetases, (aaRS) are the class of molecules responsible for ligating amino acids to all corresponding isoacceptor transfer RNAs (tRNAs), in a “charging” reaction (Figure 1.1).

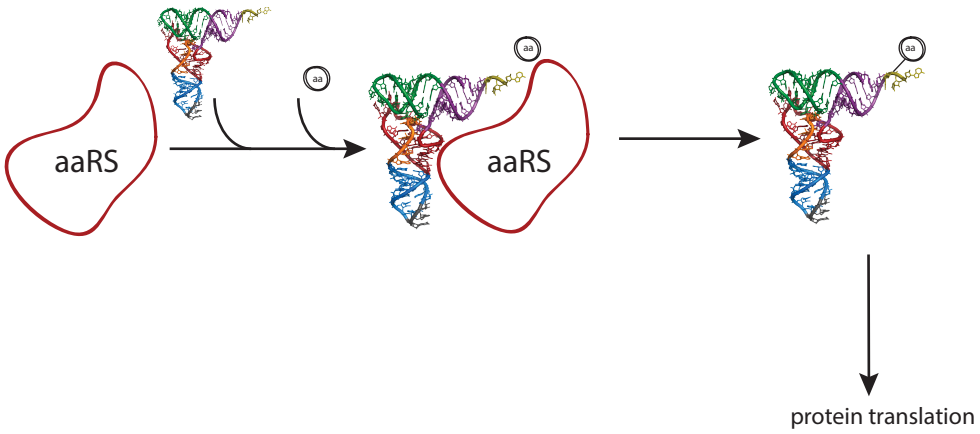

Figure 1.1. Aminoacyl tRNA Synthetases "charge" tRNAs with amino acids
A schematic depicting tRNA charging by aminoacyl tRNA synthetases (aaRS). aaRS ligate individual amino acids to all corresponding isoacceptor tRNAs, making them available to participate in protein translation.

tRNA synthetases are amino-acid specific, and aptly named using the corresponding single-letter amino acid abbreviation followed by ARS: for example, leucyl-tRNA synthetase which ligates leucine to 5 isoacceptor tRNA-Leu species, is abbreviated LARS. Unsurprisingly, tRNA synthetases are highly conserved and specific for the tRNAs and amino acids they recognize, with some containing proofreading mechanisms for mischarged tRNAs as an additional regulatory step[43,44]. aaRS use two main mechanisms to aminoacylate tRNAs. The first mechanism, utilized by Class I synthetases, involves a five-stranded β-sheet connected by α-helices, and contains highly conserved HIGH and KMSKS catalytic motifs. The second, employed by Group II synthetases, makes use of a series of a seven-stranded β-sheet flanked by α-helices, with three less-conserved catalytic motifs[45,46]. Many cytoplasmic aaRS have been shown to associate with the multi-synthetase complex (MSC), a cytoplasmic structure that groups several synthetases together. Recent structural reports have demonstrated the MSC to be a compact structure, grouping aaRS with anticodon recognition domains clustered on one side,

presumably to facilitate delivery of charged tRNAs for protein translation[47], though the function of this complex requires further exploration.

While their function in aminoacylation is critical to maintain charged tRNA pools for protein translation, several aaRS have also been found to have non-canonical physiologic functions unrelated to their catalytic activity within cells[48–50]. One notable example is WARS, which can be alternatively spliced to produced N-terminal fragments that inhibit angiogenesis through VE-cadherin[51]. LARS has additionally been implicated as an intracellular leucine sensor in activation of mTOR, signaling for cell autophagy[52].

Unsurprisingly, dysregulation of tRNA synthetases can have significant physiologic consequences by affecting either canonical or noncanonical functions, a subject that has been reviewed extensively[53,54]. The most notable example is mutations of GARS that have been found in Charcot Marie Tooth disease, a common inherited form of intellectual disability[55]. Mutations in the editing domain of AARS have also been demonstrated to contribute to neurodegeneration[56] Of relevance to this work, we examine dysregulation of aaRS particularly in the context of cancer. Several tRNA synthetases have been implicated as oncogenes, where overexpression or gain-of-function mutations in these enzymes enhance cellular transformation potential and oncogenic fitness. MARS has been implicated as a biomarker for lung cancer metastasis[57], while YARS expression has been shown to promote gastric cancer progression[58]. Noncanonical functions of LARS in activating the mTOR pathway have led to speculation about its role as an oncogene in lung cancer[59]. Intriguingly, these molecules exert pro-tumorigenic effects through both canonical aminoacylation function and noncanonical functions unique to

each enzyme. The extent of pro-tumorigenic literature for various tRNA synthetases makes it even more surprising to uncover a unique tumor-suppressive program for this enzyme, as we describe in this thesis.

1.4 tRNAs: canonical and noncanonical roles in maintaining cellular homeostasis

1.4.1 Biogenesis and canonical activity of tRNAs

Having described a substantial role for translation and aaRS in cancer and disease, the natural corollary is to examine the role of tRNAs themselves in maintaining cellular physiology and promoting pathology. Briefly, tRNA biogenesis has been well characterized; prior to aminoacylation, pre-tRNAs are transcribed by RNA polymerase III, and then undergo a series of processing steps including intron splicing, cleavage of 5' leader and 3' trailer sequences, addition of a terminal 3'CCA tail, and, folding into the mature coordinated L-shaped tertiary structure, and addition, on average, of 13 post-translational modifications[60–62]. These mature tRNAs are further aminoacylated by the requisite aaRS as previously described, and become available for protein translation. Redundancy in the genetic code has been well described; the 47 mature human tRNAs bring 20 amino acids to ribosomes for protein translation, with tRNA 'isoacceptors' carrying the same amino acid to 61 distinct codons within mRNA transcripts[63,64]. The discrepancy in mature tRNAs to codons is accounted for by 'wobble' base pairing, in which the third position of a codon-anticodon pair can be mismatched; most commonly, a C in the third codon position can be recognized by an inosine-modified A on the tRNA anticodon, increasing redundancy[65].

A few reports have described changes in mature tRNA availability that impact breast cancer; Pavon-Eternod et al. describe overexpression of tRNA-iMet to enhance breast cancer, while Goodarzi et al. demonstrate pro-metastatic function of both tRNA-Arg^{CCG} and tRNA-Glu^{UUC} in breast cancer[66,67]. In both of these reports, tRNA abundance changes were sufficient to increase translation and expression of proteins enriched in the respective codons. Natural tRNA abundance differences, for example between isoacceptors for the same amino acid, can also alter cellular physiology or cell types or states, through induction of diverging cellular programs as previously described[36] or by affecting stability of mRNAs through use of 'rare' codons for which tRNA abundance is thought to be lower[68].

1.4.2 Accurate tRNA Quantification: Trials and Tribulations

Accurate absolute quantification of tRNA species has proved challenging for the field. tRNA species have highly conserved secondary and tertiary structures, and many contain numerous nucleotide modifications. Both of these attributes result in inefficient capture, ligation, and readthrough of tRNA transcripts by traditional reverse transcriptases (RTs), making standard high-throughput sequencing methods unreliable for quantification. To combat these limitations, several strategies have been tested. The first general approach is to remove structural RT blocks using fragmentation approaches to facilitate sequencing, for example in Hydro-tRNAseq[69]. Second, modification removal can be conducted to facilitate ligation-capture and RT readthrough, for example in AlkB-facilitated RNA methylation sequencing (ARM-Seq) and DM-tRNAseq[70,71], and T4-PNK-mediated 3' cyclic phosphate removal and 5' phosphorylation to facilitate adaptor capture and ligation[72,73]. These approaches improve capture and readthrough of some transcripts; however, they bias sequencing detection and recovery towards the fraction of tRNA species with fewer modifications or with modifications that can most easily be removed

by the respective approaches. A third strategy involves improving efficiency of tRNA capture during adapter ligation using more specific adapters: most recently, a Y-shaped RNA-DNA adapter that can efficiently capture 3' and 5' ends of tRNA species (YAMAT-seq)[74], or a two-step ligation reaction that can capture mature sequences as well as truncated RT products[75,76]. A fourth approach involves improving the fidelity and processivity of the RT enzyme used for library generation. The most ubiquitous of these enzymes is a thermostable template-switching RT, in thermostable template-switching group II intron RT sequencing (TGIRT-seq, DM-tRNAseq)[71,77,78]. A recent report combined many of the above approaches, optimized salt and temperature conditions to improve TGIRT enzyme readthrough, as well as improved bioinformatic mapping pipelines to improve the reliability of tRNA mapping[79]. Still, potential limitations remain in terms of biased recovery of tRNA species, impeding accurate quantification.

As an alternative, hybridization-based tRNA capture approaches have been proposed which circumvent the need for reverse transcription entirely. In these methods, a microarray or library of tRNA-specific DNA probes are hybridized to small RNAs, and RNA-DNA hybrids are further isolated and the DNA products sequenced[66,80]. These hybridization approaches allow for accurate isolation and quantification of all hybridized species; further, the requirement for an RNA-DNA hybrid in downstream processing steps further reduces the signal-to-noise ratio in DNA probe quantification[66]. Sequencing alignment of probes to a probe-specific library facilitates relative quantification of tRNA species between different groups of interest, in the absence of reliable absolute quantification.

Taken one step further, several sequencing approaches have attempted to additionally quantify information regarding the aminoacylation status of tRNA species. This information provides valuable insight into the true availability of tRNA pools for participation in protein translation. The most common approach to isolate and maintain charged tRNA populations involves isolation of RNA under acidic conditions (pH < 4.8) to prevent spontaneous deacylation of aminoacyl-tRNA bonds, and employs sodium periodate ($NaIO_4$) oxidation, which converts the free 3'-OH on uncharged tRNA species to a ketone. This modification leaves only aminoacylated tRNAs, which lack a free 3'-OH, for downstream approaches involving deacylation and free 3'-OH capture by sequencing adapters[81], microarray[82,83] or 3' biotinylation[38].

1.4.3 tRNA fragmentation

In response to cellular stresses or starvation, tRNAs can be cleaved, generating tRNA fragments (tRFs). Stress-induced tRNA fragmentation was first described in *T.thermophila* following nutrient starvation[84], and has since been observed across multiple species including yeast and mammalian cells, in response to multiple stresses including hypoxia, UV irradiation, and heat[85–87]. Ribonucleases (RNases) are responsible for cleavage and generation of tRFs, the most commonly characterized is angiogenin (ANG), which cleaves tRNAs at the anticodon loop to generate 5' and 3' tRNA halves[85]. However, stress-induced tRNA cleavage has also been described at other sites within tRNAs, including at the D loop[88,89].

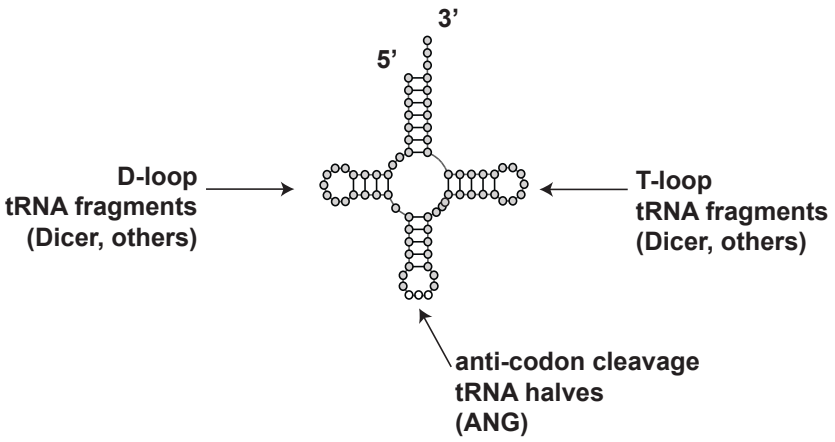

Figure 1.2. Potential sites of tRNA cleavage to generate tRNA fragments (tRFs)
A schematic depicting characterized tRNA fragmentation locations. Angiogenin has been shown to cleave tRNAs at the anticodon loop to generate tRNA halves, while other tRFs are generated through cleavage at the D loop[89].

The functionality of various tRNA fragments is also a topic of interest. Fragments have been shown to bind RNA binding proteins[88], mitigate cellular stress responses[90] and even affect ribosome biogenesis[91] and translation initiation[92]. Classically, tRNA fragments are not thought to deplete mature tRNA pools, though a handful of studies have begun to challenge that notion; a recent report implicated SLFN11-dependent tRNA-Leu^{TAA} fragmentation in cellular sensitization to DNA damage, through reduced expression of key Leu^{TAA}-rich DNA damage sensing genes ATM and ATR[93]. In this thesis, we describe a second phenomenon in which stress-induced tRNA cleavage is sufficient to reduce mature tyrosyl-tRNA species and affect gene expression programs, altering cell growth[90].

1.5 Thesis aims

The overarching goal of this thesis is to further characterize the adaptive roles of tRNAs and their associated factors in both disease and cellular homeostasis. First, we focus on the broad role of tRNA-Leu species and their associated leucyl-tRNA synthetase (LARS) in suppressing breast cancer transformation and growth (**Chapter 2**). Next, we focus on tRNA-Tyr and its

adaptive role in translation modulation downstream of oxidative stress-induced fragmentation, which we show to repress tyrosine-rich protein translation and cell growth. (**Chapter 3**). These complementary studies offer broader insights into the dynamic roles of tRNA in adaptive signaling, translation, maintenance of cellular homeostasis and mitigation of disease phenotypes.

CHAPTER 2. Leucyl-tRNA synthetase is a tumor suppressor in breast cancer and enables tumor suppressive translation

2.1 Rationale

Among the many hallmarks of cancer, protein translation is classically thought to be an upregulated cellular process in transformation. Surprisingly, we identified a novel tumor suppressor role for a tRNA synthetase, LARS, that plays a positive role in protein translation but is downregulated during breast malignant transformation. In this chapter, we characterize a novel tumor suppressive role for this gene in enacting a tumor suppressive translation program in breast cancer.

2.2 Leucyl-tRNA synthetase (LARS) is downregulated during malignant transformation

To identify candidate tRNA synthetases that may play a role in breast tumourigenesis, we assessed the expression levels of all tRNA synthetases in human breast cancers relative to normal breast tissue samples in The Cancer Genome Atlas (TCGA). Surprisingly, while 16/20 tRNA synthetases were overexpressed, LARS, KARS, QARS and DARS were reduced in tumours relative to normal breast tissues (Fig. 2.1).

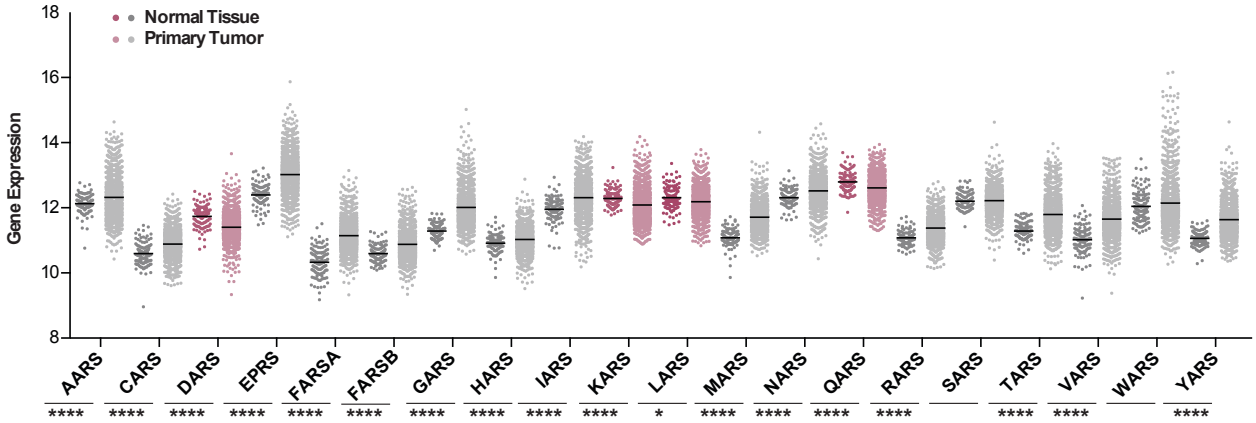

Figure 2.1. Clinical Evidence of LARS reduction upon malignant transformation. Aminoacyl tRNA synthetase (aaRS) expression levels in the TCGA database in normal breast tissue samples compared to primary tumor samples. Significant associations by two-tailed KS test with Bonferroni's correction indicated below. * = $p < 0.05$, **** = $p<0.001$.

We next performed Real-Time Quantitative Reverse Transcription PCR (qRT-PCR) for all tRNA synthetases in the non-transformed human mammary epithelial cell line MCF10A compared to the estrogen receptor negative (ER-negative) HCC1806 cell line (Fig. 2.2). Of the tRNA synthetases reduced by greater than 50%, only QARS and LARS were reduced in both human cell line and TCGA analyses. Of these two tRNA synthetases, we focused our attention on LARS, which exhibited a greater magnitude of reduction in HCC1806 cancer cells relative to MCF10A non-transformed cells.

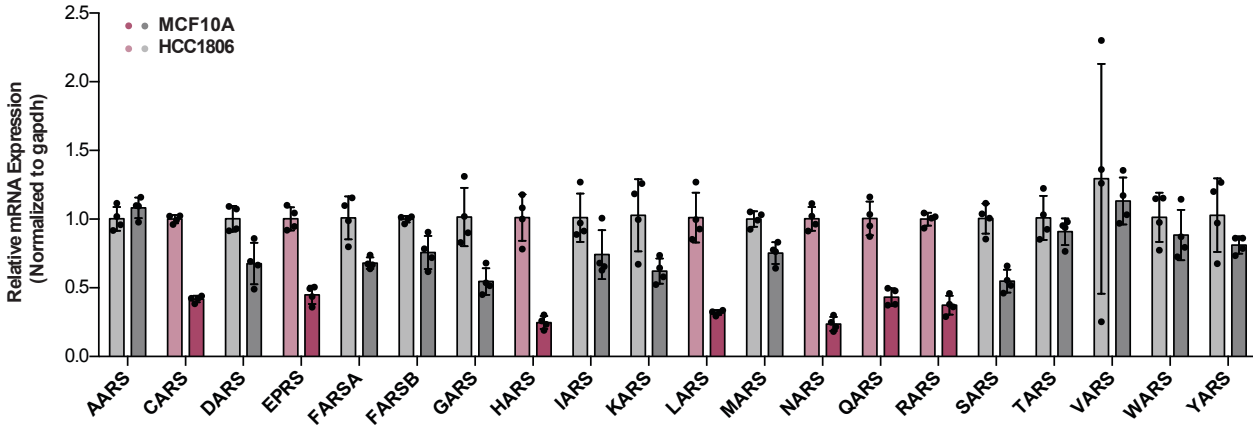

Figure 2.2. LARS is reduced in transformed HCC1806 compared to non-transformed MCF10A cells.
aaRS mRNA levels in non-transformed human mammary epithelial cell line MCF10A (left) compared to HCC1806 (right), normalized to GAPDH. Pink bars indicate a statistically significant decrease in aaRS expression between MCF10A and HCC1806 of 50% or greater ($p < 0.01$, unpaired two-tailed Student's t-test with Bonferroni correction) (n=4 samples per group).

To determine if LARS repression occurs during breast tumourigenesis, we transformed mammary epithelial MCF10A cells and the non-transformed murine mammary epithelial cell line NMuMG by overexpressing the polyoma middle-T (PyMT) oncogene in the context of p53 inhibition by pifithrin-α (PFT)[94]. PyMT-transformed MCF10A and NMuMG cells successfully formed colonies in soft agar compared to control cells, a hallmark of successful malignant transformation (Figure 2.3a). To further test tumor formation potential *in vivo*, PyMT-

transformed NMuMG cells were transplanted into the mammary fat pads of NSG mice and monitored for tumor formation. PyMT-transformed cells formed tumours as early as 14 days post transplantation, while control transduced cells did not form tumors, indicating that PyMT transformation facilitates *in vivo* mammary tumor formation. (Figure 2.3b).

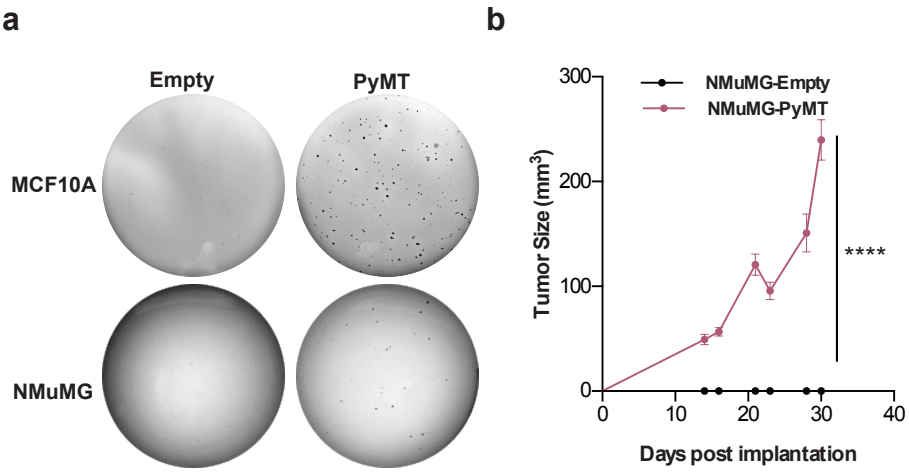

Figure 2.3. Transfection with PyMT lentivirus successfully transforms NMuMG and MCF10A cell lines.
a, Soft agar colony formation assays of PyMT-transformed MCF10A and NMuMG cells compared to empty-transduced control. Representative of n=3 experiments. **b**, tumor growth curves for transplanted PyMT transformed NMuMG cells compared to empty control. **** = $p < 0.0001$, 2-way ANOVA (n=4 mice per group).

Following PyMT tranformation, we assessed LARS expression in these cell lines by western blot. Surprisingly, we observed a significant reduction in LARS protein levels in both NMuMg and MCF10A transformed cells compared to empty-transduced controls (Figure 2.4).

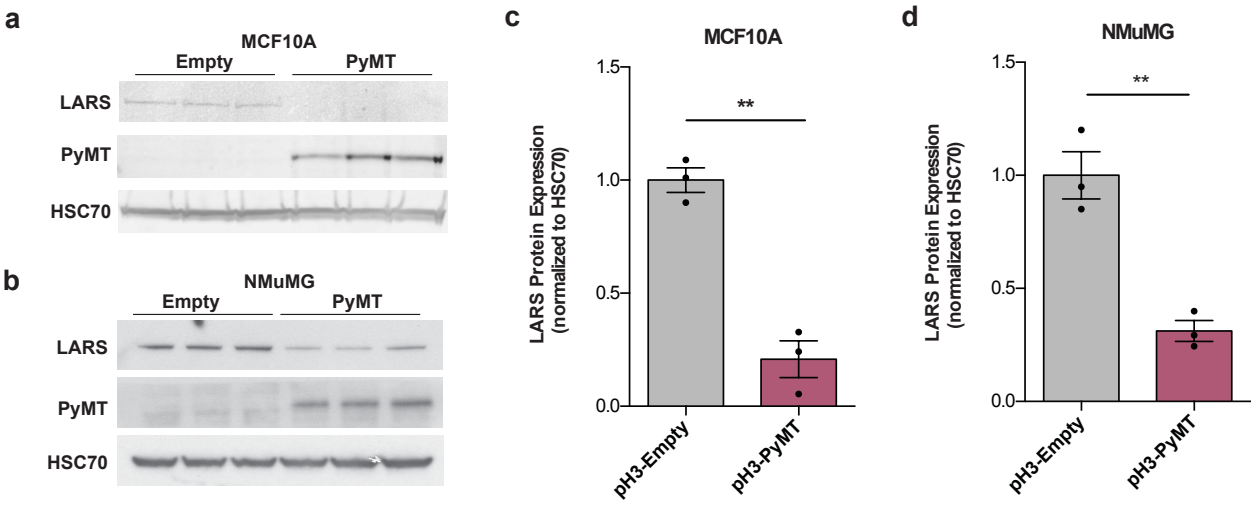

Figure 2.4. LARS is specifically downregulated upon PyMT-mediated transformation. **a,b,** Western blot of LARS protein levels in transformed MCF10A (**a**) and NMuMG (**b**) cells. Transformation indicated by PyMT expression, HSC70 is used as a loading control. **c,d,** Quantification of **b**. Representative of n=3 independent experiments.

To assess whether other tRNA synthetases were similarly downregulated during transformation, we assessed protein levels of other tRNA synthetases including isoleucyl, hitidyl and asparaginyl-tRNA synthetases (IARS, HARS, NARS, respectively). To our surprise, none of these synthetases were depleted in PyMT transformed cells. (Figure 2.4e-f). These data reveal that LARS specifically becomes repressed during malignant transformation of mammary epithelial cells.

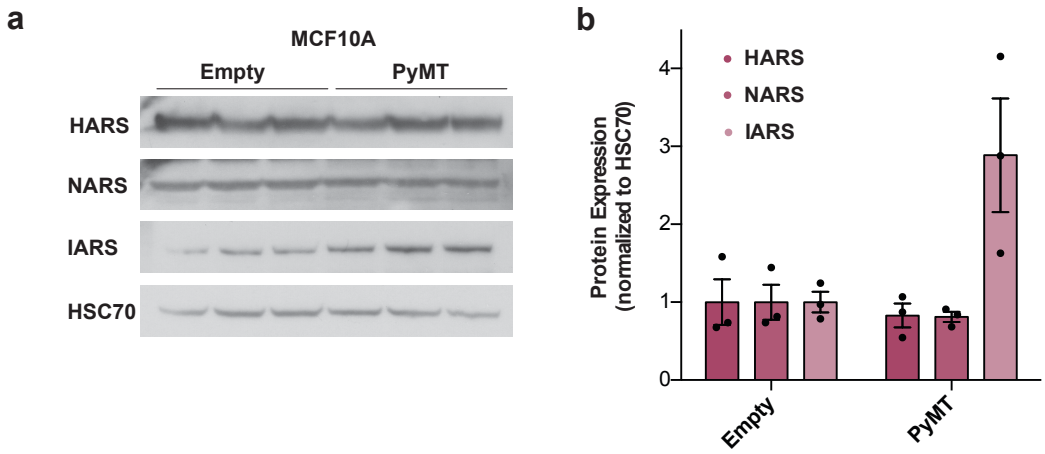

Figure 2.5. PyMT transformation does not repress other tRNA synthetases.
a, Western blot of histidyl, arginyl and isoleucyl tRNA synthetases in PyMT-transformed MCF10A cells compared to control, HSC70 is used as a loading control. Representative of n=2 independent experiments. Data are mean ± s.e.m, n.s. by unpaired two-tailed Student's t-test. **b,** Quantification of **a**.

Next, we sought to determine the generalizability of LARS depletion in breast cancer. We assessed LARS expression levels at the RNA and protein level across multiple human and mouse cell lines. LARS mRNA and protein expression were lower in MDA-MB-231, HCC1806 and T47D breast cancer cell lines relative to non-transformed MCF10A cells. Similarly, LARS mRNA and protein levels were reduced in murine breast cancer lines 4T07 and EO771 relative to non-transformed NMuMG cells (Figure 2.6).

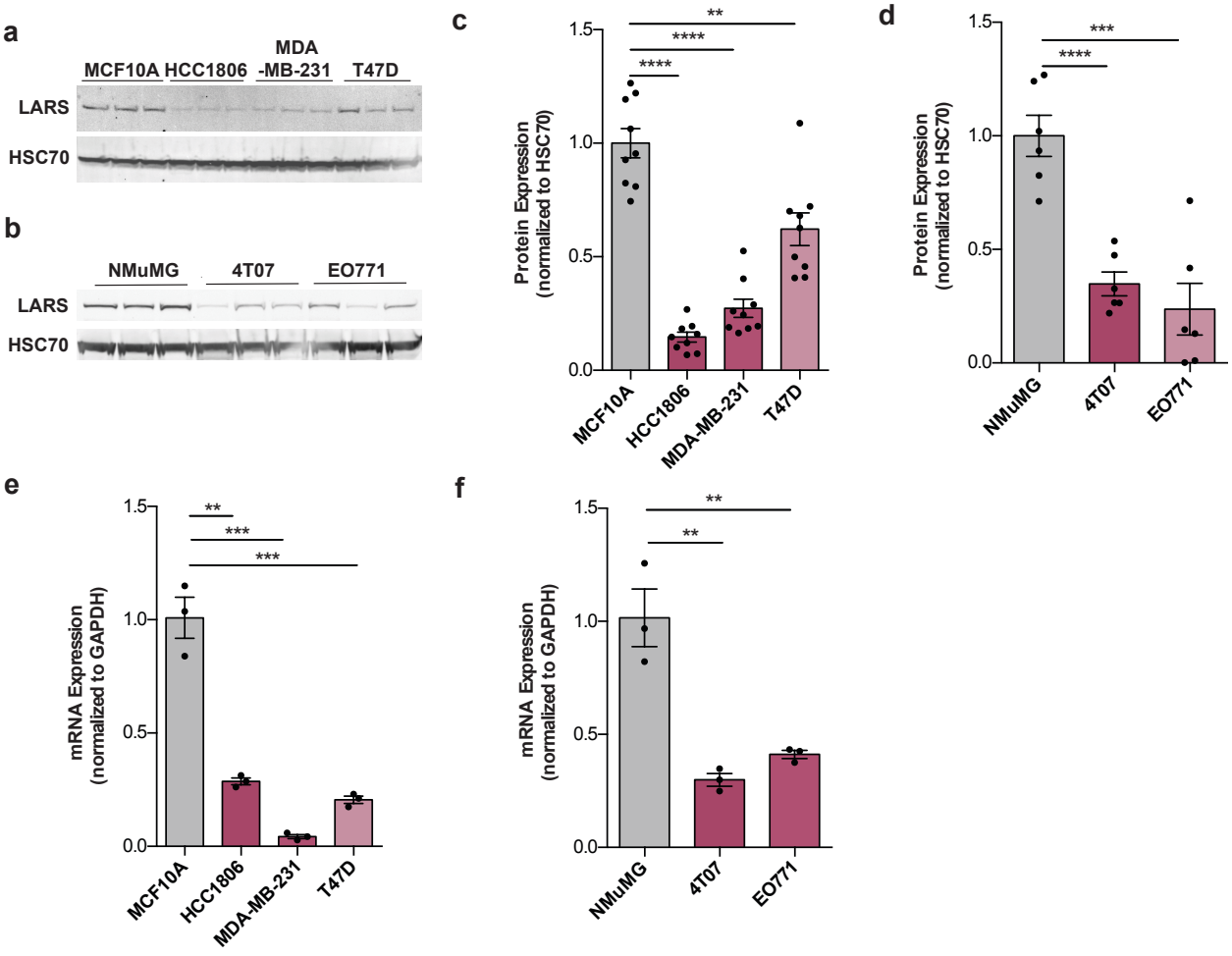

Figure 2.6. LARS is reduced in cancer cell lines compared to mammary epithelial cell lines. **a**, Western blot of LARS protein levels in non-transformed human mammary epithelial cell line MCF10A, triple negative HCC1806, MDA-MB-231 and T47D cell lines. **b**, LARS protein levels in non-transformed murine mammary epithelial line NMuMg, and murine breast tumor lines 4T07 and EO771. HSC70 is used as a loading control. **c,d,** Quantification of **a-b,** respectively. **e,** qRT-PCR of LARS mRNA levels in MCF10A, HCC1806, MDA-MB-231 and T47D cell lines, normalized to GAPDH. **f,** LARS mRNA levels in NMuMG, 4T07 and EO771 cell lines, normalized to GAPDH. Representative of n=3 independent experiments. Data are mean ± s.e.m. * = $p < 0.05$, ** = $p < 0.01$, *** = $p < 0.001$, unpaired two-tailed Student's t-test.

We also asked whether LARS expression could be further reduced in highly metastatic cells relative to poorly metastatic cells. To test this, we compared LARS protein expression in two sets of isogenic cell lines: the human MDA-MB-231 parental cells relative to its highly metastatic MDA-LM2 derivative, and the murine 67NR and 4T07 poorly metastatic lines versus

4T1 highly metastatic line. In both of these cell line pairs, we did not observe further reduction of LARS expression with metastatic potential. (Figure 2.7). Taken together, these results suggest that LARS repression may specifically regulate breast cancer formation rather than metastatic progression.

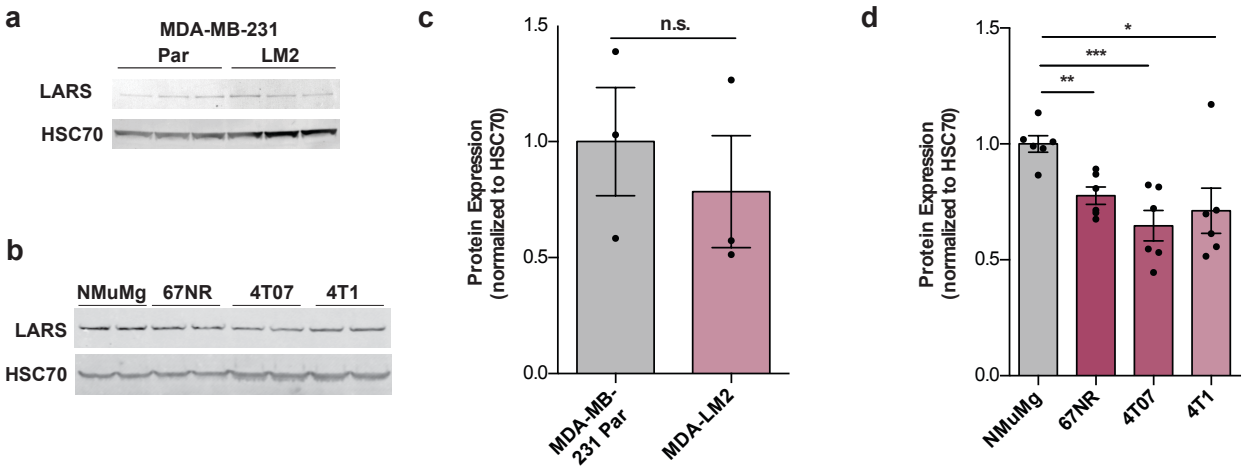

Figure 2.7. LARS expression does not correlate with cell line metastatic capacity. **a,** western blot of LARS in MDA-MB-231 parental cells compared to highly metastatic LM2 cell lines. **b**, western blot of LARS in NMuMG cell lines compared to isogenic low and high metastatic cell lines 67NR, 4T07 and 4T1. HSC70 is used as a loading control in both experiments. **c,d,** Quantification of **a-b**. Representative of n=3 independent experiments. Data are mean ± s.e.m. * = $p < 0.05$, ** = $p < 0.01$, *** = $p < 0.001$, unpaired two-tailed Student's t-test.

2.3 LARS suppresses tumorigenesis and growth in a genetically initiated breast cancer mouse model

To determine if LARS directly regulates tumourigenesis, we utilized the established MMTV-PyMT genetically initiated murine model of breast cancer[24]. PyMT animals expressing MMTV-driven *Cre*-recombinase were crossed to animals homozygous for a *Lars* allele harboring loxP sites[95], enabling constitutive monoallelic deletion of LARS in the mammary epithelium. Animals were compared based on MMTV-*Cre* genotype; as expected, monoallelic deletion in *Cre*-positive animals reduced LARS protein levels by ~50% compared to *Cre*-negative littermates

(Figure 2.8a). We compared number of initiated tumors at 12 weeks of age between these groups, a typical tumor initiation time point in the PyMT model[24,96]. Surprisingly, LARS depletion was sufficient to significantly increase the number of palpable tumors at this time point. (Figure 2.8b). We also measured primary tumor burden over time and found that LARS depletion increased tumor burden (Figure 2.8c).

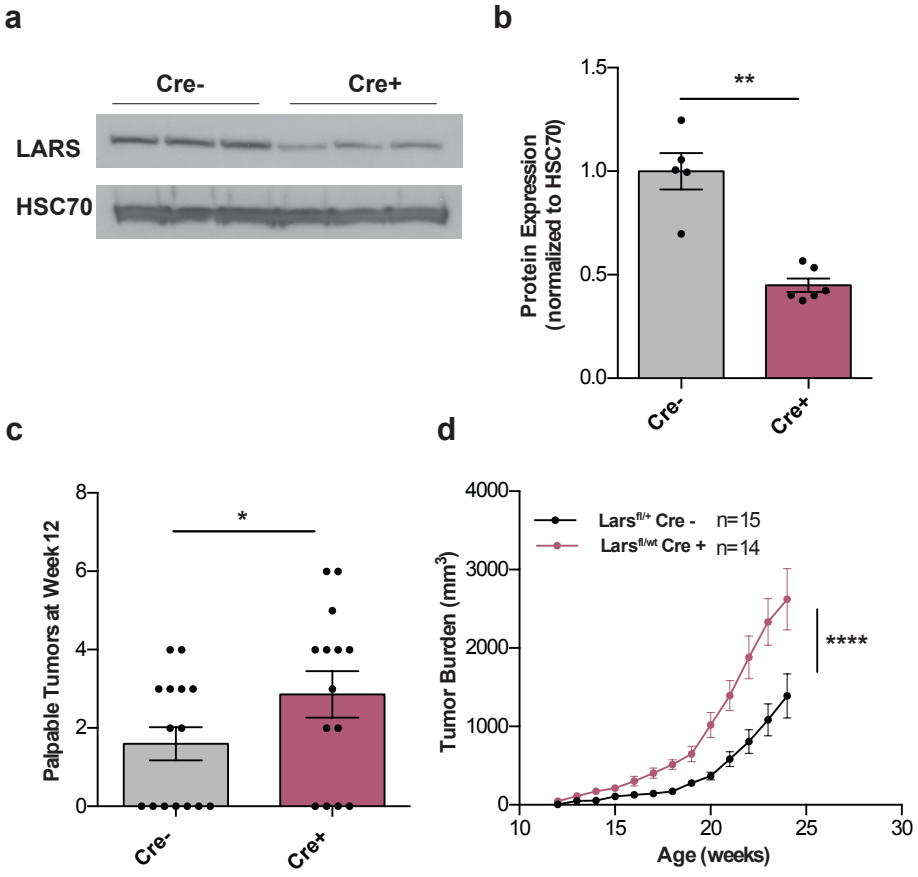

Figure 2.8. LARS depletion increases tumorigenesis and proliferation in a genetically initiated mouse model.
a, Western blot of LARS levels in MMTV-*Cre*-expressing PyMT tumours with monoallelic LARS deletion compared to *Cre*-negative animals. *Cre* expression results in 50% reduction in protein levels. Representative of n=3 independent blots, each sample is from one mouse. **b,** Quantification of **a**. ** = $p < 0.001$, unpaired two-tailed Student's t-test. **c,** Number of palpable initiated tumours per mouse at week 12 in PyMT model with LARS deletion. * = $p < 0.05$, unpaired one-tailed Student's t- test. **d,** Growth curves depicting overall tumour burden in PyMT model animals stratified by MMTV-*Cre* expression. *Cre*+ n=14, *Cre*- n=15, **** = $p < 0.0001$, 2-way ANOVA.

To further characterize a LARS-mediated tumour growth phenotype, we stained mammary tumour sections for the proliferation marker Ki67 by immunofluorescence. Consistent with our tumour growth measurements, Ki67 staining revealed enhanced proliferation in *Cre*-positive *Lars*$^{fl/+}$ animals compared to *Cre*-negative littermates (Figure 2.9). To further assess whether LARS-dependent tumour growth effects observed *in vivo* were cell autonomous, we derived heterotypic organoids from PyMT tumours of *Cre*-positive and *Cre*-negative *Lars*$^{fl/+}$ mice[97]. When cultured in Matrigel, *Cre*-positive *Lars*$^{fl/+}$ organoids exhibited significantly increased growth relative to *Cre*-negative organoids (Figure 2.9). Taken together, these findings implicate LARS as a breast cancer tumour suppressor through repression of mammary tumour initiation and cell-autonomous growth.

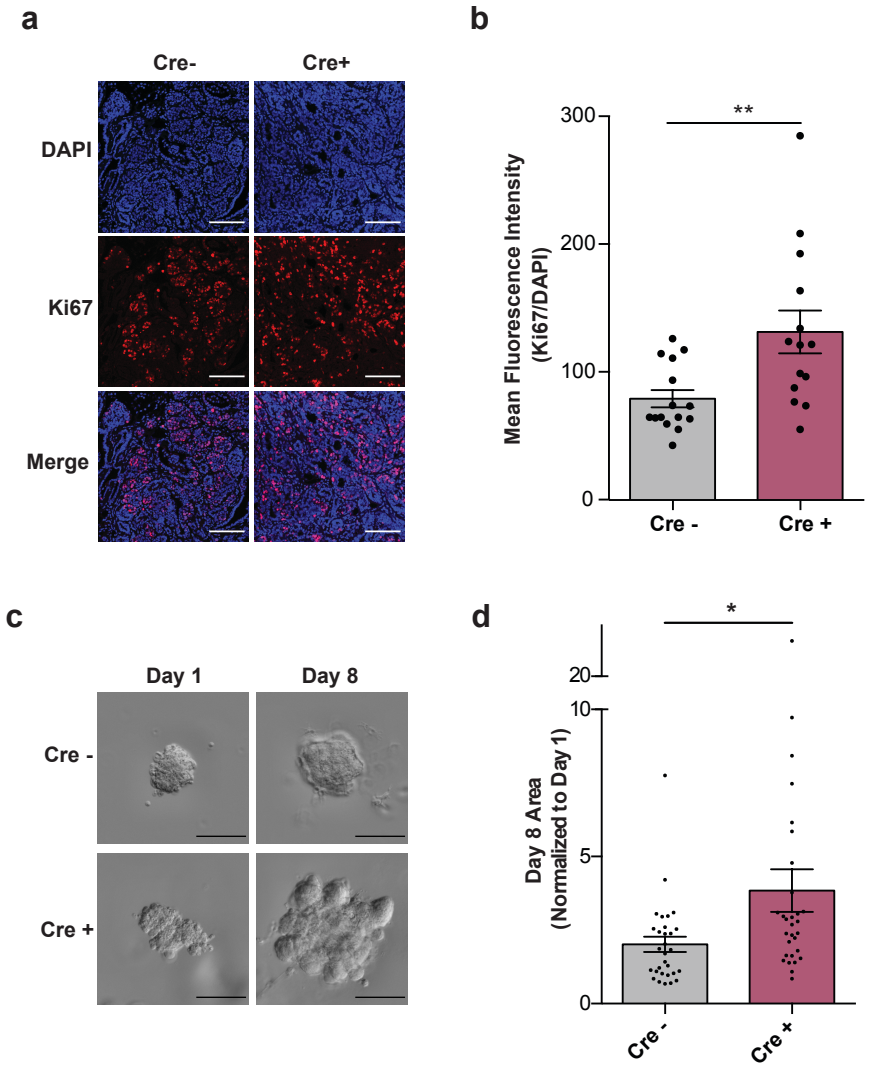

Figure 2.9. LARS depletion increases proliferation in a non-cell autonomous manner. **a,** Representative images of Ki67 staining in LARS-depleted PyMT tumours. Scale bar, 100px. **b,** quantification of **a** as mean fluorescence intensity of Ki67 normalized to DAPI. *Cre-* n=15, *Cre+* n=14, where each data point represents staining from an individual animal. ** = $p < 0.01$, two-tailed Mann-Whitney test. **c,** Representative images of PyMT tumour-derived organoids cultured in Matrigel. Scale bar, 100 μm. **d**, Quantification of change in 2D projection of organoid area, normalized to Day 1. Representative of n=3 independent experiments. * = $p < 0.05$, unpaired two-tailed Student's t-test. All data are mean ± s.e.m.

2.4 LARS depletion mediates tumorigenesis through reduction of select charged and total tRNA-Leu isoacceptors

LARS ligates leucine amino acid to all five tRNA-Leu isoacceptors. We reasoned that LARS-dependent tumour suppression may occur through altered levels of specific leucyl-tRNAs. To

test this hypothesis, we adapted our previously reported tRNA capture-sequencing profiling approach[66] to allow for relative quantification of charged tRNA species, in charged tRNA profiling. In brief, we isolated RNA under acidic conditions to preserve aminoacyl-tRNA bonds and then oxidized uncharged tRNAs with sodium periodate ($NaIO_4$)[38,39,81], leaving only charged species available for downstream biotinylation and capture for sequencing as previously described. In parallel, total tRNA was isolated for comparison (Figure 2.10).

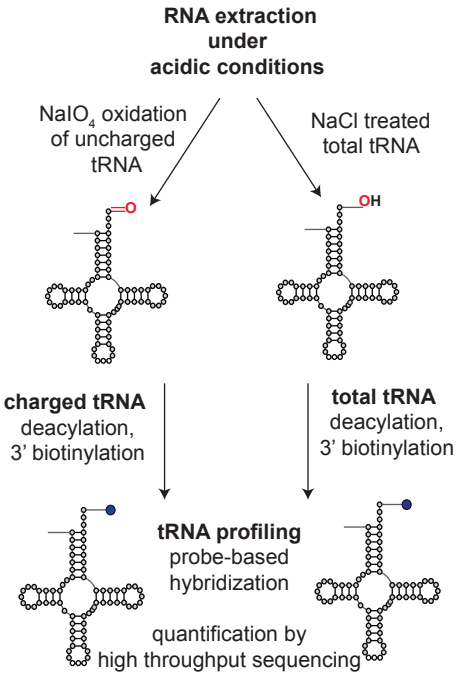

Figure 2.10. an overview of charged tRNA profiling.
An experimental overview of charged tRNA profiling. In brief, samples are extracted under acidic conditions, subjected to sodium periodate oxidation of uncharged tRNAs, followed by deacylation, 3' end biotinylation and capture, and probe-based hybridization and ligation. Probes are amplified and quantified by high-throughput sequencing.

Given the previously observed endogenous differences in LARS protein expression, we chose to perform charged tRNA profiling in transformed HCC1806 cells compared to un-transformed MCF10A cells. Charged tRNA profiling revealed reduced expression of four out of five leucyl

tRNA isoacceptors in HCC1806 cells relative to MCF10A cells (Figure 2.11a). Among these tRNAs, tRNA-Leu^{CAG} exhibited the greatest magnitude of reduction. Interestingly, the same tRNA-Leu species were reduced in total tRNA quantification, with tRNA-Leu^{CAG} exhibiting the greatest reduction (Figure 2.11b). These findings are consistent with the literature, whereby reduced tRNA charging has been found to lead to tRNA destabilization and degradation, reducing overall tRNA abundance[98,99]. As such, northern blot analysis for the most significantly reduced tRNA-Leu species—tRNA-Leu^{CAG}, tRNA-Leu^{AAG}, and tRNA-Leu^{TAG}—revealed a reduction in overall expression of these tRNAs in HCC1806 relative to MCF10A cells (Figure 2.11c).

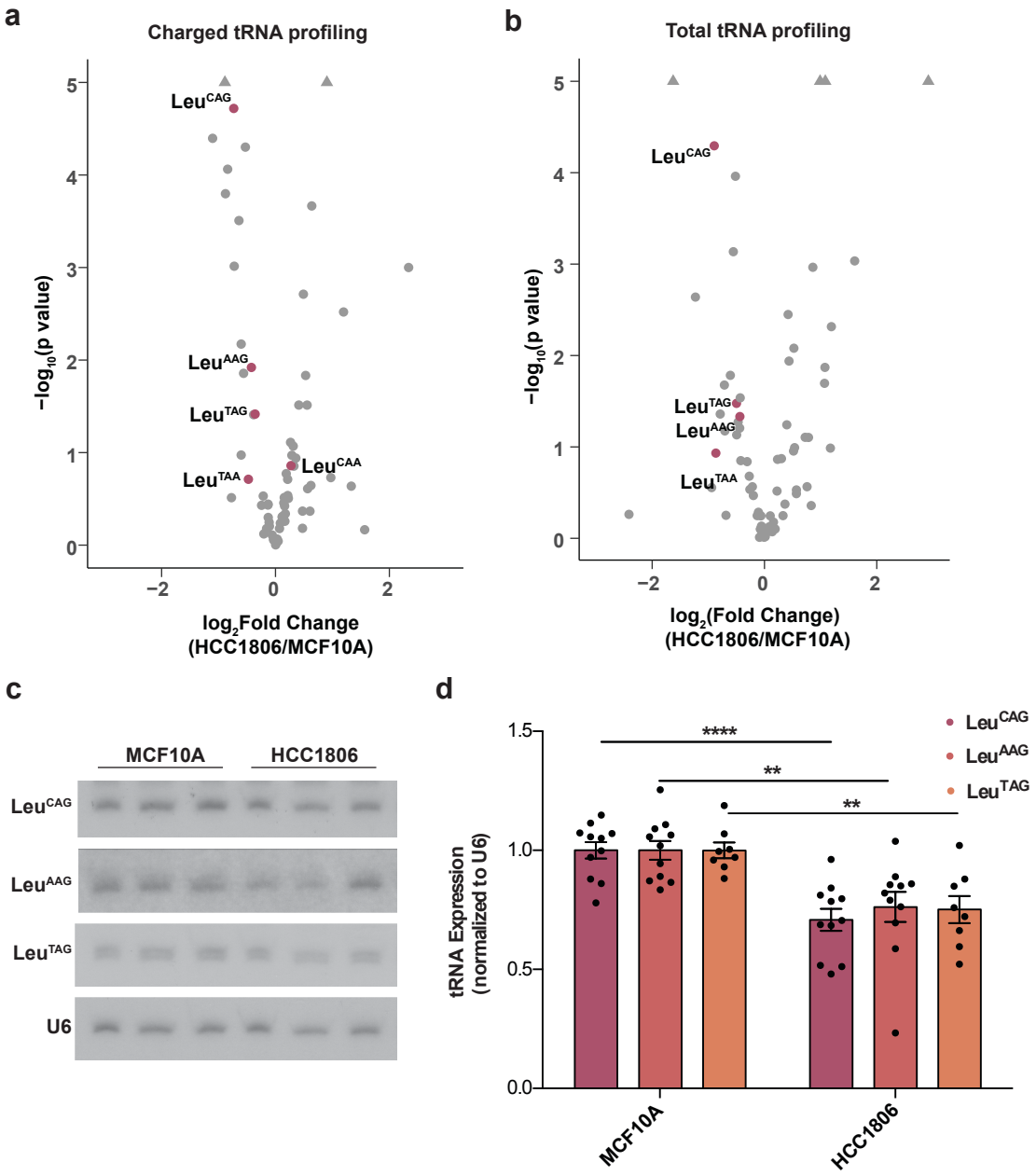

Figure 2.11. tRNA-Leu isoacceptors are reduced in LARS-low cells.
a, Volcano plot showing differential expression of charged tRNAs in HCC1806 cell line compared to MCF10A (n=3 samples per group). **b,** Volcano plot showing differential expression of total tRNAs in HCC1806 cell line compared to MCF10A (n=3 samples per group). **c,** Northern blot validation of reduction in tRNA-Leu species in HCC1806 compared to MCF10A. **d**, quantification of **c**. Representative of n=3 independent experiments, ** = $p < 0.01$, **** = $p < 0.0001$, unpaired one-tailed Student's t-test. All data are mean ± s.e.m.

As orthogonal validation of LARS-mediated tRNA-Leu depletion, we also assessed total tRNA-Leu levels in LARS-depleted 4T07 cells (Figure 2.12). tRNA-Leu^{CAG}, tRNA-Leu^{AAG}, and tRNA-Leu^{TAG} were all reduced in 4T07 cells with 90% reduction in LARS by shRNA, confirming the findings above.

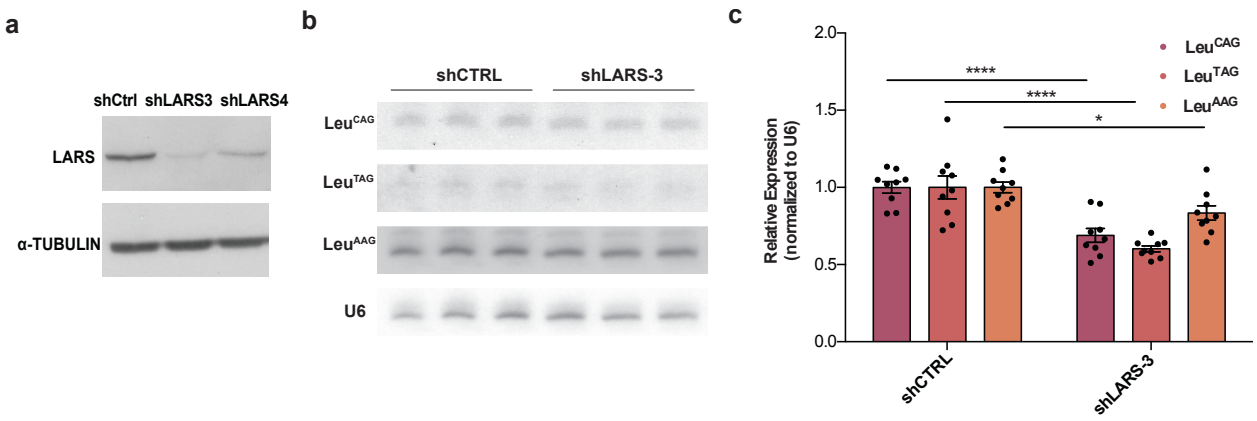

Figure 2.12. tRNA-Leu isoacceptors are reduced in LARS-depleted 4T07 cells.
a, Western blot depicting LARS knockdown levels in 4T07 cells with two independent shRNAs. Representative of n=3 independent experiments. **b,** Northern blot validation of reduction in tRNA-Leu species in LARS-depleted 4T07 cells compared to control. Representative of n=3 independent experiments. **c,** Quantification of **b**. * = $p < 0.05$, **** = $p < 0.0001$, unpaired two-tailed Student's t-test. All data are mean ± s.e.m.

We next asked whether tumour suppression by LARS may be mediated by specific leucyl tRNA(s). We employed CRISPRi[100] to repress transcription of the most significantly reduced leucyl tRNA, tRNA-Leu^{CAG}, and assessed the impact of this on mammary epithelial cell transformation. Remarkably, CRISPRi-based depletion of tRNA-Leu^{CAG} in MCF10A cells enhanced PyMT-induced colony formation by soft agar assay (Figure 2.13). These findings identify tRNA-Leu^{CAG} as a mammary tumour suppressor downstream of LARS.

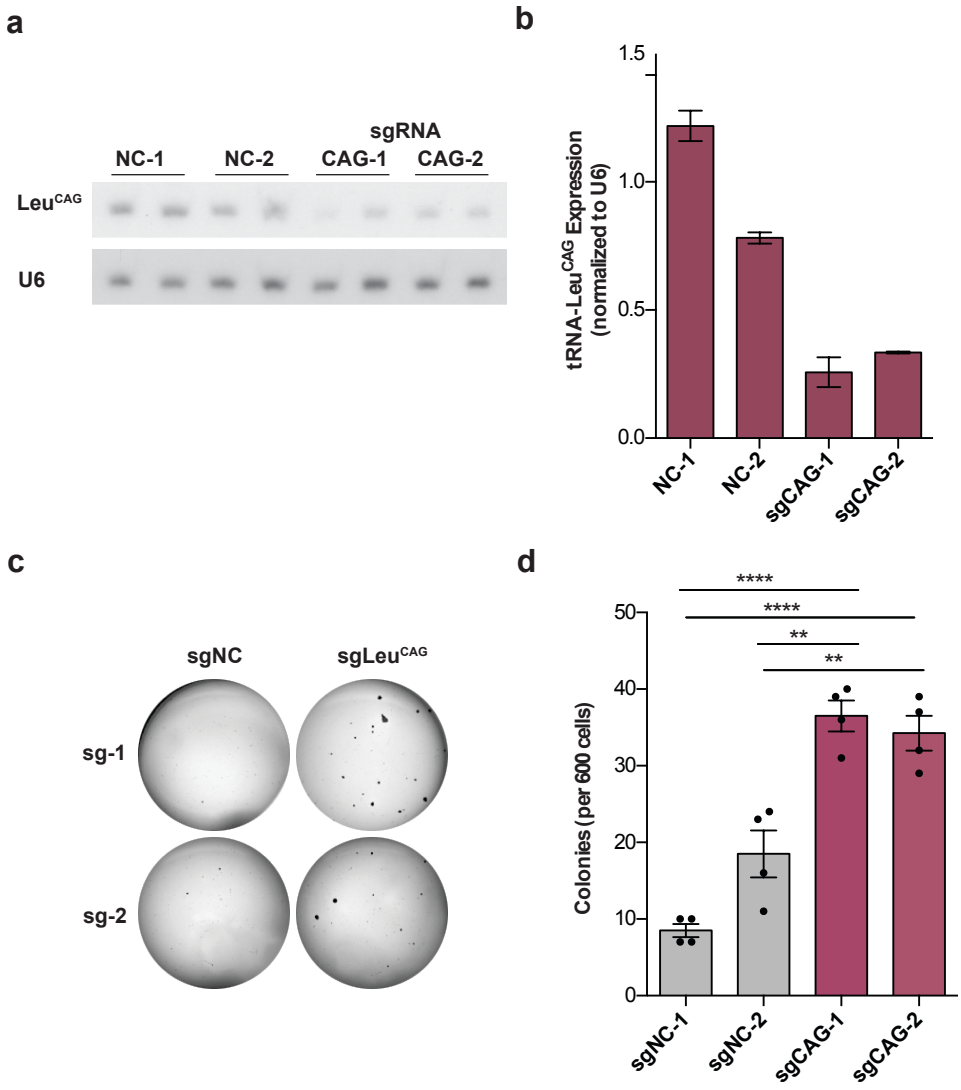

Figure 2.13. Depletion of tRNA-Leu^{CAG} increases transformation by colony formation. **a,** Northern blot depicting CRISPRi-mediated tRNA-Leu depletion in MCF10A cells. Representative of n=2 independent experiments. **b,** Quantification of **a. c,** Representative colony formation assays of PyMT-transformed, tRNA-Leu^{CAG} depleted MCF10A cells. **d**, Quantification of **c**. Representative of n=3 independent experiments. ** = $p < 0.01$, *** = $p < 0.001$, **** = $p < 0.0001$, unpaired two-tailed Student's t-test. All data are mean ± s.e.m.

Next, to exclude the possibility that LARS repression may exert its effects on tumorigenesis through metabolic alterations involving tumoural leucine availability, we conducted mass spectrometry-based metabolite profiling of branched chain amino acids within 4T07 LARS depleted tumours implanted into mice. Intratumoural levels of leucine, isoleucine and valine were not significantly altered in LARS-depleted relative to control tumours (Figure 2.14). This

finding suggests that LARS depletion does not meaningfully impact tumoural abundance of leucine or other branched-chain amino acids.

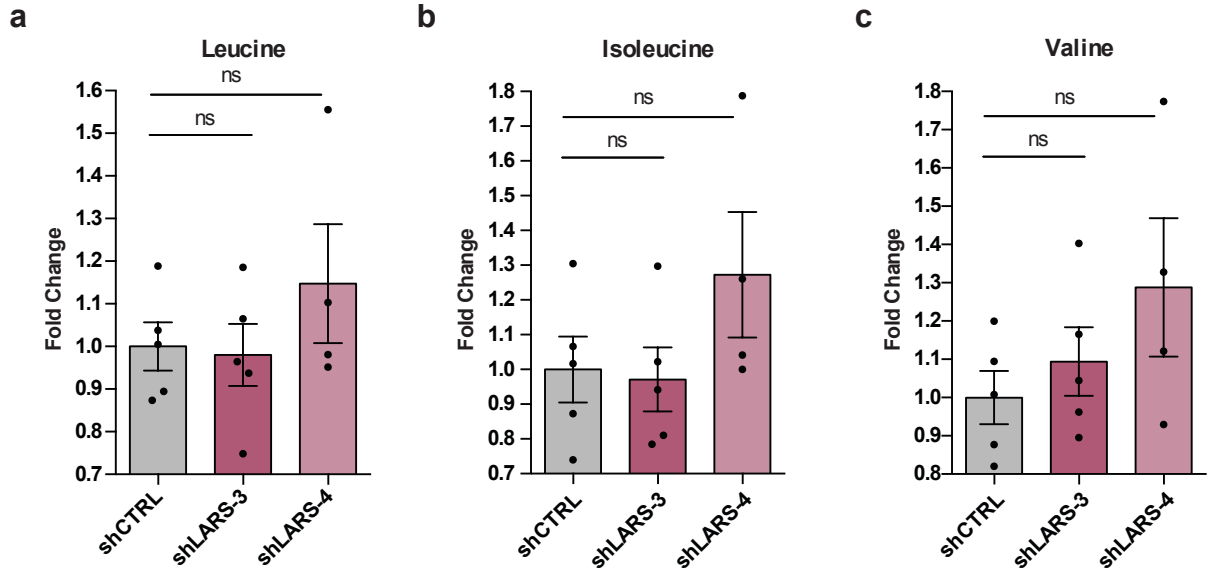

Figure 2.14. Intratumoral leucine, valine and isoleucine levels are not impacted by LARS depletion.
a-c, *In vivo* metabolomics of branched chain amino acids leucine (**a**), isoleucine (**b**) and valine (**c**) in LARS-depleted 4T07 tumours (n=5 mice per group). All data are mean ± s.e.m.

Another important mechanistic possibility to exclude was the previously described noncanonical function of LARS as a mediator of mTOR signaling[52]. In this report, Han et al. found LARS to sense intracellular leucine pools, activating autophagy in the context of low leucine. This function was carried out independent of LARS catalytic activity in aminoacylation. To assess the potential of LARS to impact mTOR signaling in our context, we assessed changes in S6 and S6K phosphorylation at mTOR-phosphorylation sites Ser240/244 and Thr389[101,102], respectively, in LARS-depleted PyMT tumors. Encouragingly, while phosphorylation of both targets was constitutively active in LARS-depleted and control tumors, there were no significant differences between the groups, implying that changes in mTOR activity do not contribute to our observed tumor suppressive phenotype (Figure 2.15).

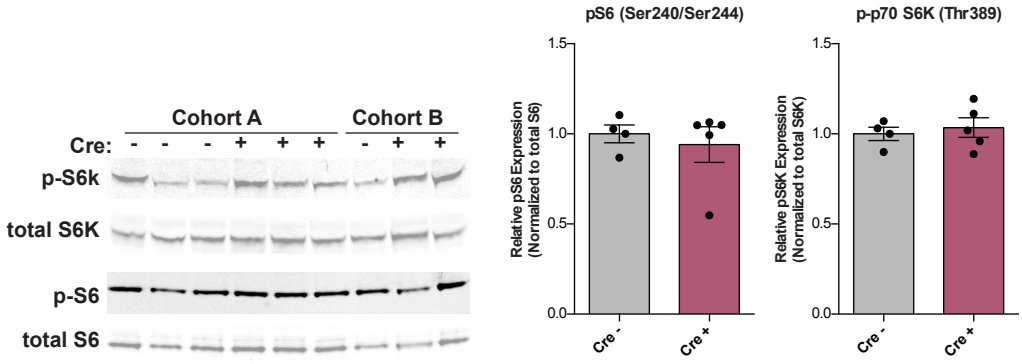

Figure 2.15. mTOR phosphorylation of S6 and S6K are unaffected by LARS depletion in PyMT tumors.

To further explore the role of mTOR signaling in our system, we derived PyMT organoids and treated with an mTOR-specific inhibitor, BC-LI-0186[103] and assessed growth changes in Matrigel. BC-LI-0186 specifically binds the RagD recognition domain of LARS, abrogating its mTOR signaling capacity but leaving its aminoacylation function intact. Consistent with a growth-promoting role of mTOR signaling, treatment with this inhibitor at various concentrations was sufficient to reduce organoid growth (Figure 2.16). As LARS is a pleiotropic, multifunctional enzyme, these results confirm the role of LARS in mTOR signaling and further highlight that this function is not driving the tumor suppressive phenotype observed.

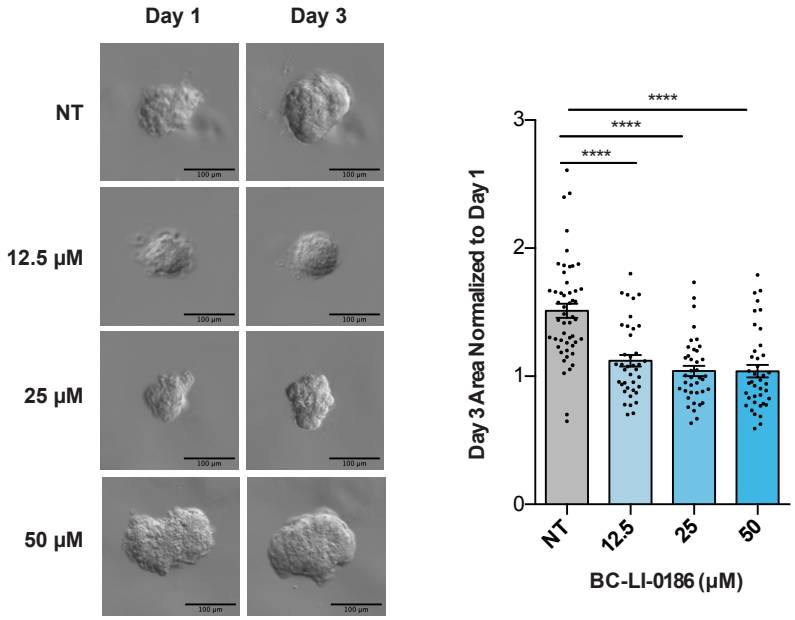

Figure 2.16. Specific Inhibition of LARS-mTOR signaling activity by BC-LI-0186 reduces organoid growth.
Left, Representative images of PyMT tumour-derived organoids cultured in Matrigel at Day 1 and Day 3 following inhibitor treatment. Scale bar, 100 μm. **Right**, quantification of change in 2D projection of organoid area at Day 3, normalized to Day 1. **** = $p < 0.0001$, unpaired two-tailed Student's t-test. All data are mean ± s.e.m.

2.5 LARS depletion impacts Leucine-rich translation in a codon-dependent manner

To further characterize the impact of LARS depletion on translation dynamics, we employed multiple translation profiling approaches. First, we conducted polysome profiling in 4T07 LARS-depleted cells. Polysome fractions were pooled into low-translated (1-2 ribosomes) and high-translated (>3 ribosomes) groups and associated mRNA transcripts were sequenced (Figure 2.17).

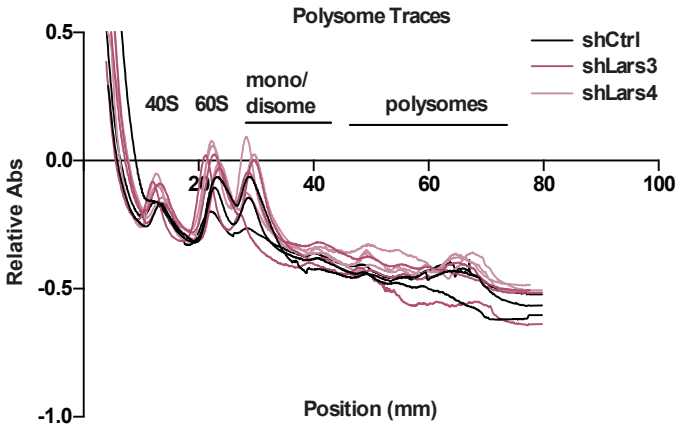

Figure 2.17. Polysome Profiling traces in 4T0 shLARS.
Polysome traces from gradient fractionation and polysome profiling in LARS-depleted 4T07 cells compared to control. (n=3 samples per group).

Differential expression was calculated in high vs low-translated fractions for LARS-depleted samples vs. control. We reasoned that if LARS repression promotes tumour formation via reduced availability of leucyl tRNAs, we would expect decreased polyribosome association with leucine codon-enriched transcripts. To assess this, we binned differentially expressed polysome-associated transcripts in LARS-depleted and control cancer cells into four quartiles based on total leucine codon content and plotted the $\log_2$ fold changes between these conditions as a cumulative distribution function (Figure 2.18). Transcripts containing the greatest number of leucine codons (top 25%) exhibited a significant left shift in $\log_2$ fold change compared to transcripts with the fewest codons (bottom 25%), consistent with LARS depletion-induced reduction of leucine-rich protein translation. The analysis was repeated, instead ranking and binning transcripts by specific leucine codon content. Top quartiles of Leu-CTC and Leu-CTG codon enriched transcripts also exhibited a significant left shift in $\log_2$ fold change (Figure 2.16b-c).

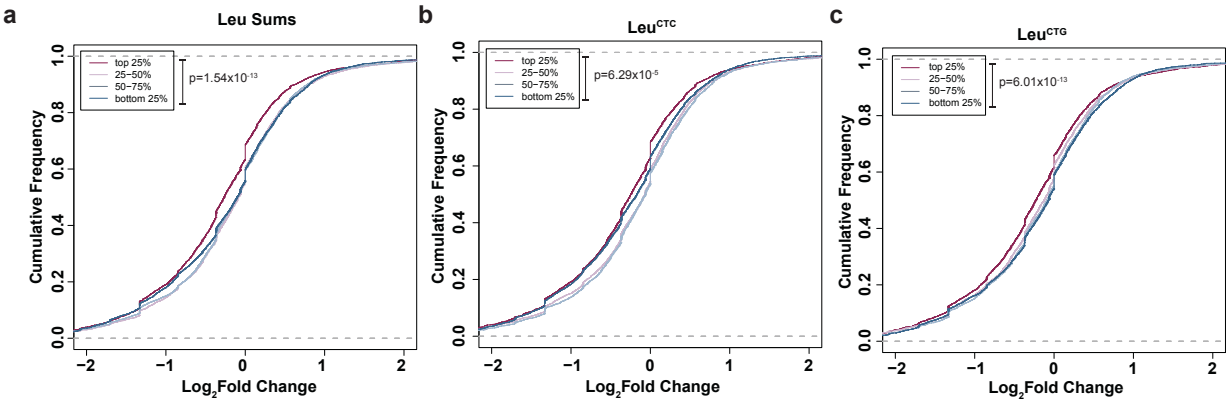

Figure 2.18. LARS depletion impacts polysome occupancy on Leu-rich transcripts. **a,** Cumulative distribution functions of differentially expressed genes by polysome occupancy in LARS-depleted 4T07 cell lines, stratified by overall Leu-codon content. Genes with higher Leu codon content have relatively lower log2 fold changes (left-shift) indicating lower translation in Lars knockdown (n=3 samples per group). **b,c,** as in **a**, stratified by individual Leu-CTC and Leu-CTG isoacceptor content, respectively. p < 1.54e-13 (**a**), p < 6.01e-13 (**b**), p < 6.29e-5 (**c**), two-sided KS test between top 25% and bottom 25% quartiles.

Interestingly, the remaining four Leu codons demonstrated no difference or a right shift in $\log_2$ fold change (Figure 2.19). These data suggest that global effects are primarily driven by Leu-CTC and Leu-CTG codon enriched transcripts, which account for ~60% of leucine incorporation into proteins[63,64]. Notably, Leu-CTG is decoded by tRNA-Leu^{CAG}, which was observed to repress transformation as described above, while Leu-CTC contains a wobble position and would be most likely be decoded by inosine-modified tRNA-Leu^{AAG} [65].

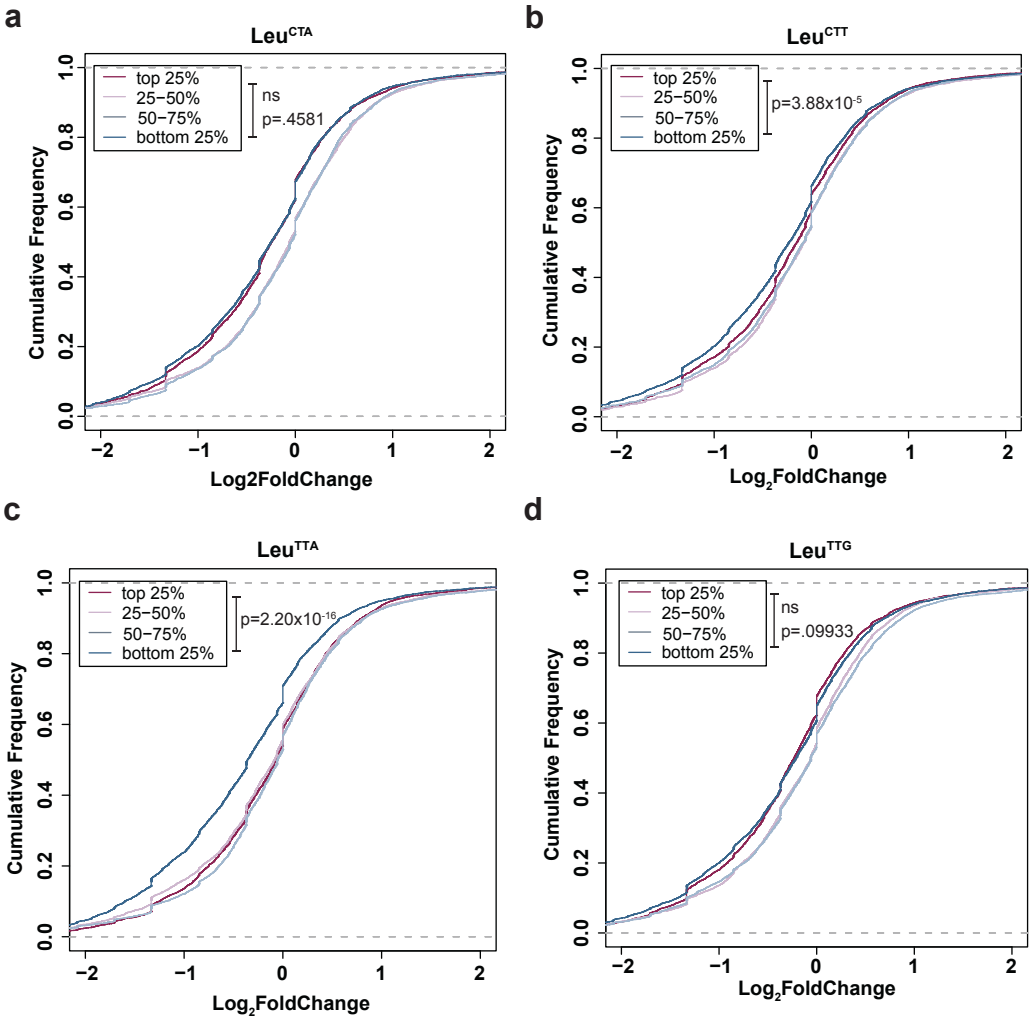

Figure 2.19. LARS depletion impacts polysome occupancy in a codon-dependent manner. Cumulative distribution functions of differentially expressed genes by polysome occupancy, stratified by Leu-CTA (**a**), Leu-CTT (**b**), Leu-TTA (**c**), and Leu-TTG (**d**) codon content, respectively. p < .4581 (**a**), p < 3.88e-5 (**b**), p < 2.20e-16 (**c**), p < 0.09933 (**d**), two-sided KS test between top 25% and bottom 25% quartiles.

As an orthogonal *in vivo* approach, we employed the RiboTag model[96,104] within our *Lars*-depleted PyMT tumour model to capture tumoral ribosome-associated mRNAs. Consistent with polysome profiling findings, differentially expressed leucine-rich genes in *Lars*$^{fl/wt}$ compared to wild-type tumours revealed a significant left-shift in cumulative distribution of $\log_2$ fold change (Figure 2.20). These effects were presumably more modest since the RiboTag system does not enrich for polysomes relative to monosomes. These findings reveal that LARS depletion reduces

polysome and ribosome association of leucine enriched transcripts, suggesting that reduced abundance of leucyl tRNAs significantly reduces translation of transcripts enriched in cognate leucyl codons.

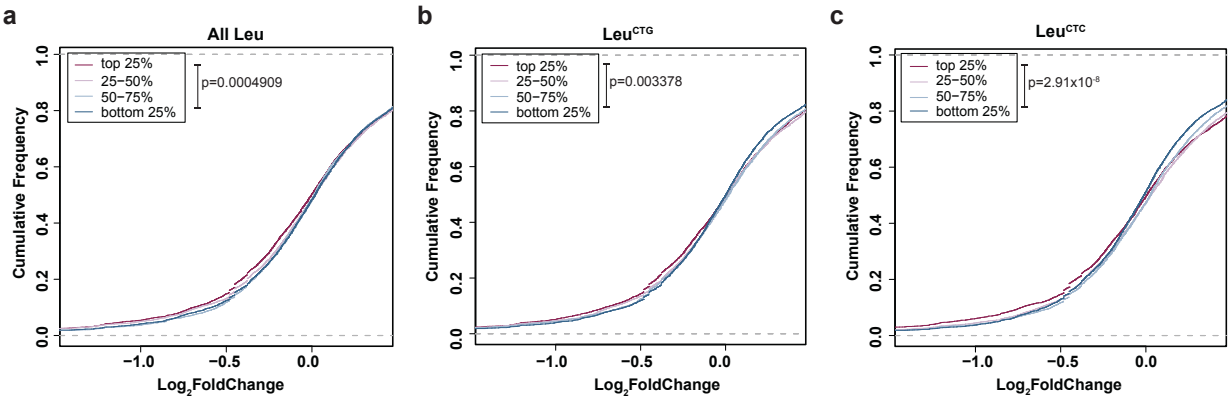

Figure 2.20. LARS depletion reduces ribosome association of Leu-rich transcripts in RiboTag mice.
a, Cumulative distribution functions of differential gene expression by RiboTag (n=3 mice per group), stratified by abundance of Leu isoacceptors (**a**) Leu-CTG (**b**) and Leu-CTC (**c**). p = 0.0004909 (**a**), p < 0.003378 (**b**), p < 2.91e-8 (**c**), two-sided KS test between top 25% and bottom 25% quartiles.

To further assess the impact of LARS depletion on leucine-rich protein translation, we conducted Ribo-seq[105] on LARS-depleted 4T07 cells. We first asked whether ribosome dwell time over each codon was substantially different in LARS-depleted samples compared to control. To do this, we calculated codon level bias coefficients, a measure proportional to ribosome dwell time. Regression of bias coefficients against cell lines demonstrated an increase in dwell time for all Leu codons in LARS-depleted samples compared to control. Importantly, LARS-mediated dwell time changes were significantly increased for Leu codons compared to other codons (Figure 2.21). These data suggest that LARS depletion preferentially enhances ribosome dwell time over leucine codons.

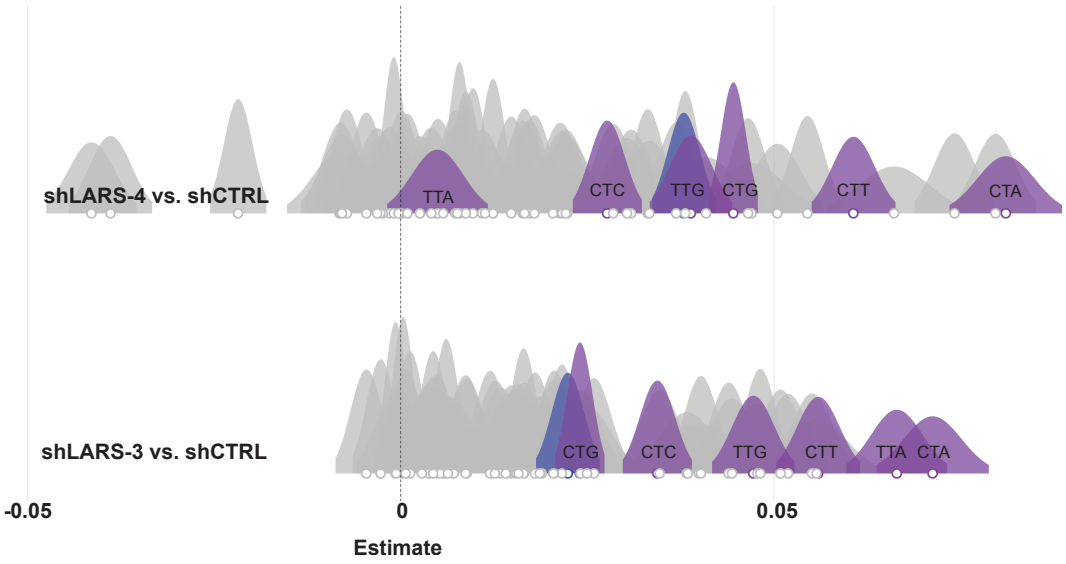

Figure 2.21. LARS depletion in 4T07 cells increases dwell time over leucine codons. Ribosome dwell time analysis in Ribo-seq data (n=2 samples per group). Leu codons show increased dwell time compared to other codons in Lars knockdown relative to control. shCtrl vs. shLars3, p = 0.001642; shCtrl vs. shLars4, p = 0.02282, Kruskal Wallis rank sum test.

We next asked if local translation rates were affected by clusters of leucine codons within a given gene. We calculated sequence discrepancy for leucine codons across all transcripts in control cells. This is represented as a value that ranges from 0 to 1 where 0 corresponds to an even distribution and 1 is perfectly uneven. We observed a significant positive regression coefficient for the association of sequence discrepancy and bias coefficient, suggesting that ribosome dwell time increases as leucine clustering increases (Figure 2.22).

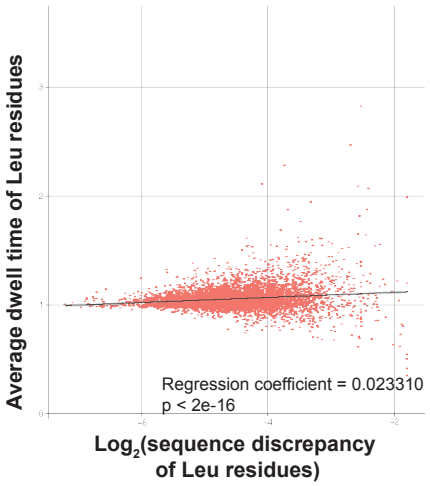

Figure 2.22. Sequence discrepancy impacts ribosome dwell time over leucine codons. Analysis of Leucine sequence discrepancy, or "clumpiness" on ribosome dwell time in 4T07 shCtrl cells. Regression coefficient = 0.023310, p < 2e-16.

Taken together, these data reveal that LARS depletion significantly impacts translation at leucine codons and reveal increased ribosome dwelling at regions of transcripts enriched in leucine codons.

2.6 LARS regulates expression of Leu-rich tumor suppressor genes

To identify candidate genes that mediate LARS-dependent tumor suppression, we performed tandem mass tag (TMT)-labeled proteomics[106] on tumours derived from *Lars* heterozygous PyMT mice differentially expressing MMTV-*Cre*. We identified a set of proteins that were significantly repressed in the context of LARS heterozygosity (Figure 2.23).

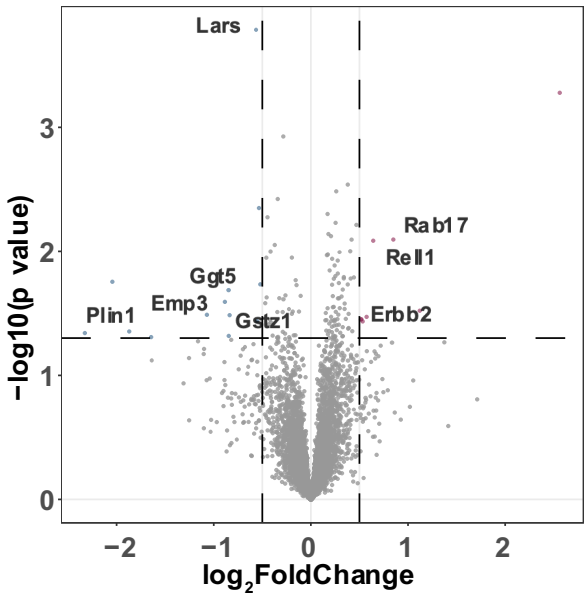

Figure 2.23. TMT-proteomics in LARS-depleted PyMT tumors reveals reduced tumor suppressive proteins.
Volcano plot of differentially detected proteins in TMT-labeled proteomics in PyMT Lars knockout tumours compared to control. Cutoffs of $\log_2$fold change < |0.5| and $p < 0.05$ indicated by dotted lines (n=5 tumors per group).

We were interested primarily in downregulated genes, particularly those enriched in leucine codons. We examined significantly downregulated genes in LARS depleted tumors compared to control, with a $\log_2$-fold change cutoff of -0.5. Within these genes, we queried their overall Leu codon content as well as specifically Leu-CTC and Leu-CTG codon content, and also assessed their expression in tumor samples in the TCGA. Gratifyingly, 9 of 13 genes were among the top 50% for either overall Leu codon enrichment, or Leu-CTC or Leu-CTG enrichment, with many ranking in all three categories (Figure 2.24).

GENE	Description	Leucine Enrichment Quartile (SUM)	Leu-CTC Enrichment Quartile	Leu-CTG Enrichment Quartile	Clinical Association (tumor/normal)
Emp3	Epithelial membrane protein 3	1	1	1	↓
Ssna1	Sjoegren syndrome nuclear autoantigen 1 homolog	1	1	2	↑
Gstz1	Maleylacetoacetate isomerase	2	2	1	NS
Ggt5	Glutathione hydrolase 5 proenzyme	2	2	1	↓
Plin1	Perilipin-1	2	3	1	↓
Celf1	CUGBP Elav-like family member 1	2	1	4	NS
Lsp1	Lymphocyte-specific protein 1	3	4	1	NS
Car3	Carbonic anhydrase 3	3	4	2	↓
Lars	Leucyl aminoacyl tRNA synthetase	3	3	3	↓
Tppp3	Tubulin polymerization-promoting protein family member 3	4	4	2	↓
CD163	Scavenger receptor cysteine-rich type 1 protein	4	3	4	NS
Cd36	Platelet glycoprotein 4	4	3	4	↓
Fabp4	Fatty acid-binding protein, adipocyte	4	4	4	↓

Figure 2.24. Relative Leu codon enrichment and clinical significant of downregulated proteomics targets.
A chart depicting significantly downregulated proteins by proteomics in LARS-depleted tumors compared to control. nine of 13 candidates exhibited some enrichment in Leu codons relative to the proteome. Several were additionally significantly downregulated in breast cancer in TCGA.

Among this set, we focused on epithelial membrane protein 3 (EMP3) and gamma glutamyl transferase 5 (GGT5)—two genes that were relatively enriched in Leu-CTC and Leu-CTG codons and whose expression levels are reduced in human breast tumours relative to non-cancerous mammary tissue, suggesting potential roles in suppressing tumourigenesis (Figure 2.25).

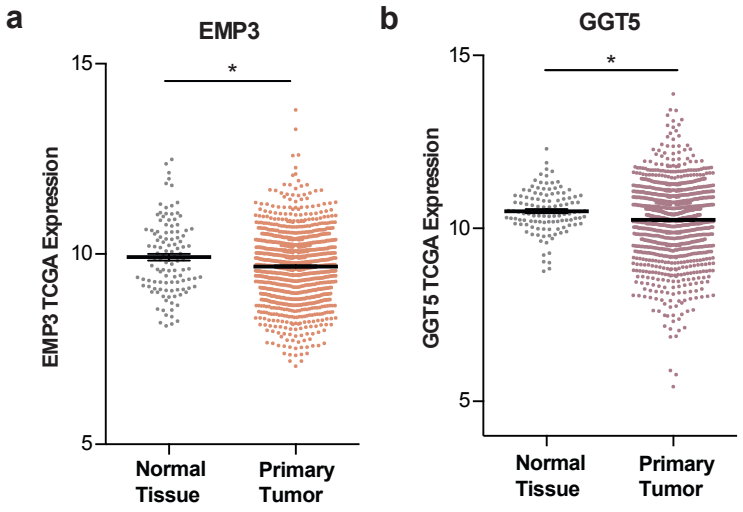

Figure 2.25. Clinical association of candidate downregulated proteins in LARS depleted tumors.
Clinical association of EMP3 (**a**), GGT5 (**b**) in the TCGA database normal breast tissue samples compared to primary tumor. **c-d**, quantification of **a,b** respectively. * = $p < 0.05$, two-tailed Mann-Whitney test. All data are mean ± s.e.m.

To validate our proteomics findings, we assessed protein levels of EMP3 and GGT5 in LARS-depleted PyMT tumors by western blot (Figure 2.26). Consistent with proteomics findings, both were reduced in LARS-depleted tumors compared to control.

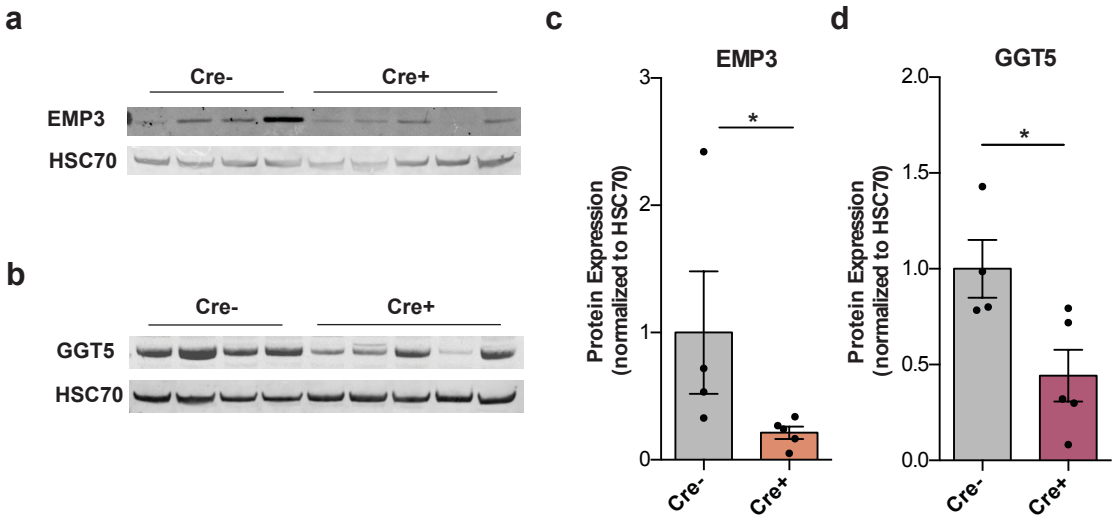

Figure 2.26. EMP3 and GGT5 are reduced in LARS-depleted PyMT tumors.
a-b, Western blot expression of candidate downstream regulators EMP3 and GGT5 in LARS-depleted PyMT tumours. HSC70 is used as a loading control. Samples represent individual mice *Cre-* n=4, *Cre+* n=5. **c,d,** Quantification of **a,b**. Representative of 2 independent experiments, * = $p < 0.05$, one-tailed Mann-Whitney test. Data are mean ± s.e.m.

As an orthogonal approach to validate these findings, we depleted LARS in NMuMG cells using two independent shRNAs. These LARS-depleted cells also exhibited significantly reduced EMP3 and GGT5 protein levels (Figure 2.27). Importantly, EMP3 and GGT5 mRNA abundance was not reduced, suggesting that downregulation of these proteins is specifically due to LARS-mediated translation changes, not mRNA stability or transcriptional downregulation (Figure 2.27). In fact, GGT5 mRNA levels trended towards an increase in NMuMG Lars-depleted cells, suggesting a potential feedback mechanism increasing transcription in response to LARS depletion.

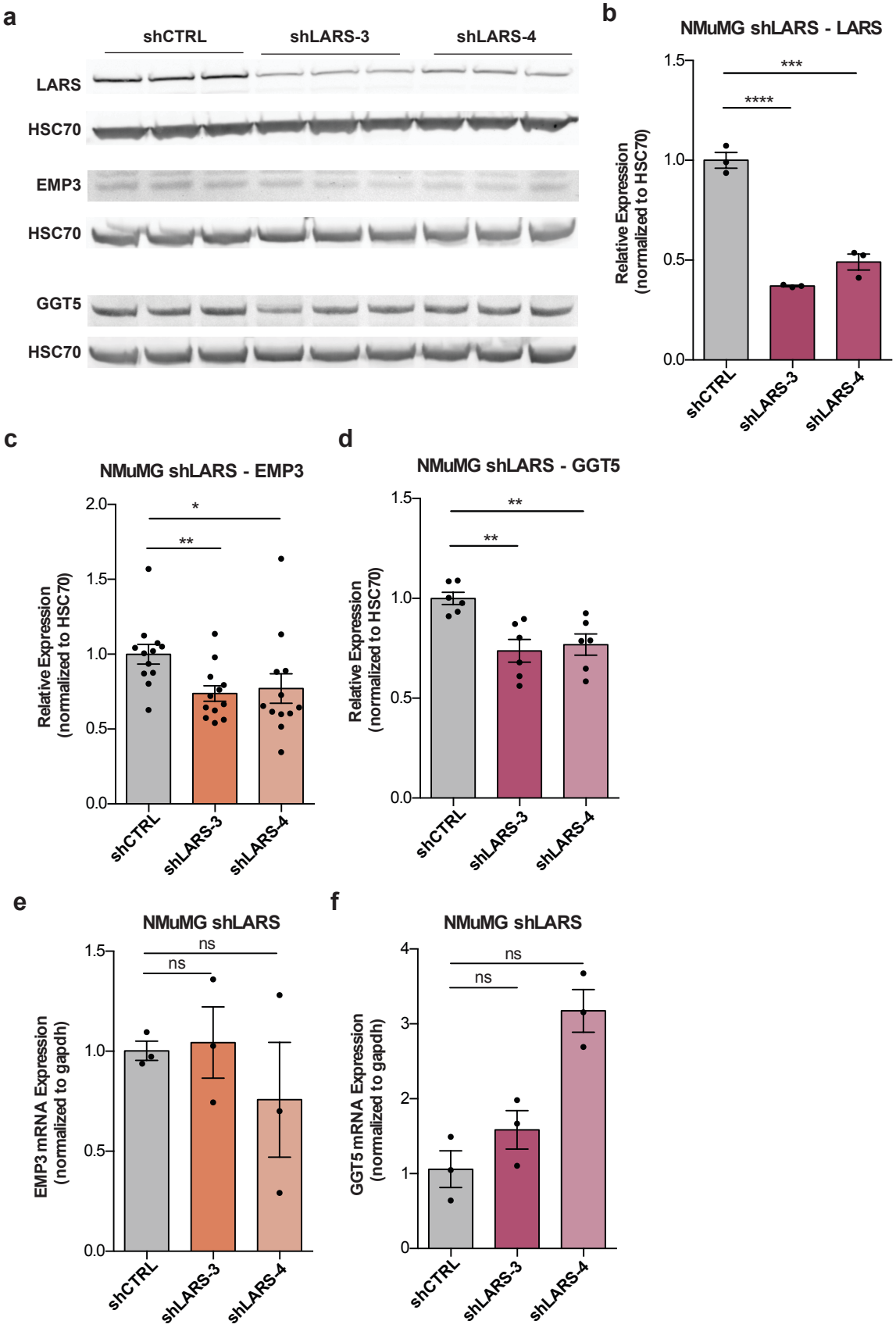
a
shCTRL
shLARS-3
shLARS-4
LARS
HSC70
EMP3
HSC70
GGT5
HSC70
b
NMuMG shLARS - LARS
Relative Expression (normalized to HSC70)
***
****
shCTRL
shLARS-3
shLARS-4
c
NMuMG shLARS - EMP3
Relative Expression (normalized to HSC70)
*
**
d
NMuMG shLARS - GGT5
Relative Expression (normalized to HSC70)
**
**
e
NMuMG shLARS
EMP3 mRNA Expression (normalized to gapdh)
ns
ns
f
NMuMG shLARS
GGT5 mRNA Expression (normalized to gapdh)
ns
ns

Figure 2.27. EMP3 and GGT5 are translationally downregulated in NMuMG-LARS depleted cells.
a, Western blot of LARS, EMP3, and GGT5 in LARS-depleted NMuMg cells. HSC70 is used as a loading control. **b-d,** Quantification of LARS (**b**), EMP3 (**c**) and GGT5 (**d**) in **a. e-f,** mRNA levels of EMP3 (**e**) and GGT5 (**f**) in Lars-depleted NMuMG cells normalized to GAPDH. * = $p < 0.05$, ** = $p < 0.01$, *** = $p < 0.001$, **** = $p < 0.0001$, unpaired two-tailed Student's t-test. Representative of n=3 independent experiments. All data are mean ± s.e.m.

EMP3 is a small transmembrane protein thought to be involved in cell proliferation, and has been implicated in cancer including as a tumor suppressor in certain solid tumours[107,108]. GGT5 is a glutathione metabolism related proenzyme, which has been shown to play a non-cell autonomous role in overcoming chemoresistance in ovarian cancer[109].

To further assess the roles of these proteins in breast proliferative growth, we derived tumour organoids from PyMT mice and transduced them with shRNAs targeting *Emp3* or *Ggt5*. Following transduction, organoids were cultured in Matrigel and growth changes were assessed. Depletion of either EMP3 or GGT5 enhanced organoid growth (Figure 2.28). These findings implicate EMP3 and GGT5 as LARS-regulated tumour suppressors in breast cancer.

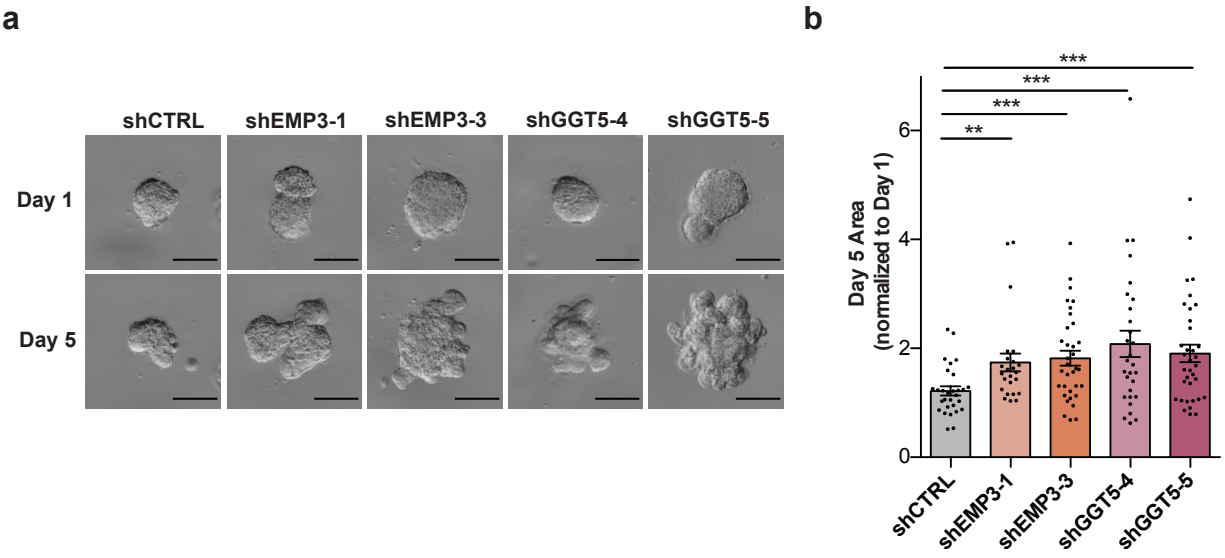

Figure 2.28. EMP3 and GGT5 depletion in PyMT organoids increases 3D growth. **a,** Representative images of PyMT organoids with shRNA knockdown of EMP3 and GGT5, cultured in 3D Matrigel. Scale bar, 100 μm. **b,** Quantification of change in 2D projection of organoid area, normalized to Day 1. Representative of n=3 experiments. Data are mean ± s.e.m. ** = $p < 0.01$, *** = $p < 0.001$, unpaired two-tailed Student's t-test.

Finally, to determine if LARS repression can mediate codon-dependent translation of a downstream target gene, we performed codon-based mutagenesis studies of EMP3. We designed reporter constructs containing EMP3 where Leu-CTC and Leu-CTG—codons for which translation was significantly impacted by LARS depletion—were mutated to the synonymous codon Leu-TTG, a codon for which translation was not significantly impacted upon LARS depletion (Figure 2.29a). We observed that a synonymous codon mutant form of EMP3 was significantly less repressed by LARS depletion, consistent with direct LARS- and Leu-codon-dependent regulation of EMP3 (Figure 2.29b-c). These findings identify EMP3 as a direct Leu codon-dependent target of LARS and confirm the existence of a direct translational regulatory response downstream of LARS in mammary tumour suppression.

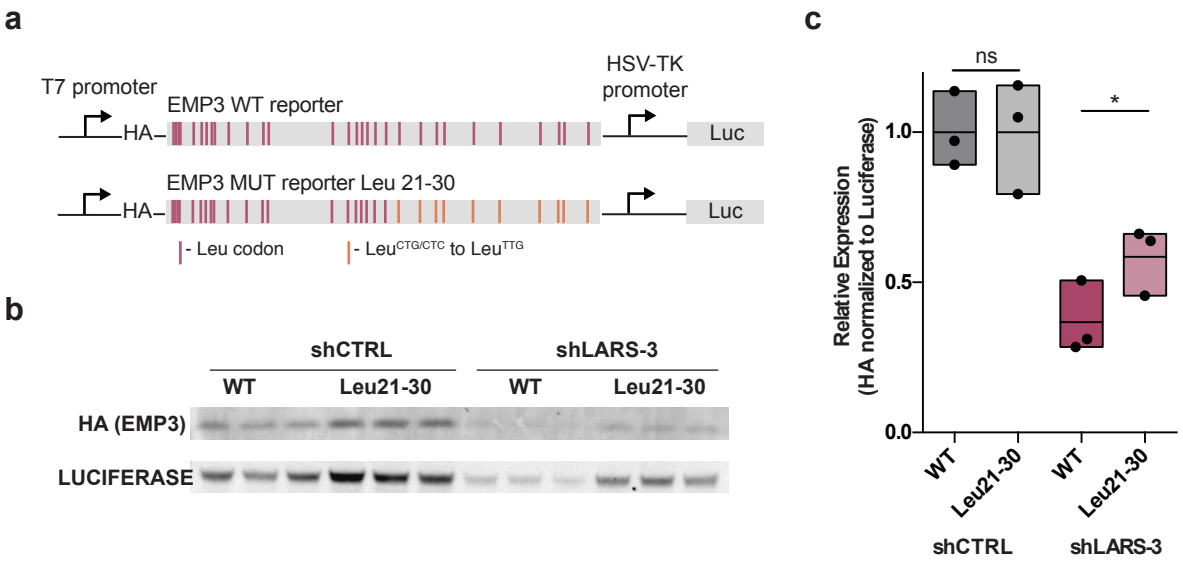

Figure 2.29. EMP3 and GGT5 depletion in PyMT organoids increases 3D growth. **a,** Schematic overview of EMP3 codon reporter design. For leucine codons 21-30 in the gene Leu-CTC and Leu-CTG codons are replaced with Leu-TTG codon. **b,** Western blot for EMP3 reporter expression (HA expression) in NMuMG Lars depleted cell lines. Luciferase is used as a transfection control. Representative of n=4 independent experiments. **c,** quantification of **b**. * = $p < 0.05$, unpaired one-tailed Student's t-test. Data are mean ± s.e.m.

2.7 Summary

Our work identifies LARS, a specific tRNA synthetase, as a breast cancer tumour suppressor. We show that repression of LARS reduces the charging and function of tRNA-Leu^{CAG} to suppress malignant transformation. Depletion of LARS reduced leucine rich protein translation and expression, including that of two candidate genes, EMP3 and GGT5, that we further implicated in tumour suppression and proliferation (Figure 2.30). These findings suggest that LARS regulates a tumour suppressive network. Moreover, they demonstrate that specific repression of a tRNA synthetase can modulate translation of tumour suppressors enriched in a cognate codon.

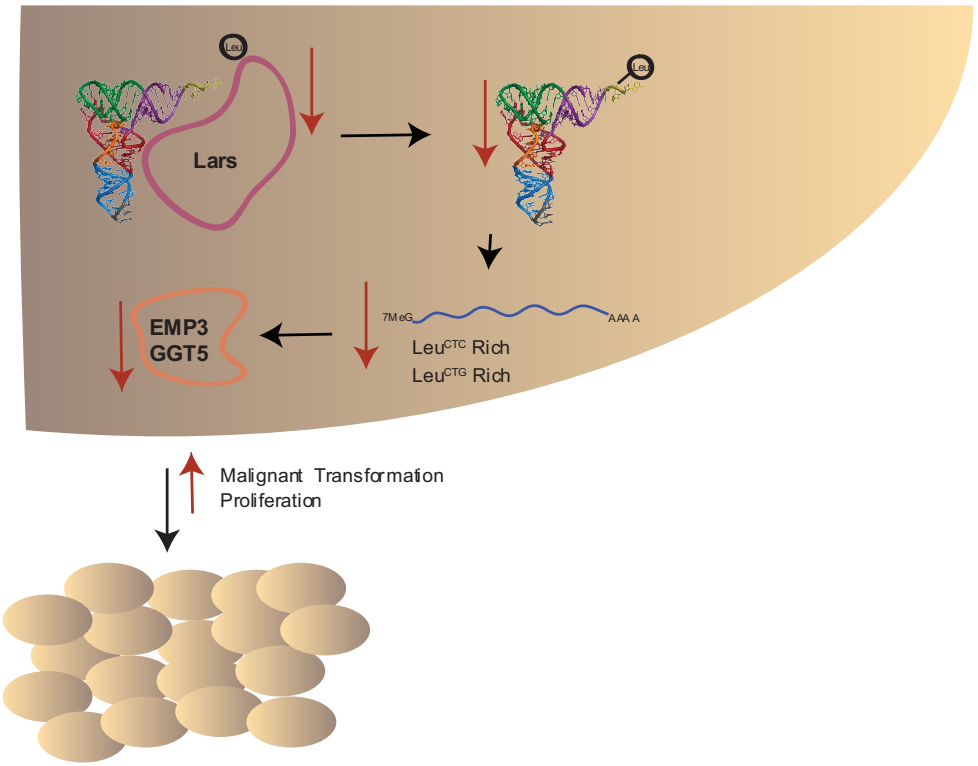

Figure 2.30. Model of LARS-mediated suppression of tumorigenesis.

CHAPTER 3. Stress-induced tyrosine-tRNA depletion through tRNA fragmentation can modulate translation and growth.

3.1 Rationale

Although tRNA fragmentation in response to cellular stress has been well-documented, the functionality of tRFs remains understudied. While tRFs have been implicated in ribosome biogenesis and translation initiation[91,92], they are classically not thought to affect mature tRNA abundance. We sought to identify such exceptions and in this chapter we characterize a tyrosyl-tRNA fragmentation response to oxidative stress that is sufficient to deplete mature tyrosyl-tRNA species and affect gene expression programs, altering cell growth[90].

3.2 Oxidative stress-induced tRNA fragmentation can deplete mature tRNAs

We first sought to identify tRFs generated in response to oxidative stress, that resulted in concomitant decrease in the corresponding tRNA species. We conducted small RNA sequencing as well as tRNA profiling[66] in MCF10A cells at both 8 and 24 hours following hydrogen peroxide (H_2O_2) treatment at 200 μM. While global tRNA levels were unchanged at these time points, several specific tRNAs became repressed (Figure 3.1a). Concomitantly, oxidative stress induced many tRFs (Figure 3.1b). Upon integration of these two approaches, four tRFs were induced alongside reduced mature tRNA populations; of these, we focused on tRNA-Tyr^{GUA}, as the most highly induced tRF (Figure 3.1c).

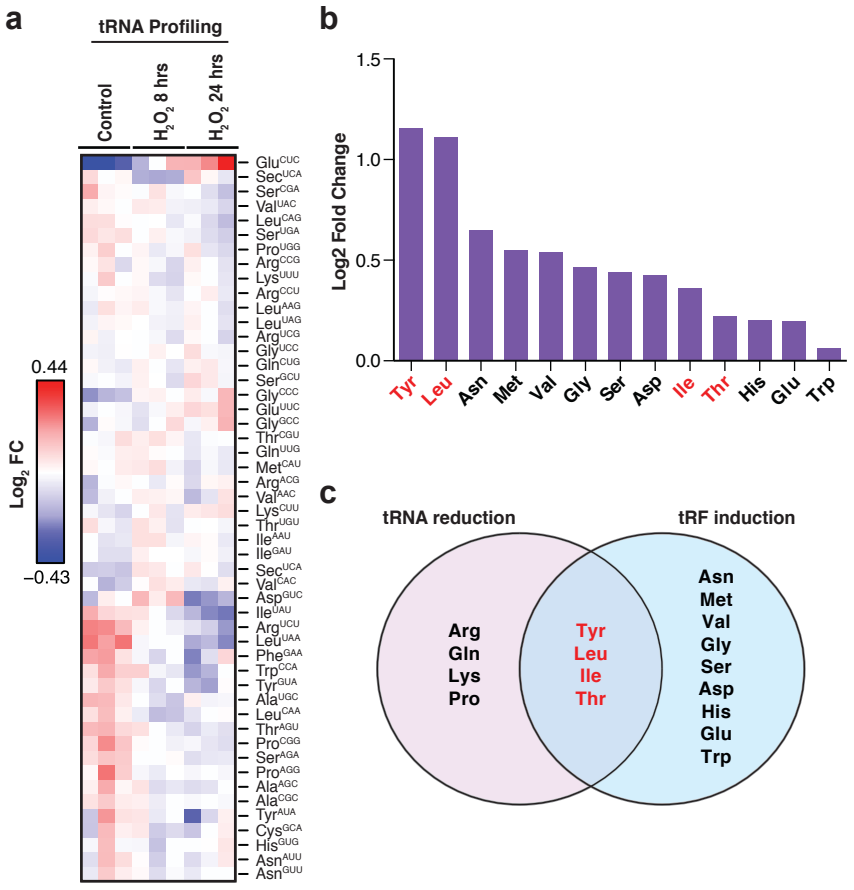

Figure 3.1. identification of modulated mammalian tRNAs and tRFs in response to oxidative stress.

a, Heatmap of tRNA profiling of MCF10A cells at 8 and 24 hours post exposure to oxidative stress (200μM H_2O_2). n=3 per condition. **b**, MCF10A cells were exposed to oxidative stress (200μM H_2O_2) and processed for small RNA-sequencing. The $\log_2$ fold change levels for tRFs derived from distinct tRNA isoacceptors is plotted. **c**, Schematic depicting the overlap of tRNAs in (**a**) that decreased over time with tRFs from (**b**) that were induced. Four isoacceptor families of tRNAs are shown in the overlap with tyrosyl-tRNA and leucyl-tRNAs as the most promising candidates that exhibited the highest degree of tRF induction.

3.3 Oxidative stress-induced fragmentation depletes $tRNA^{Tyr}_{GUA}$

To further validate these findings, we assessed tRF induction and tRNA depletion in a time-course experiment. tRF-Tyr^{GUA} was induced within five minutes of H_2O_2 treatment, with a surprising concomitant reduction in pre-tRNA-Tyr^{GUA} levels, which became nearly undetectable one hour after treatment (Figure 3.2a-b).

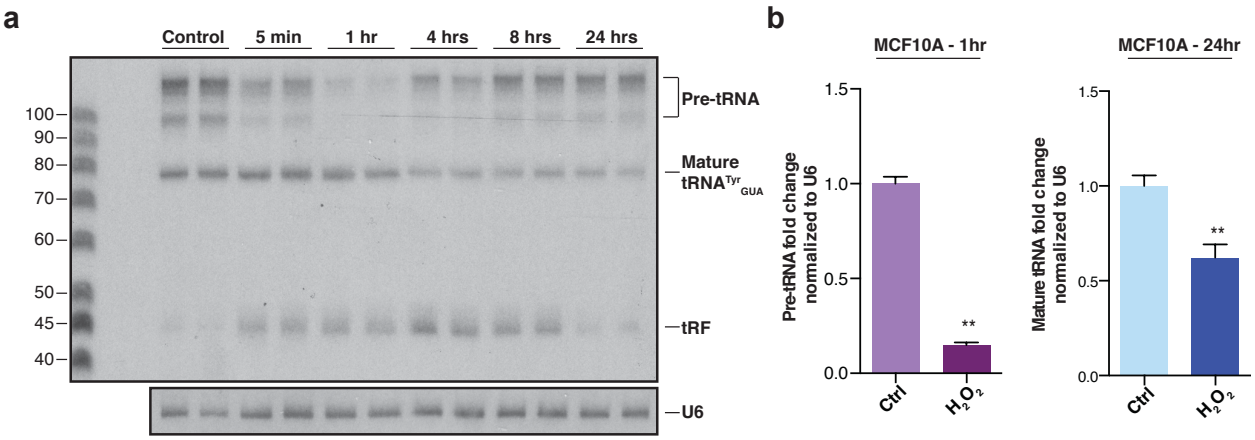

Figure 3.2. tRNA$^{Tyr}_{GUA}$ abundance is reduced while the corresponding Tyr-tRF is induced in response to oxidative stress.
a, Northern blot depicting a time course experiment ranging from five minutes to 24 hours of MCF10A cells in response to oxidative stress. A single probe complementary to pre-tRNA$^{Tyr}_{GUA}$, mature tRNA$^{Tyr}_{GUA}$, and tRF$^{Tyr}_{GUA}$ expression was ^{32}P-labeled and used for detection. **b**, Quantification of pre-tRNA$^{Tyr}_{GUA}$ northern blot analysis from multiple independent experiments after one hour as well as mature tRNA$^{Tyr}_{GUA}$ levels after 24 hours (normalized to U6 levels) are shown (n=6).

This data suggests that tRF-Tyr^{GUA} is generated from the pre-tRNA, rather than the mature tRNA. By contrast, a 50% reduction in mature tRNA-Tyr^{GUA} was observed following 24 hours of treatment, which is likely a result of the stability of mature tRNAs (Figure 3.2). These findings demonstrate that oxidative stress-induced generation of tRF-Tyr^{GUA} can ultimately significantly deplete the corresponding mature tRNA-Tyr^{GUA} pool. Furthermore, we show that a single cellular stress can induce the levels of a specific tRF and deplete its corresponding tRNA.

We next wondered whether the observed tRNA-Tyr^{GUA} depletion was transient or if it could persist in continuous stress exposure. Surprisingly, following five days of daily H_2O_2 treatment, cells maintained both a 50% tRNA-Tyr^{GUA} repression and tRF-Tyr^{GUA} induction (Figure 3.3a-b). By contrast, other tRNA species , including tRNA-His^{GUG} and tRNA-Glu^{YUC}, remained stable over this time period (Figure 3.2a,c-d).

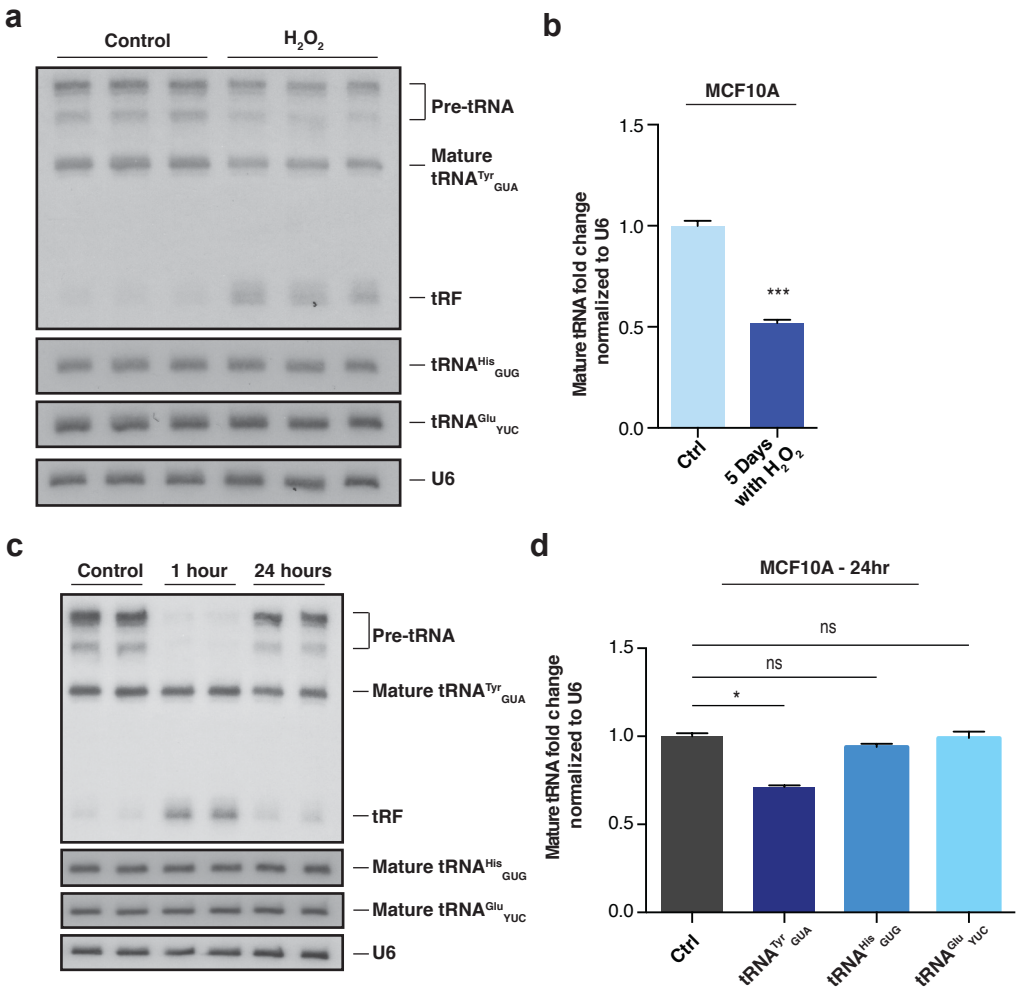

Figure 3.3. tRNA-Tyr^{GUA} fragmentation is sustained with continuous stress and is not generalizable to all tRNAs.

a, northern blot depicting MCF10A cells that were exposed to oxidative stress (200μM H_2O_2) once daily for five continuous days to test if repeated exposure to the stress could elicit sustained fragmentation. **b**, Quantification of mature tRNA-Tyr^{GUA} bands by northern blot after cells were treated once daily for five continuous days (normalized to U6) from multiple independent experiments (n=12). **c**, A northern blot depicting two time points, one hour and 24 hours, after exposure to oxidative stress (200 μM H_2O_2) in MCF10A cells. As before, a single probe complementary to pre-tRNA-Tyr^{GUA}. mature tRNA-Tyr^{GUA}, and tRF-Tyr^{GUA} was while another probe complementary to either the mature tRNA-His^{GUG} or mature tRNA-Glu^{YUC} were both ^{32}P-labeled and used for detection. **d,** Quantification of tRNA-Tyr^{GUA}, tRNA-His^{GUG}, and tRNA-Glu^{YUC} by northern blot analysis from two independent experiments 24 hours (normalized to U6 levels) after exposure to oxidative stress (200 μM H_2O_2) are shown (n=4). Data represent mean ± s.e.m. A one-tailed Mann-Whitney test was used to test for statistical significance between the treated and control cell lines for each time point.

To determine the generalizability of these results, we also measured the effects of oxidative stress on tRNA-Tyr species in a distinct mammalian cell line, the human bronchial epithelial cell line (HBEC30). Consistent with MCF10A data, we observed that pre-tRNA-Tyr^{GUA} levels dramatically declined at 1-hour post treatment, with a corresponding significant reduction in mature tRNA-Tyr^{GUA} levels at 24 hours (Figure 3.4).

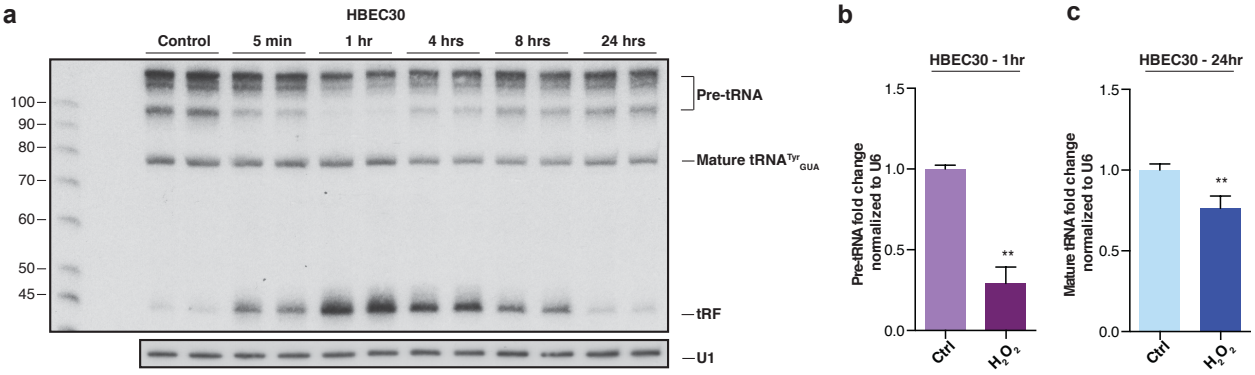

Figure 3.4. tRNA-Tyr^{GUA} fragmentation occurs within additional cell lines.
a, northern blot depicting a time course experiment ranging from five minutes to 24 hours for HBEC30 cells in response to oxidative stress (200µM H_2O_2). As before, a single probe complementary to pre- tRNA-Tyr^{GUA}, mature tRNA-Tyr^{GUA}, and tRF-Tyr^{GUA} was ^{32}P-labeled and used for detection. **b-c**, Quantification of northern blot analysis for pre-tRNA-Tyr^{GUA} (**b**) and tRF-Tyr^{GUA} (**c**) after one hour and 24 hours respectively in HBEC30 cells upon exposure to oxidative stress (200µM H_2O_2) (n=6). Data represent mean ± s.e.m. A one-tailed Mann-Whitney test (*$p < 0.05$ and **$p < 0.01$) was used to test for statistical significance between the treated and control cell lines for each time point.

To determine if tRF-Tyr^{GUA} formation is conserved across species, we exposed *C. elegans* to H_2O_2. Consistent with our observations in human cells, tRNA-Tyr^{GUA} was induced following 15 minutes of treatment (Figure 3.5). This suggests that tyrosyl-tRNA fragmentation is conserved in nematodes, highlighting the significance of this phenomenon.

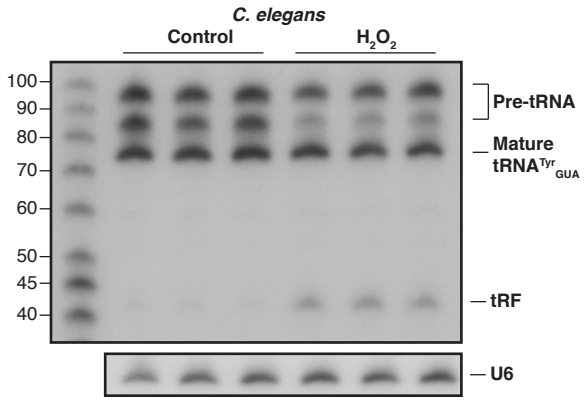

Figure 3.5. tRNA-Tyr^{GUA} fragmentation in response to oxidative stress is conserved across species.
Northern blot for tRF-Tyr^{GUA} in *C. elegans* cells at 15 minutes post-oxidative stress (200μM H_2O_2) exposure.

We also tested independent sources of oxidative stress, to further confirm the mechanism of tRNA-Tyr^{GUA} fragmentation. Similar to H_2O_2 treatment, menadione reduced pre-tRNA and induced the tRF at early time points, whereas mature tRNA-Tyr^{GUA} was depleted after 24 hours (Figure 3.6). Taken together, these findings reveal that stress-induced tRNA depletion can be a sustained response and that it can be elicited in multiple human cell types.

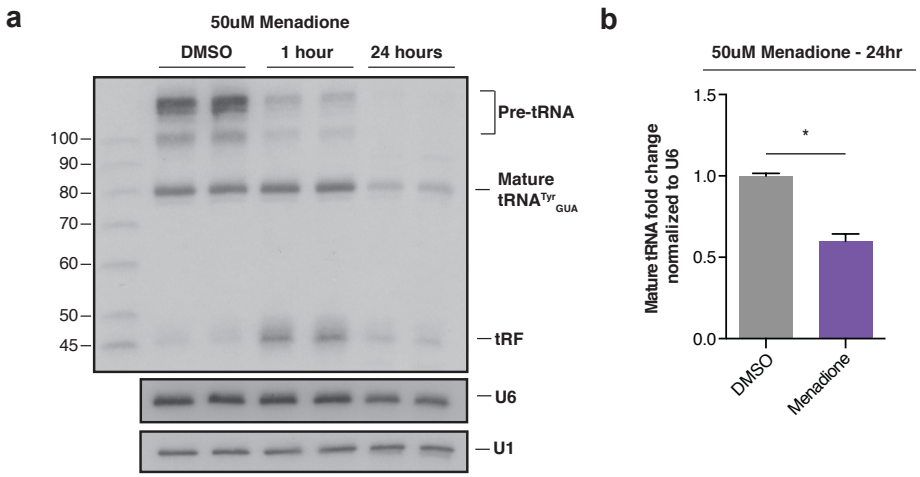

Figure 3.6. tRNA-Tyr^{GUA} fragmentation occurs with other sources of oxidative stress. **a**, Northern blot at a short and longer time point after MCF10A cells were treated with a pharmacological agent used to induce oxidative stress(menadione). **b**, Quantification of tRNA-Tyr^{GUA} by northern blot analysis form two independent experiments 24 hours (normalized to U6 levels) after exposure to oxidative stress (50μM menadione) are shown (n=4). A one-tailed Mann-Whitney test was used to test for statistical significance. Data represent mean ± s.e.m.

3.4 Oxidative stress-induced tRNA-Tyr^{GUA} depletion represses cellular growth.

Next, we sought to further characterize the observed tRNA-Tyr^{GUA} depletion effects. To rule out the possibility that mature tRNA depletion was due to cell death, we conducted cell growth and viability assays following H_2O_2 treatment. We observed no difference in cell viability following treatment at the doses and time points studied, reducing the possibility of cell death as a mediator of mature tRNA depletion (Figure 3.7a). Further, cell death is an unlikely contributor given that only specific tRNAs were depleted. Given that the dose of H_2O_2 used did not reduce cell viability, and that only specific tRNAs were depleted, we deemed it unlikely that the observed effects were due to cell death. However, we observe substantial growth defects upon H_2O_2 treatment (Figure 3.7b). As a result, we wondered if tRNA-Tyr^{GUA} depletion may contribute to growth repression phenotypes.

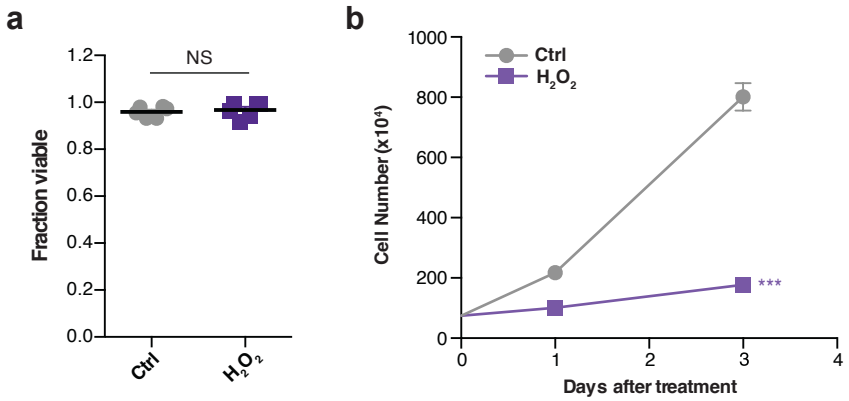

Figure 3.7. Oxidative stress represses cell growth but does not affect cell viability.
a, The viability of MCF10A cells after H_2O_2 treatment (200μM) was tested by a trypan blue exclusion assay (n=6). Viability was tested one hour after exposure to oxidative stress. A two-tailed Mann-Whitney test was used to test for statistical significance between the treated and control cell lines. **b**, Growth curves of MCF10A cells exposed to oxidative stress (200 μM H_2O_2) relative to control cells (n=3). Two-way ANOVA was used to test for significance. All data represent mean ± s.e.m.

To assess the effects of tRNA-Tyr^{GUA} reduction on cell growth, we used two orthogonal approaches. We first depleted tRNA-Tyr^{GUA} using shRNA[66], and confirmed a 50% reduction in tRNA level using this approach (Figure 3.8a). We also depleted tyrosyl-tRNA synthetase (YARS) with two independent shRNAs, to deplete tRNA-Tyr^{GUA} functionally through reduced tRNA charging (Figure 3.8b). Both of these approaches were sufficient to suppress cell growth in MCF10A cells compared to control (Figure 3.8c).

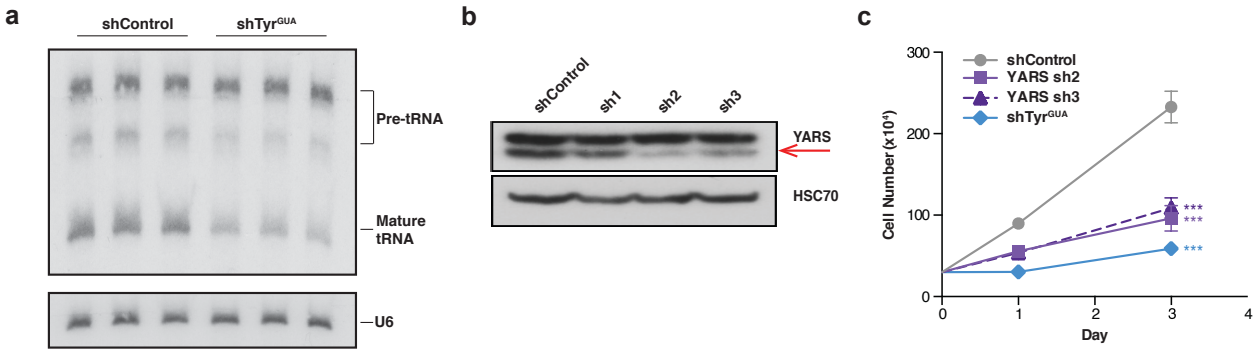

Figure 3.8. tRNA-Tyr^{GUA} depletion and YARS depletion repress cell growth.
a, The viability of MCF10A cells after H_2O_2 treatment (200 μM) was tested by a trypan blue exclusion assay (n=6). Viability was tested one hour after exposure to oxidative stress. A two-tailed Mann-Whitney test was used to test for statistical significance between the treated and control cell lines. **b**, Growth curves of MCF10A cells exposed to oxidative stress (200 μM H_2O_2) relative to control cells (n=3). Two-way ANOVA was used to test for significance. **c**, (D) Growth curves of MCF10A cells expressing RNAi against mature tRNA-Tyr^{GUA} or YARS relative to cells expressing a control hairpin (n=3). Two-way ANOVA was used to test for significance. All data represent mean ± s.e.m.

These results demonstrate that tRNA-Tyr^{GUA} depletion can significantly impair growth, phenocopying H_2O_2-induced physiological depletion of endogenous tRNA-Tyr^{GUA}. Overexpression of tRNA-Tyr^{GUA,} on the other hand, led to increased cell growth (Figure 3.9). These data imply that stress-induced tRNA-Tyr^{GUA} depletion is growth-suppressive, and may contribute to a cellular oxidative stress program.

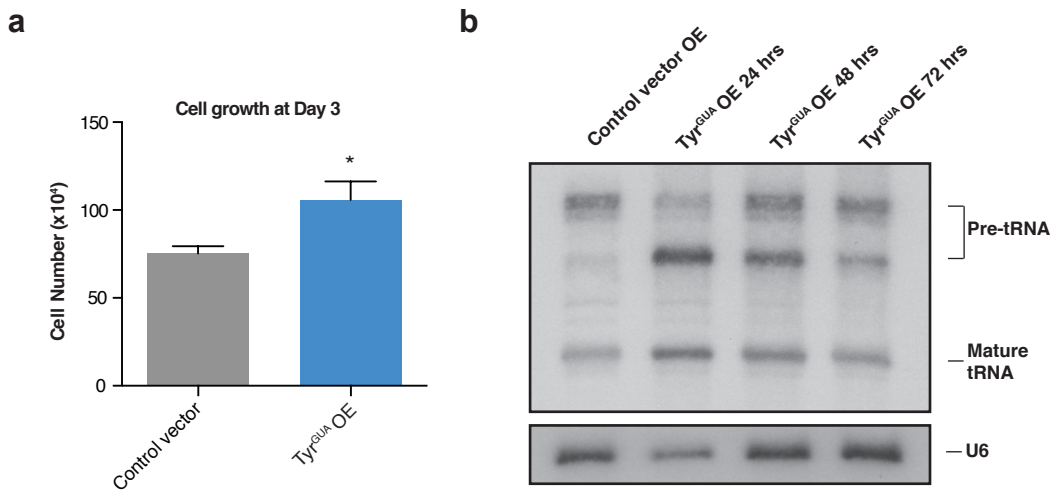

Figure 3.9. tRNA-Tyr^{GUA} overexpression increases cell growth.
a, Cell growth of MCF10A cells transiently transfected with a tRNA-Tyr^{GUA} overexpression vector relative to an empty control vector (n=3). A one-tailed Mann-Whitney test was used to test for significance at day 3. **b**, Northern blot of MCF10A cells transiently transfected with a tRNA-Tyr^{GUA} overexpression vector relative to an empty control vector. tRNA-Tyr^{GUA} overexpression is shown at 24, 48, and 72 hours post transfection. Data represent mean ± s.e.m. *p < 0.05, **p < 0.01, and ***p < 0.001

3.5 tRNA-Tyr^{GUA} depletion represses candidate growth-related genes.

We hypothesized that stress-induced tRNA$^{Tyr}_{GUA}$ depletion impairs growth through reduction of relatively tyrosine-rich proteins. To identify potential candidates, we assessed protein expression by label-free proteomics in tRNA-Tyr^{GUA} or YARS-depleted MCF10A cells compared to control. There was a significant correlation between differentially expressed proteins in each of these groups (R=0.648; p < 2.2 e-16), confirming the overlap in these orthogonal methods of tRNA$^{Tyr}_{GUA}$ loss-of-function (Figure 3.10a). Among depleted candidates, we specifically searched for relatively Tyr-enriched proteins, which were most likely to be tRNA-Tyr^{GUA} dependent (Figure 3.10b). Using this approach, we identified 102 tyrosine-enriched candidate proteins.

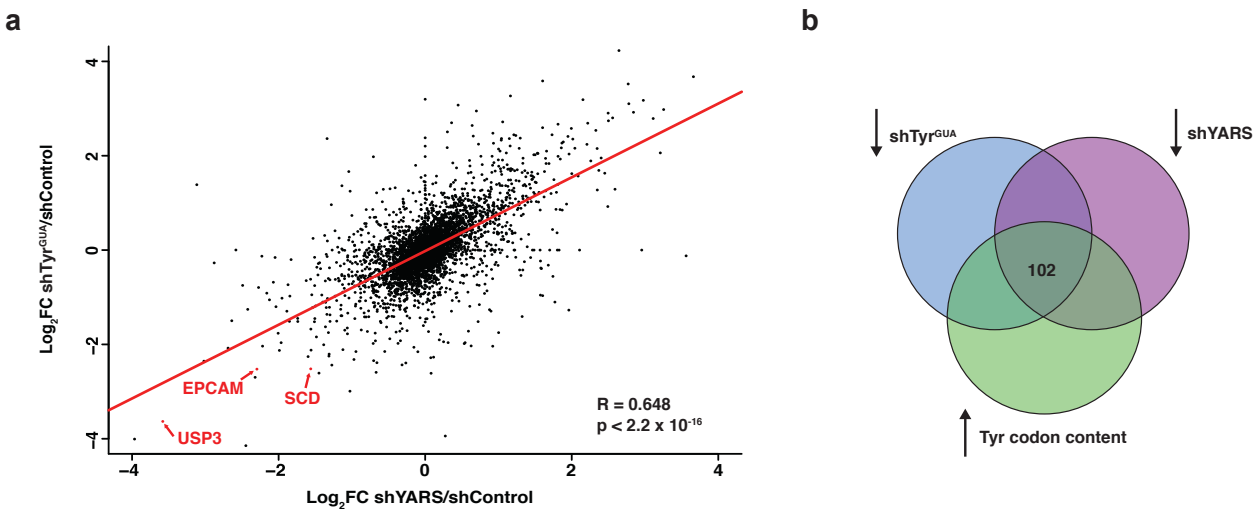

Figure 3.10. Proteomic analysis identifies downregulated Tyr-rich proteins within tRNA-Tyr^{GUA} -depleted and YARS-depleted cells.
a, A plot showing the correlation between protein abundance changes in the proteome upon either tRNA-Tyr^{GUA} depletion or YARS depletion (shYARS-2) relative to control cells. A Pearson's two-sided test was used to test determine the statistical significance of the correlation between tRNA-Tyr^{GUA} and YARS depletion effects across the detected proteome. **b**, Cells depleted of tRNA-Tyr^{GUA} or YARS were processed for label free quantitation by mass spectrometry to identify proteins that were reduced by a $\log_2$-fold change of 0.5 or more. This set was overlapped with proteins containing a higher than median abundance of Tyr codon content to identify candidate mediators of the pleiotropic effects of tRNA-Tyr^{GUA} depletion.

To further characterize these 102 candidates, we conducted Gene Ontology functional analysis[110]. Consistent with our growth repression findings, we observed that the most significantly enriched GO terms included those associated with cellular growth, including regulation of ATP synthesis, G0 to G1 cell-cycle progression, and phosphorylation (Figure 3.11). These findings demonstrate that tRNA-Tyr^{GUA} depletion represses the expression of candidate growth-related proteins.

GO terms	Description	p-value
GO:0042775	mitochondrial ATP synthesis coupled electron transport	3.30E-03
GO:0042773	ATP synthesis coupled electron transport	3.56E-03
GO:0007626	locomotory behavior	6.17E-03
GO:0070316	regulation of G0 to G1 transition	6.63E-03
GO:0045184	establishment of protein localization	6.65E-03
GO:0022904	respiratory electron transport chain	7.00E-03
GO:0006497	protein lipidation	8.98E-03
GO:0042475	odontogenesis of dentin-containing tooth	8.98E-03
GO:0042886	amide transport	9.17E-03
GO:0016310	phosphorylation	9.18E-03
GO:0006119	oxidative phosphorylation	9.42E-03

Figure 3.11. GO-functional analysis associates growth-related activities with Tyr-rich proteins depleted in tRNA-Tyr^{GUA} -depleted and YARS-depleted cells.
GO-functional analysis of the 102 candidate gene set from Figure 3.10.

Within these candidate proteins, we selected a small set of tRNA-Tyr^{GUA} –regulated genes that exhibited some of the greatest fold reductions upon tRNA-Tyr^{GUA} depletion for further functional studies (Figure 3.12a). These genes comprised ubiquitin specific protease 3 (USP3), a hydrolase that deubiquitinates histone H2A and H2B and is required for mitotic entry and S phase progression[111], epithelial cell adhesion molecule (EPCAM), a tumorigenic cell surface protein over-expressed in many carcinomas[112], and stearoyl-CoA desaturase (SCD), the rate limiting enzyme for generating mono-unsaturated fatty acids such as palmitoleate and oleate—principle components of membrane phospholipids and cholesterol esters[113]. Quantitative western blotting and quantitative real time PCR (qRT-PCR) revealed significant reductions in the endogenous levels of these proteins and mRNA transcripts upon shRNA-mediated depletion of tRNA-Tyr^{GUA} or YARS (Figure 3.12b-d). In contrast, the control protein HSC70 was not significantly depleted, consistent with our findings of a specific set of modulated proteins upon tRNA-Tyr^{GUA} depletion.

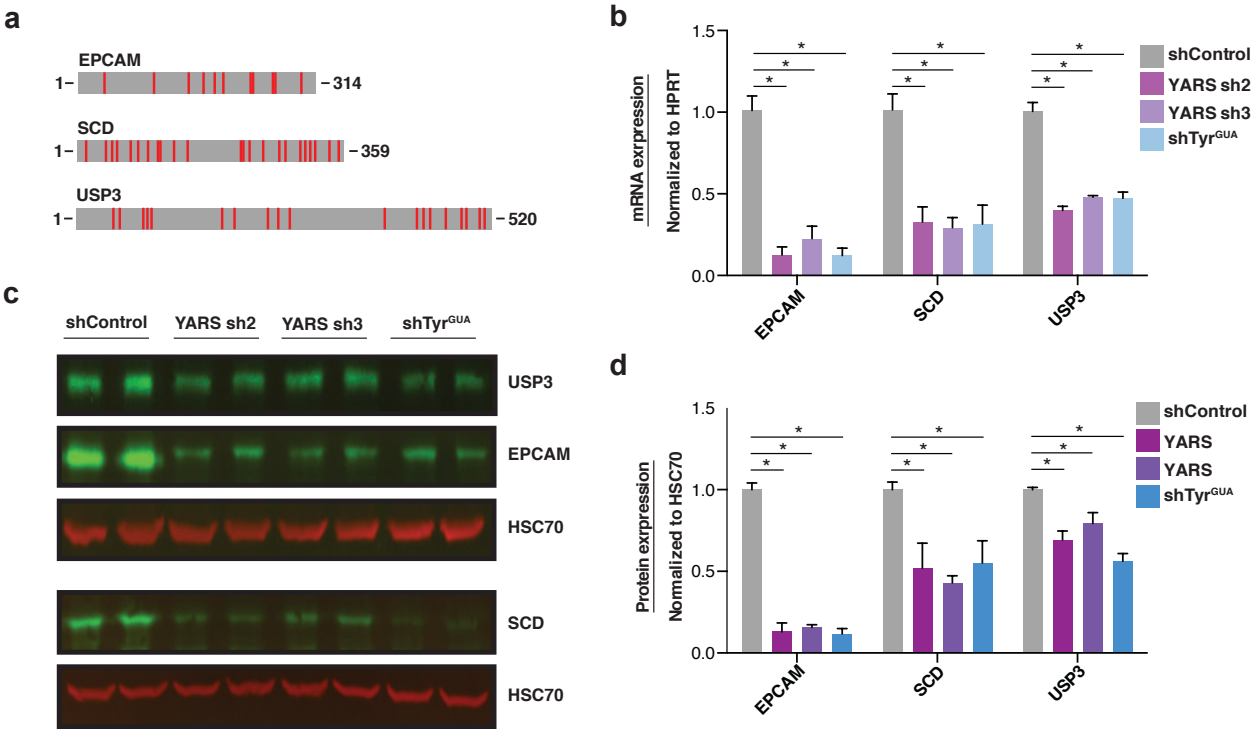

Figure 3.12. Candidate proteins EPCAM, SCD and USP3 are depleted in tRNA-Tyr^{GUA} -depleted and YARS-depleted cells.
a, A schematic showing locations of all tyrosine residues in the coding sequence of three target genes, EPCAM, SCD, and USP3. **b,** Levels of mRNA expression for target genes in cells depleted of either tRNA-Tyr^{GUA} or YARS as measured by qRT-PCR (n=4). **c,** Quantitative western blot validation depicting abundances of protein targets (EPCAM, SCD, and USP3). HSC70 was used as a loading control and is not modulated upon molecular perturbation of tRNA-Tyr^{GUA}. **d,** Quantification of western blot analysis in (**c**) (n=4). A one-tailed Mann-Whitney test was used to test for statistical significance between knockdown and control conditions. Data represent mean ± s.e.m. *$p < 0.05$, **$p < 0.01$, and ***$p < 0.001$.

To determine if repression of these genes affects proliferation, we conducted cell growth assays in the context of RNAi-mediated gene depletion. Knockdown of each gene by two independent oligos was sufficient to reduce cell growth in MCF10A cells (Figure 3.13). Our results reveal that repressing the function of a specific tRNA reduces expression of a candidate set of tyrosine enriched proteins enriched in growth-dependent processes. Moreover, depletion of tRNA-Tyr^{GUA} or its downstream regulated genes impairs growth of breast epithelial cells. We propose that this network constitutes a pro-growth tRNA-Tyr^{GUA}-regulated pathway, and its repression via stress-

induced tRNA fragmentation and tRNA depletion constitutes an adaptive growth suppressive stress response.

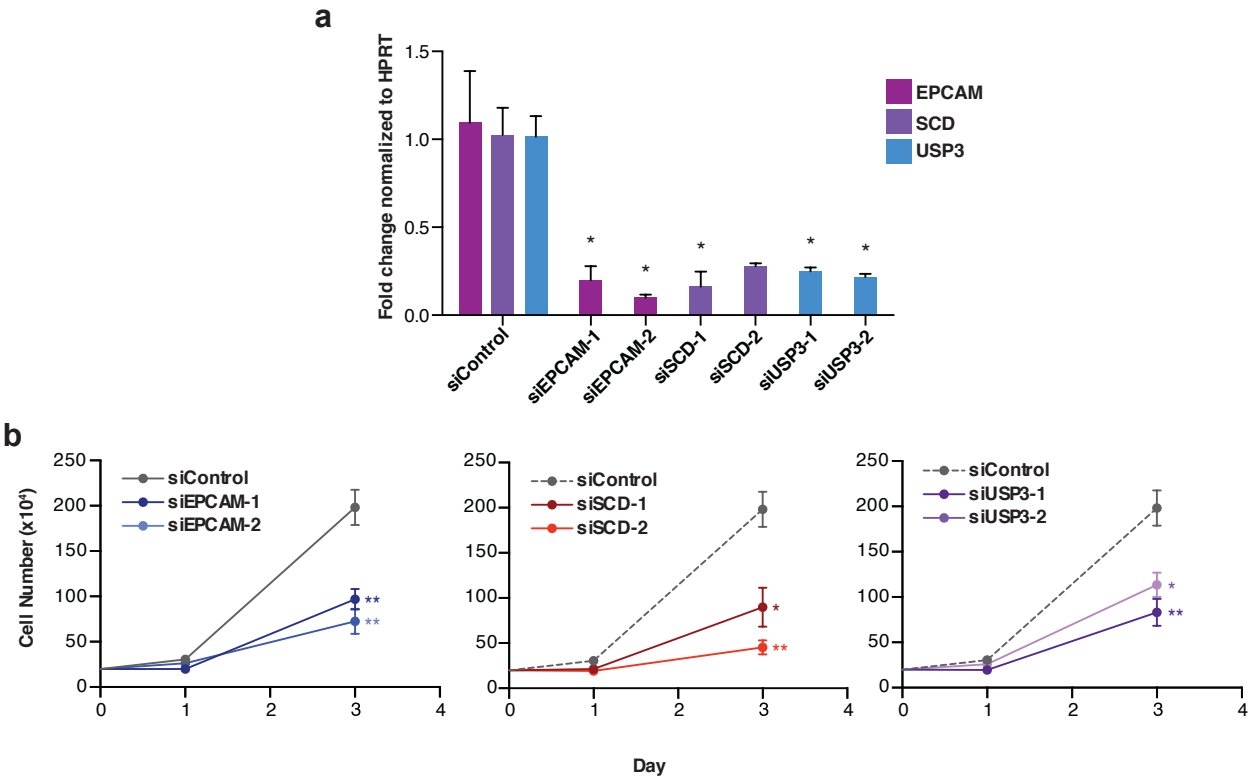

Figure 3.13. Depletion of candidate Tyr-rich proteins by RNAi represses growth. **a**, Total mRNA from MCF10A cells transiently transfected with two independent siRNA targeting EPCAM, SCD, or USP3 was analyzed by quantitative RT-PCR at the end of each growth assay. A one-tailed Mann-Whitney test was used to establish statistical significance (n=3 except for siSCD-2 has n=2). **b**, Growth curves for MCF10A cells were transfected with either control siRNA or two independent siRNA targeting EPCAM, SCD, or USP3. Note that the control cell growth curve is the same in all graphs and were plotted separately for clarity and does not represent independent experiments. Two-way ANOVA was used to test for significance. All data represent mean ± s.e.m. *$p < 0.05$

3.6 tRNA-Tyr^{GUA} depletion impairs protein translation in a codon-dependent manner.

Thus far, we demonstrate that tRNA-Tyr^{GUA} expression regulates abundance of tyrosine-enriched growth-related proteins. We wondered whether these proteins would also be sensitive to oxidative stress-induced tRNA-Tyr^{GUA} depletion. To test this hypothesis, we assessed candidate protein expression by western blot following 24 hours of H_2O_2 treatment. Consistent with our previous

experiments, we noted significant reductions in protein expression of SCD, EPCAM and USP3 (Figure 3.14a-b). Despite these reductions at the protein level, the transcript levels of two of these three downstream genes were not significantly altered upon H_2O_2 treatment (Figure 3.14c), suggesting that tRNA-Tyr^{GUA} depletion results in repression of specific growth-regulatory target genes at the translational level.

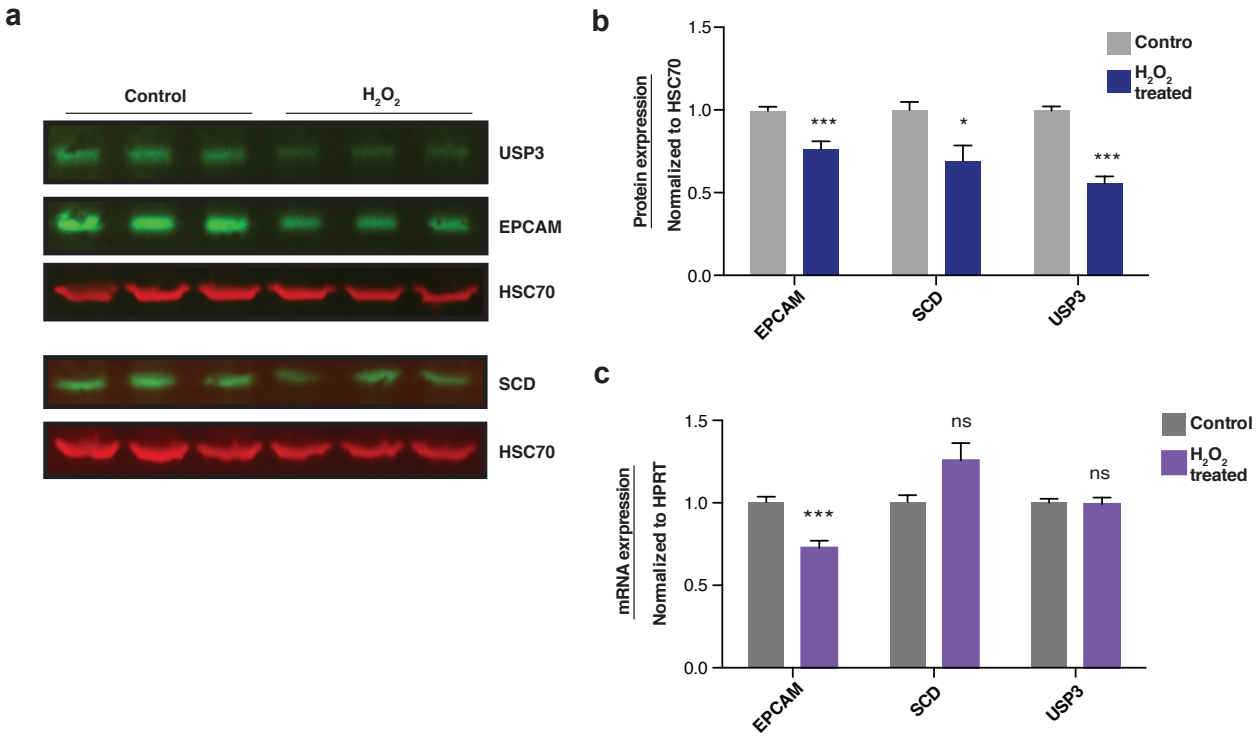

Figure 3.14. Oxidative stress reduces candidate Tyr-rich protein expression.
a, Quantitative western blot EPCAM, SCD, and USP3 in MCF10A cells 24 hours after treatment with H_2O_2 (200μM). HSC70 was used as a loading control. **b**, Quantification of western results in (**a**) (n=9). **c**, mRNA expression levels for target genes 24 hours after treatment with H_2O_2 (200μM) as measured by qRT-PCR (n=9). A one-tailed Mann-Whitney test was used to test for statistical significance between the treated and control conditions. Data represent mean ± s.e.m. *$p < 0.05$, **$p < 0.01$, and ***$p < 0.001$

To test whether tRNA-Tyr^{GUA} modulation directly impacts gene regulation at the translational level, we employed two approaches. In the first, we designed a codon-dependent reporter of USP3. A Myc-tagged USP3 coding sequence was cloned upstream of a Luciferase transfection control.

The cloned USP3 sequence was either wild-type (WT) or a mutant variant, which contained 5 tyrosine codons mutated to alanine codons (Figure 3.15a). We hypothesized that if USP3 was sensitive to, and directly regulated by tRNA-Tyr^{GUA} modulation, then mutating its tyrosine codons would reduce its susceptibility to stress-induced gene repression. These reporters were transfected into MCF10A cells and 24 hours after H_2O_2 treatment quantitative western blotting was performed. Consistent with our model of codon-dependent translation regulation, we observed a significant increase in the abundance of the mutant USP3 relative to the WT version of the protein (Figure 3.15b).

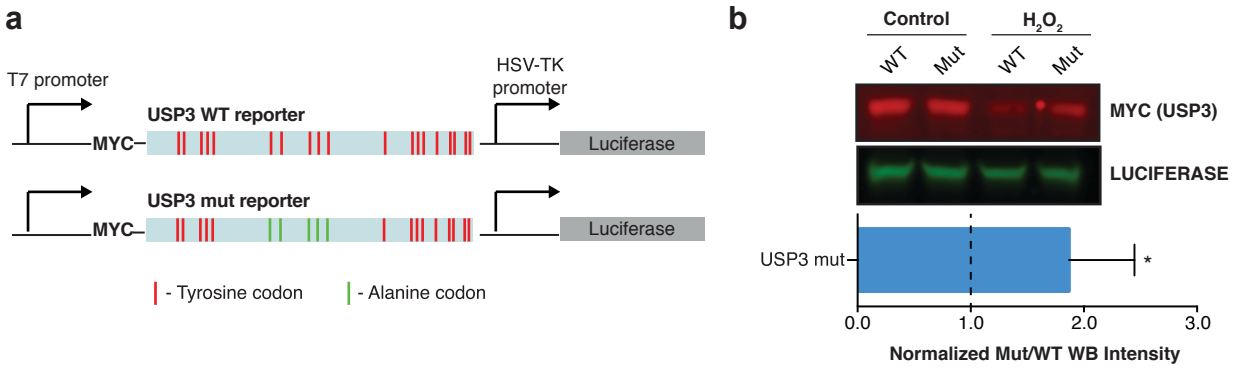

Figure 3.15. Codon reporter assays demonstrate codon-dependent translation regulation of Tyr-rich genes under oxidative stress.
a, A schematic of the codon-based USP3 reporter. A Myc-tagged WT or mutant reporter with 5 Tyr codons mutated to Ala codons were cloned upstream of a Luciferase used for transfection normalization. **b**, Quantitative western blot for the Myc-tag and Luciferase (top) with normalized fluorescent intensities (bottom) are shown (n=3). Data represent mean ± s.e.m. *p < 0.05, **p < 0.01, and ***p < 0.001

That protein expression is sensitive to tRNA-Tyr^{GUA} abundance as well as YARS expression suggests that modulations occurs at the translational level. Thus, we performed ribosomal profiling in tRNA-Tyr^{GUA} -depleted cells compared to control, to test if ribosomal occupancy is altered on tyrosine-rich transcripts[105]. We compared the ribosome protected fragments (RPFs) detected in cells with and without tRNA-Tyr^{GUA} depletion, in order to examine the global translational effects due to modulating this single tRNA. We observed similar length distribution

and nucleotide periodicity for ribosome-protected fragments as those of previous studies[105] (Figure 3.16).

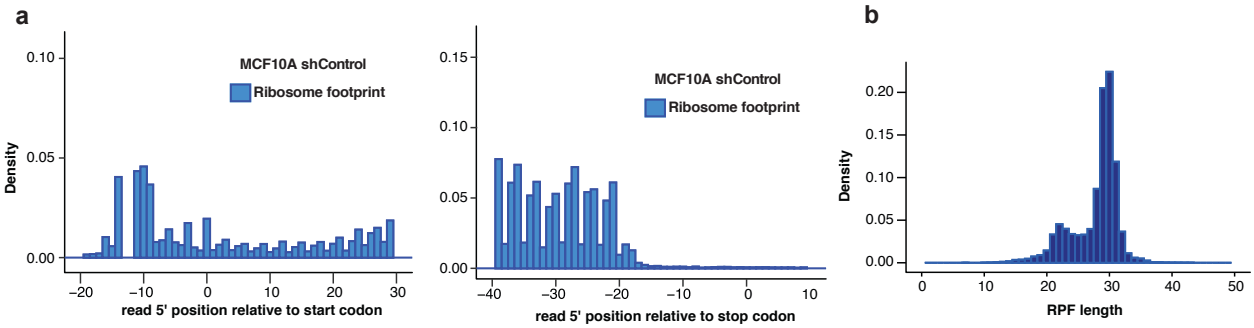

Figure 3.16. Ribosome protected fragments from tRNA-Tyr^{GUA} -depleted cells demonstrate expected length distribution and nucleotide periodicity.
a, Examples of the mapped position of the 5'-end of reads near the start (left) or stop (right) codons are shown, revealing the characteristic 3-nucleotide periodicity of ribosomal positioning observed as previously described. **b**, Histogram of the read length distribution of ribosome protected fragments observed upon ribosome profiling sequence analysis.

Non-optimal or rare tRNAs are thought to induce ribosome stalling when the corresponding codon in the ribosomal A site[114]. We therefore wondered whether tRNA-Tyr^{GUA} depletion could induce such stalling at corresponding tyrosine codons. We examined RPF reads from the 20-22nt RPFs—representing ribosomes with an empty A site[115]—and observed an increase of reads containing tyrosyl UAC or UAU codons in tRNA-Tyr^{GUA} –depleted cells compared to control cells (Figure 3.17a). In parallel, we estimated translation efficiency for each gene, a ratio between RPFs and mRNA expression, and asked whether this differed for relatively Tyr-rich transcripts between control and tRNA-Tyr^{GUA} –depleted cells. Genes were ranked by translataion efficiency and binned into three sets, and we queried tyrosine codon content in each group. Consistent with ribosome stalling analysis, we found that genes with higher tyrosine codon count were significantly enriched in the set of genes with the lowest translational efficiency (denoted by the lowest red bar) upon tRNA-Tyr^{GUA} depletion (Figure 3.17b). These findings reveal that ribosomal

translation of a set of tyrosine codon-enriched genes in these mammalian cells is sensitive to depletion of tRNA-Tyr^{GUA} to physiological levels.

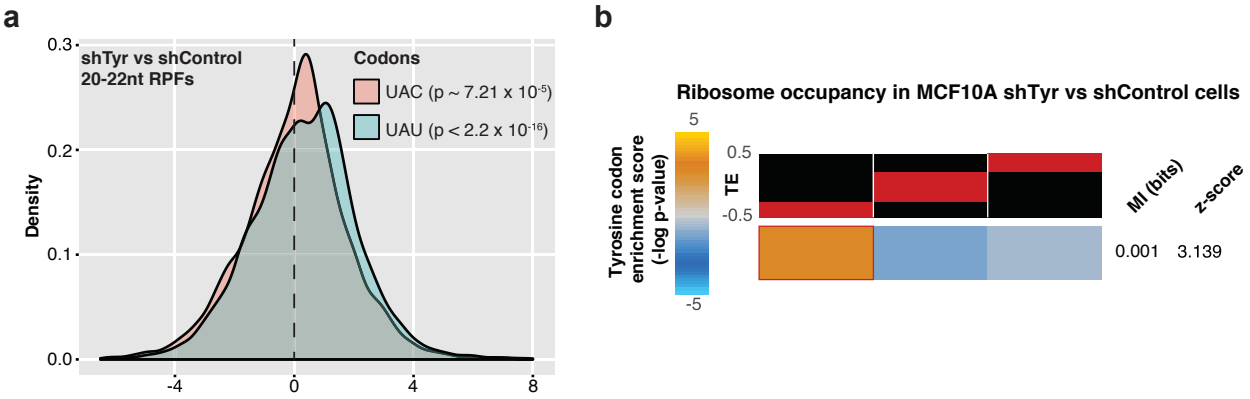

Figure 3.17. Global ribosome occupancy analysis from tRNA$^{Tyr}_{GUA}$-depleted cells reveals reduced translation efficiency for Tyr-enriched genes.
a, Ribosome occupancy of 20-22nt RPFs in tRNA$^{Tyr}_{GUA}$-depleted cells compared to control cells reveal greater occupancy at both tyrosine codons in tRNA$^{Tyr}_{GUA}$-depleted cells. **b**, Genes were sorted based on their changes in GC-corrected translation efficiency (TE) values, with reduced TE in tRNA$^{Tyr}_{GUA}$-depleted cells shown in left and enhanced TE shown on right. The red bars over each column depict the range of values in that bin. We then assessed the distribution of genes with high tyrosine codon content across these three bins using mutual information calculation and testing (see methods for details). For visualization, we used the hypergeometric distribution to assign p-values to the overlap between tyrosine-rich genes and each of the three bins. We then defined an enrichment score as –log of p-value, if there was a significant enrichment. If the overlap is significantly fewer than expected by chance, log of p-value is used instead (depletion). The resulting enrichment score is then shown as a heatmap with gold depicting positive enrichment.

3.7 Studies of tF-Tyr^{GUA} biogenesis and its interactors, RNA binding proteins hnRNPA1 and SSB.

As previously discussed, oxidative stress in MCF10A cells not only caused tRNA-Tyr^{GUA} depletion, but also generated of tRF-Tyr^{GUA} as early as 5 minutes post H_2O_2 treatment. The tRF remained elevated for up to eight hours, declining to baseline at 24 hours post exposure (Figure 3.18).

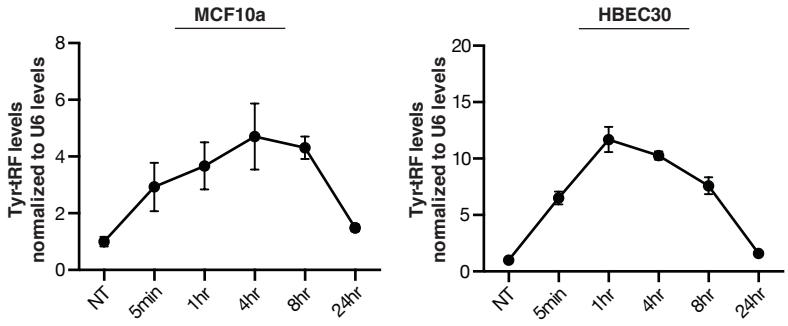

Figure 3.18. Time course of induction of tRF-Tyr^{GUA}.
Quantification of tRF-Tyr^{GUA} induction in response to oxidative stress as a function of time in MCF10A (left) (n=4) and in HBEC30 (right) (n=6).

Previous studies have implicated tRFs in multiple biological processes[88,91] Sequencing of the tRF-Tyr^{GUA} after gel extraction identified tRFs with a 5' leader sequence from nearly every tRNA-Tyr^{GUA} genomic locus (Figure 3.19a-b).

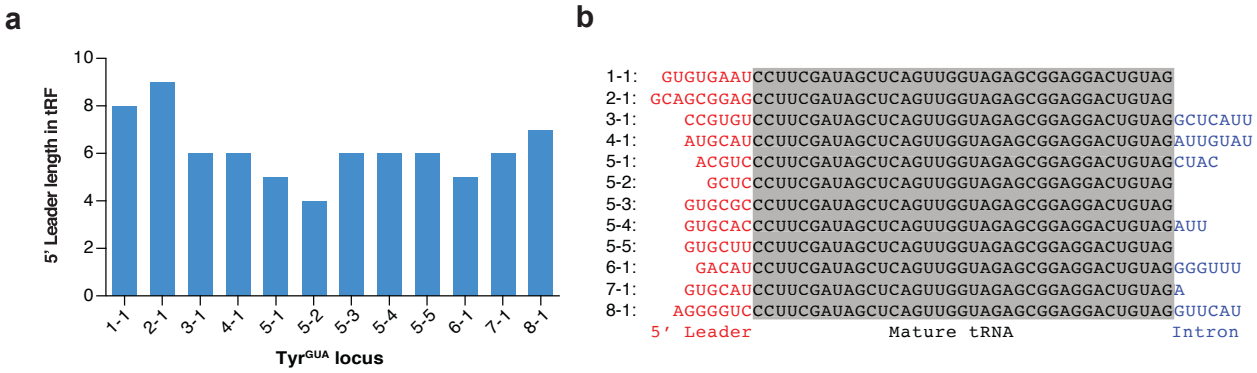

Figure 3.19. Sequencing of tRF-Tyr^{GUA} from identifiable loci.
a, Length of 5' leader sequence of all tRF-Tyr^{GUA} by loci that were identified by sequencing. **b**, Sequence of each tRF-Tyr^{GUA} by loci that were identified by sequencing. Conserved tRF-Tyr^{GUA} found in each loci are highlighted in gray.

We first wondered whether tRF-Tyr^{GUA} might impact the same molecular pathway as the mature tRNA. Using the conserved region from the different tRF-Tyr^{GUA} sequences (Figure 3.19b), we transfected a 37nt synthetic mimetic as a means of eliciting gain-of-function. tRF-Tyr^{GUA} transfection did not significantly alter protein levels of USP3, SCD, or EPCAM and did not impact

growth (Figure 3.20). These findings suggested that tRF-Tyr^{GUA} might play a regulatory role independent of the tRNA-Tyr^{GUA} -mediated response.

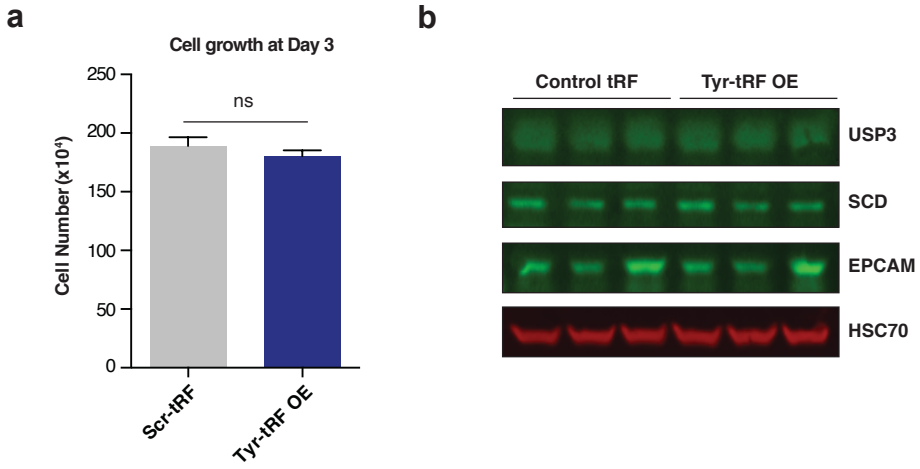

Figure 3.20. tRF$^{Tyr}_{GUA}$ does not affect growth nor Tyr-rich protein expression.
a, Cell growth of MCF10A cells transiently transfected with a tRF$^{Tyr}_{GUA}$ mimetic relative to a scrambled tRF control (n=3). A one-tailed Mann-Whitney test was used to test for significance at day 3. **b**, Western blot of downstream tRNA$^{Tyr}_{GUA}$-dependent genes 24 hours after transfection of tRF$^{Tyr}_{GUA}$ mimetic or a scrambled tRF control.

We next asked what factors could contribute to the cleavage of this tRF. Given that the tRF may originate from the pre-tRNA, we wondered whether the tRNA splicing machinery may play a role. We also hypothesized that ANG might play a role, as an RNase known to cleave tRNAs at the anticodon loop[85]. We used RNAi-mediated knockdown for ANG as well as TSEN2, the catalytic subunit of the tRNA splicing complex[116,117], and CLP1, a second tRNA splicing component[118]. tRF-Tyr^{GUA} formation was not impaired by depletion of any of these components, suggesting that none of these ribonucleases are involved in mediating this oxidative-stress induced response (Figure 3.21).

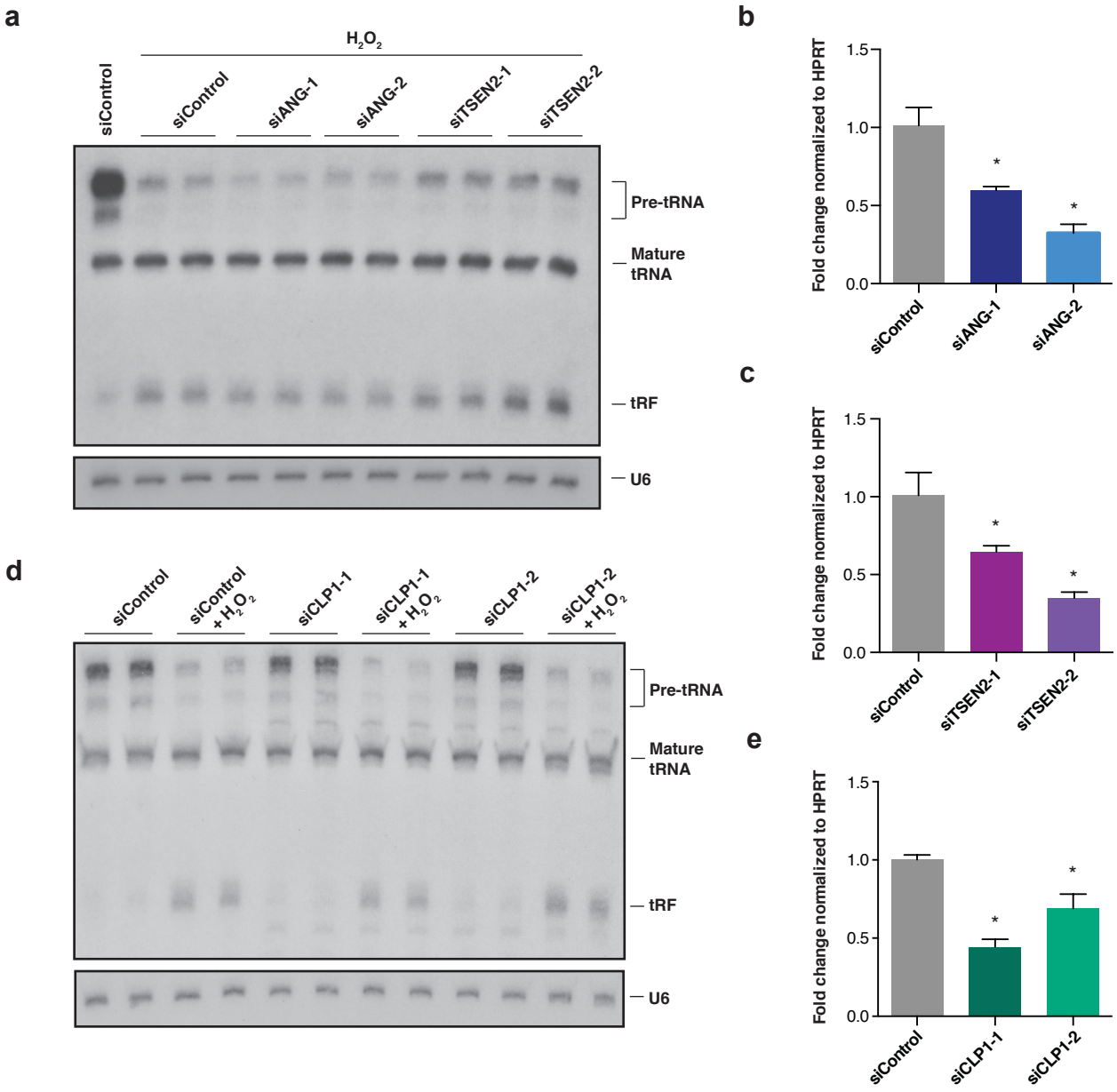

Figure 3.21. ANG, CLP1 and TSEN2 do not affect tRF-Tyr^{GUA} generation.
a, A northern blot depicting the tRF-Tyr^{GUA} induction in MCF10A cells with two independent siRNA each against angiogenin (ANG) or TSEN2 relative to a control siRNA. **b,** qRT-PCR validation of the siRNA-mediated knockdown of ANG relative to a control siRNA. **c**, qRT-PCR validation of the siRNA-mediated knockdown of TSEN2 relative to a control siRNA. **d**, A northern blot depicting the tRF-Tyr^{GUA} induction in MCF10A cells with two independent siRNA against CLP1 relative to a control siRNA. **e**, qRT-PCR validation of the siRNA-mediated knockdown of CLP1 relative to a control siRNA.

One mechanism by which tRFs have been proposed to function is through their interaction with various RNA binding proteins (RBPs)[88,119,120]. We hypothesized that tRF-Tyr^{GUA} may not only be a degradation product of tRNA fragmentation, but may also interact in *trans* with an RBP. To test this, we used a synthetic 5'-biotinylated tRF-Tyr^{GUA} as bait in an *in vitro* co-precipitation experiment. Proteins interacting with the mimetic from cellular lysate were identified by in-solution digestion and mass-spectrometry, and compared to proteins interacting with a scrambled mimetic. Mass spectrometry identified numerous proteins that were enriched in the tRF-Tyr^{GUA} co-precipitation relative to scrambled control oligonucleotide (Figure 3.22a). We selected the most significantly enriched proteins—hnRNPA0, hnRNPA1, and SSB—and validated their interaction with synthetic tRF-Tyr^{GUA} by western blot. Western blot analyses confirmed the mass spectrometry results, revealing increased interactions between these proteins and tRF-Tyr^{GUA} mimetic relative to scrambled control (Figure 3.22b). These results suggest that tRF-Tyr^{GUA} may interact with one or more RBPs.

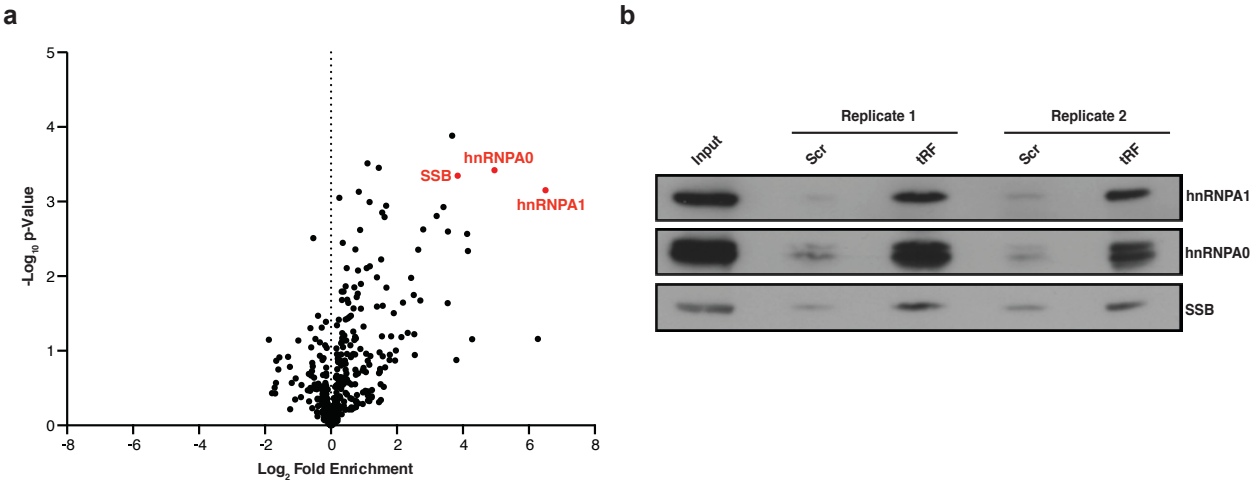

Figure 3.22. Characterization of tRF-Tyr^{GUA} and its potential functional role.
a, Volcano plot of mass spectrometry results from a synthetic 5'-biotinylated tRF-Tyr^{GUA} co-precipitation experiment with cell lysate. Log2 fold enrichment values of proteins identified from tRF-Tyr^{GUA} relative to scrambled tRF control samples. **b**, Western blot validation of mass spectrometry results for three of the top hits in (**a**), showing co-precipitation of endogenous proteins with transfected tRF-Tyr^{GUA} relative to a scrambled control sequence (Scr).

Next, we asked whether tRF-Tyr^{GUA} could interact endogenously with any RBP. UV-crosslinking enables assessment of direct endogenous interactions between RBPs and their cellular RNA substrates[121,122] and has been coupled with deep-sequencing methods such as HITS-CLIP or PAR-CLIP to identify all RNAs that interact with a given RBP[123,124]. The initial step of such CLIP-sequencing methods is a limited RNase digestion of immunoprecipitated ribonucleoprotein complexes, followed by SDS-PAGE visualization. Such experiments have previously been done with Argonaute-2, which binds microRNAs[125], and YBX1, which binds tRFs[88]. These experiments have revealed well-defined bands roughly the size of the RBP, which represent the RBP bound to a population of small RNAs. In contrast, for RBPs that bind mRNAs, CLIP-seq methods reveal a smear representing the RBP bound to a population of such longer RNAs[88,125] (Figure 3.23).

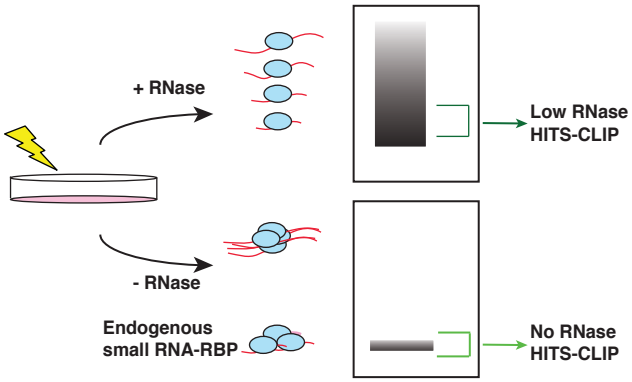

Figure 3.23. a modified HITS-CLIP sequencing approach to capture smRNA-associated RBPs.
a, Schematic depicting the expected visualization of a cross-linked immunoprecipitation by autoradiogram. Samples processed in the absence of RNase digestion that revealed a band corresponding to smRNA-RBP interactions were processed for HITS-CLIP. Samples processed using low RNase digestion showing a smear representing mRNA-RBP interactions by autoradiogram were also processed for HITS-CLIP.

To determine if any of the candidate RBPs identified by mass spectrometry interact with endogenous small RNA populations, we included an experimental condition where the HITS-CLIP protocol was conducted in the absence of RNase digestion to ensure that any potential small RNA-RBP bands visualized were not a consequence of, or confounded by, RNase digestion. UV-crosslinked immunoprecipitation followed by SDS-PAGE in the presence or absence of RNase digestion revealed that endogenous hnRNPA1 and SSB interacted with an endogenous small RNA population (Figure 3.24a-b).

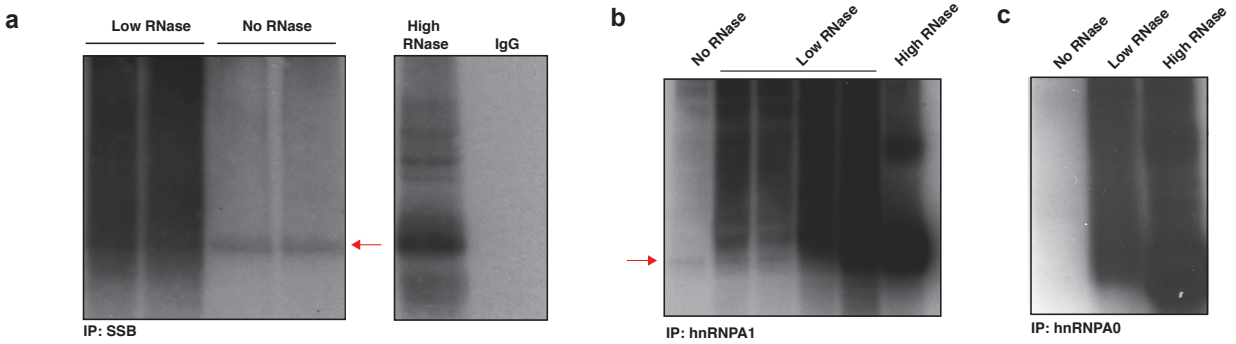

Figure 3.24. a modified HITS-CLIP sequencing approach to capture of tRF-Tyr^{GUA} and its potential functional role.
a, Volcano plot of mass spectrometry results from a synthetic 5'-biotinylated tRF-Tyr^{GUA} co-precipitation experiment with cell lysate. Log_2-fold enrichment values of proteins identified from tRF-Tyr^{GUA} relative to scrambled tRF control samples. **b**, Western blot validation of mass spectrometry results for three of the top hits in (**a**), showing co-precipitation of endogenous proteins with transfected tRF-Tyr^{GUA} relative to a scrambled control sequence (Scr).

We did not observe a small RNA-ribonucleoprotein band for hnRNPA0 in the absence of RNase (Figure 3.24c), even upon prolonged autoradiographic exposure, suggesting that this RBP either does not significantly interact with a small RNA population *in vivo* or this method is not conducive to identifying this interaction. These findings suggest that hnRNPA1 and SSB directly interact with small RNA populations *in vivo*.

Next, we sought to identify hnRNPA1 and SSB-bound small RNAs. An analysis of tRFs bound by a previously published CLIP-seq study for hnRNPA1[126] validated our observations by revealing a reciprocal interaction between hnRNPA1 and tRF^{Tyr}_{GUA} (Figure 3.25).

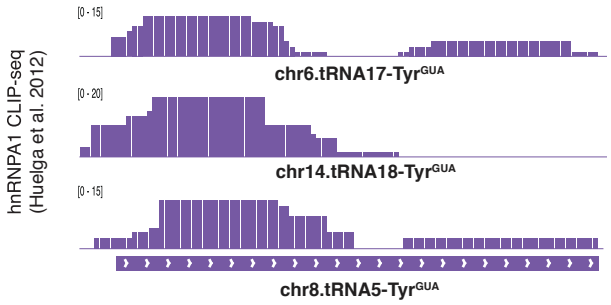

Figure 3.25. tRF-Tyr^{GUA} interacts with hnRNPA1 in an independent dataset.
IGV plots from the hnRNPA1 HITS-CLIP[126] reveals interactions with the tRF-Tyr^{GUA}.

As an abundant RBP, hnRNPA1 has many previously described roles in gene expression regulation, including as a regulator of splicing and mRNA stability via binding to 3' UTRs [127,128]. hnRNPA1 has also been implicated in promoting growth and multiple cancer progression phenotypes[129,130]. We next conducted HITS-CLIP for endogenous SSB with and without RNase digestion. SSB, also known as La, is a well characterized RNA-binding protein known to bind the nascent 3' ends of Pol III transcripts, including those of full-length pre-tRNAs[131–133]. Although our HITS-CLIP experiment was designed to enrich for signal from tRFs, we found that consistent with its previously described canonical role in binding Pol III transcripts, alignment and analysis of sequencing reads revealed binding of SSB to the 3'-trailers of pre-tRNAs (Figure 3.26a). Importantly, in addition to this previously described binding, we observed previously unreported interactions of SSB with the 5' half of tRNA-Tyr^{GUA} arising from multiple distinct loci (Figure 3.26b). In experiments with and without RNase, sequencing reads containing and not containing the 5' leader region of pre-tRNA-Tyr^{GUA} were detected. The 5' leader containing

reads likely represent intermediates in the pre-tRNA-Tyr^{GUA} processing reaction (Figure 3.26 b-c)[134].

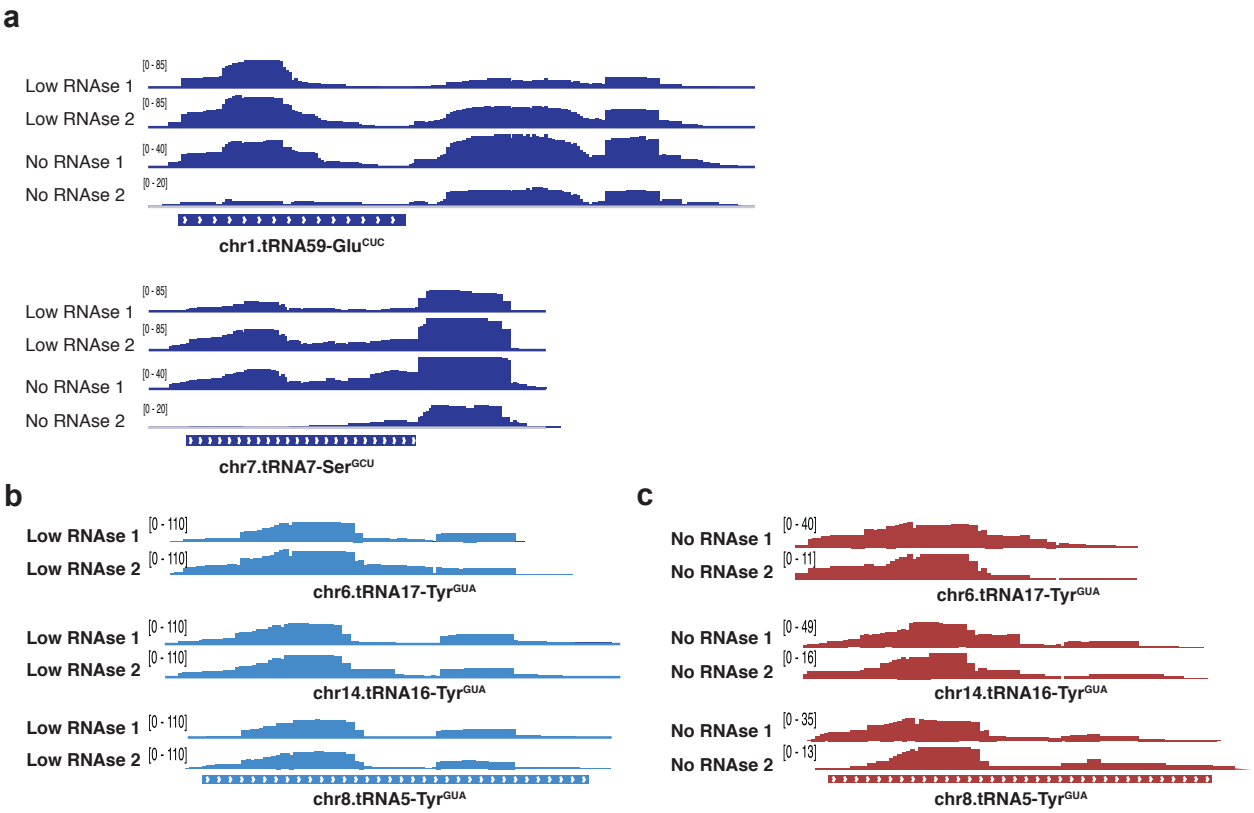

Figure 3.26. tRF-Tyr^{GUA} and pre-tRNA-Tyr^{GUA} interact with SSB.
a, IGV plots from the SSB HITS-CLIP reveals protein binding to the 3' trailer end of pre-tRNAs arising from distinct tRNA loci. **b**, IGV plots representing SSB interacting with the tRF-Tyr^{GUA} in samples that were treated with low levels of RNase digestion. SSB bound tRF-Tyr^{GUA} reads mapped to multiple loci encoding tRNA-Tyr^{GUA}. **c**, Similar to the IGV plots shown in (**b**), but depicting SSB interactions with tRF-Tyr^{GUA} loci in samples without RNase digestion.

The abundant number of reads mapping to the 5' regions of tRNA-Tyr^{GUA} distinguish these SSB-tRF interactions from the previously described canonical SSB interactions with 3'-trailers of full-length pre-tRNAs. This notion is further supported by our observations of SSB binding to the 5' tRF without 3'-trailer binding even in the absence of RNase digestion. These observations reveal that tRF-Tyr^{GUA} interacts in *trans* with RBPs in human cells.

We next investigated if the stress-induced tRF-Tyr^{GUA} might regulate the activity of hnRNPA1 or SSB as a *trans* factor. Using the 3' UTR targets of hnRNPA1 previously identified by CLIP-seq[126], we assessed whether tRF-Tyr^{GUA} impacts hnRNPA1-mediated mRNA stabilization. Following transfection of the tRF-Tyr^{GUA} mimetic or a scrambled control, we observed impaired stabilization of hnRNPA1 targets in an RBP-specific manner (Figure 3.27a). Conversely, locked nucleic acid mediated inhibition of tRF-Tyr^{GUA} or a control had the opposite effect in increasing stability of hnRNPA1 mRNA targets in an hnRNPA1 specific manner (Figure 3.27b). These results are consistent with known reports of hnRNPA1 binding to 3' UTRs to affect mRNA stability[127,128]. Taken together, our results are consistent with tRF-Tyr^{GUA} competing with hnRNPA1 target transcripts for binding to endogenous hnRNPA1. tRF-Tyr^{GUA}-dependent reduction of hnRNPA1 binding to its 3'UTR targets decreased stability of hnRNPA1 transcripts during a-amanitin-stability analyses.

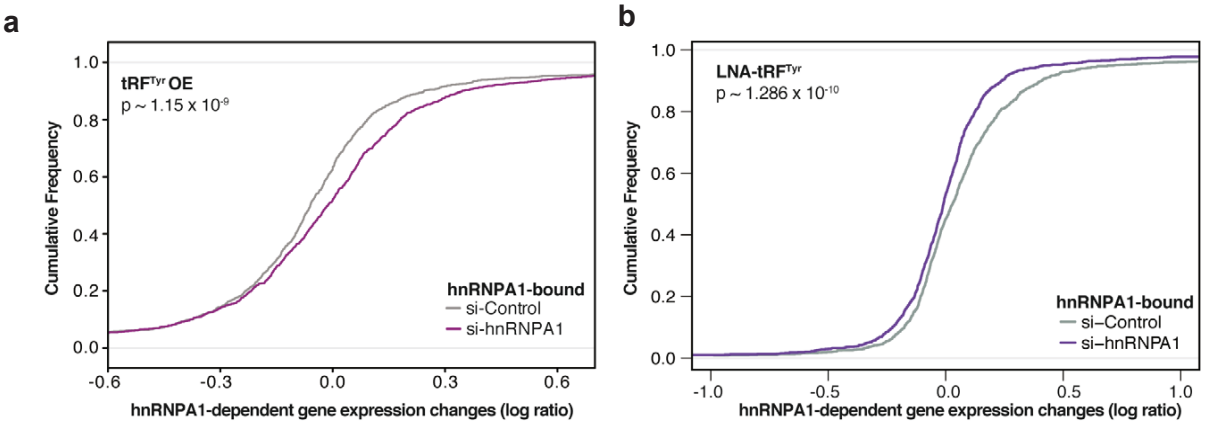

Figure 3.27. tRF-Tyr^{GUA} interacts with hnRNPA1 in an independent dataset.
a, cumulative distribution in control and hnRNPA1 depleted cells of the stability levels for mRNA transcripts with 30 UTR hnRNPA1 CLIP binding[126]. Transfection of tRF-Tyr^{GUA} led to a significant right-shift in the expression levels of 30 UTR bound hnRNPA1 transcripts. Statistical significance was measured using the Kolmogorov–Smirnov test. **b**, Cumulative distribution as in (a). Transfection of locked nucleic acid against tRF-Tyr^{GUA} and treatment with 200 μM H_2O_2 led to a significant left-shift in mRNA stability of 3'UTR-bound hnRNPA1 transcripts. Statistical significance was assessed using the Kolmogorov–Smirnov test.

Transfection of the tRF-Tyr^{GUA} mimetic did not impact expression of Pol III transcriptional targets, suggesting that the canonical nuclear role for SSB was unaffected by increased levels of the tRF-Tyr^{GUA} mimetic in this context (Figure 3.28).

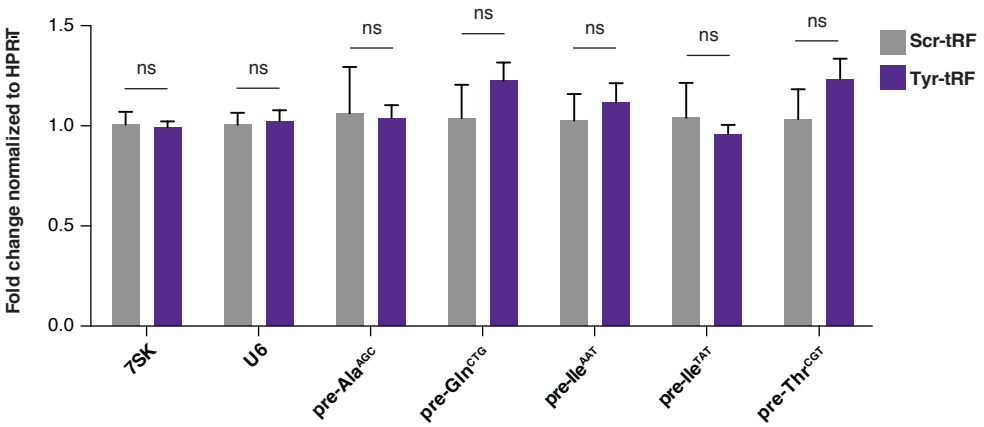

Figure 3.28. tRF-Tyr^{GUA} mimetic expression does not affect SSB canonical function. Quantitative RT-PCR expression levels for various Pol III transcribed targets from MCF10A cells transfected with the tRF-Tyr^{GUA} mimetic or a scrambled control.

Our findings describe that stress-induced fragmentation can cause a specific tRNA to become depleted, resulting in translational consequences. This process concomitantly gives rise to a tRNA fragment that can interact in *trans* and functionally impact the regulon of an RNA-binding protein known to promote growth and cancer progression phenotypes (Figure 3.29).

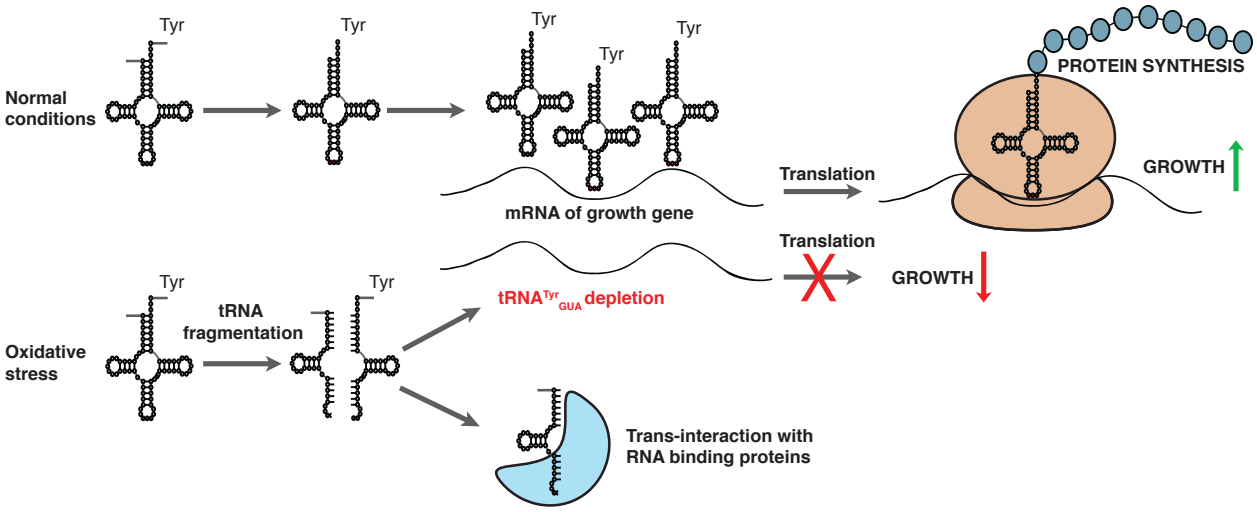

Figure 3.29. Model of tRNA-Tyr^{GUA} -dependent gene regulatory response to oxidative stress.

3.8 tRNA-Tyr^{GUA} fragment generation is DIS3L2 exoribonuclease dependent

Finally, we employed unbiased approaches to identify a ribonuclease involved in oxidative-stress induced tRF-Tyr^{GUA} generation. In an ongoing RNAi screen focused on identifying putative regulators of tRNA fragments in *C.elegans*, we observed that depletion of the exoribonuclease *disl2*—the ortholog of *DIS3L2*—an tumor suppressor in Wilms tumor, impaired stress-induced tRNA fragment levels (unpublished results, data not shown).

In parallel, we conducted an RNAi screen of all known human ribonucleases in mammalian cells. In this screen, we systematically depleted each ribonuclease candidate with a pool of siRNA oligonucleotides, then treated the samples with H_2O_2 and assessed EPCAM mRNA levels as a readout. We reasoned that, since tRNA-Tyr^{GUA} depletion occurred concomitantly with tRF-Tyr^{GUA} induction, H_2O_2-induced EPCAM mRNA depletion might be rescued relative to control by depletion of a ribonuclease responsible for tRF generation. Indeed, RNAi depletion of several candidate ribonucleases produced a relative EPCAM mRNA enrichment, which we validated in a secondary validation screen containing only top hits (Figure 3.30). Consistent with our findings in *C.elegans*, DIS3L2 produced the most substantial effects on EPCAM expression, in both the

primary and secondary validation screens, highlighting its importance as a candidate for further study.

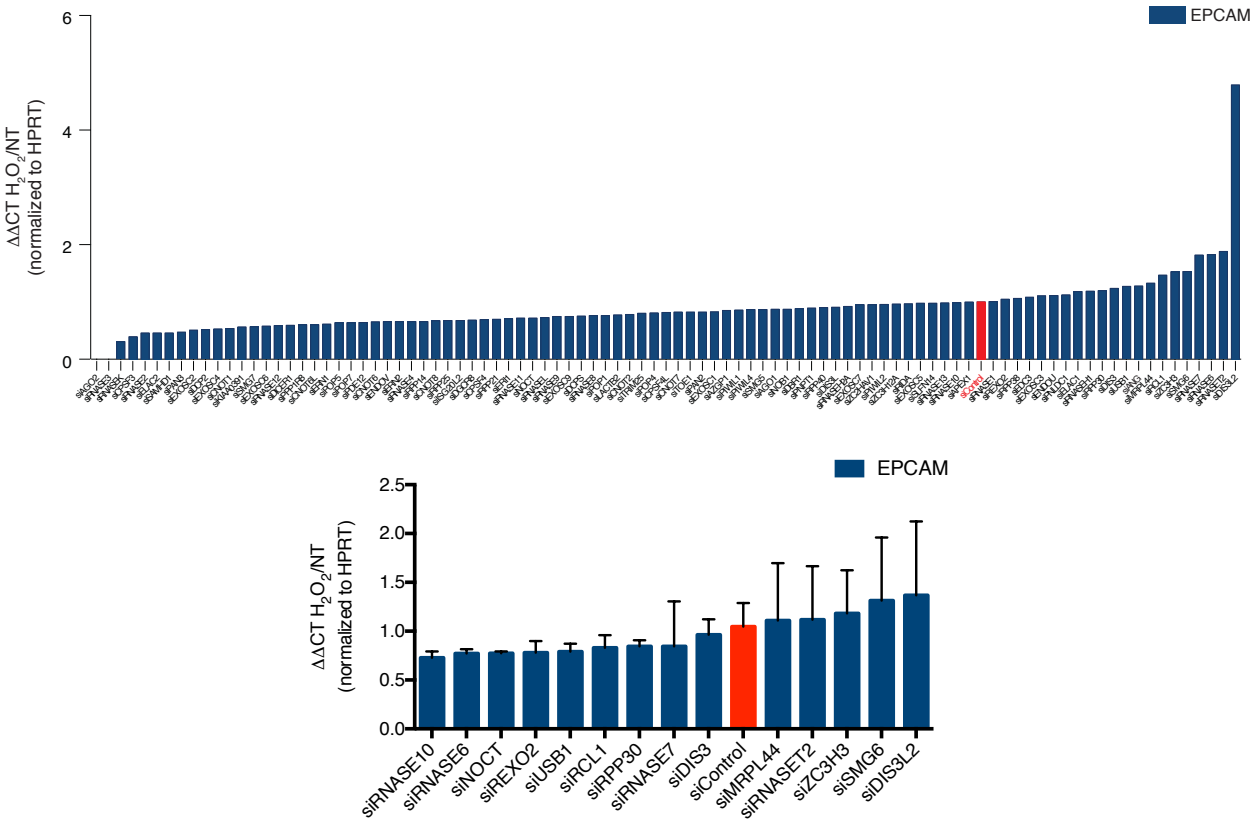

Figure 3.30. An RNAi screen of human ribonucleases identifies DIS3L2.
upper, siRNA screen of known human ribonucleases. siControl sample indicated in red (n=2). **lower,** secondary validation siRNA screen of top hits from upper panel. In both screens, RNAi-depleted cells were treated with H_2O_2 and EPCAM mRNA expression levels were measured as a readout of the relevance of gene knockdown to tRF-Tyr^{GUA} induction and concomitant tRNA-Tyr^{GUA} depletion. A positive value for EPCAM ratio (treated / control) suggests a relevant candidate.

To validate mammalian and *C.elegans* screen findings, we first employed RNAi approaches to deplete *disl2* in worms. RNAi-depletion was sufficient to reduce *disl2* expression by 50% (Figure 3.31a). Consistent with screen results, following 15 minutes exposure to H_2O_2, *disl2*-depleted worms produced less stress-induced tRNA-Tyr^{GUA} fragments relative to control animals (Figure 3.31b-c).

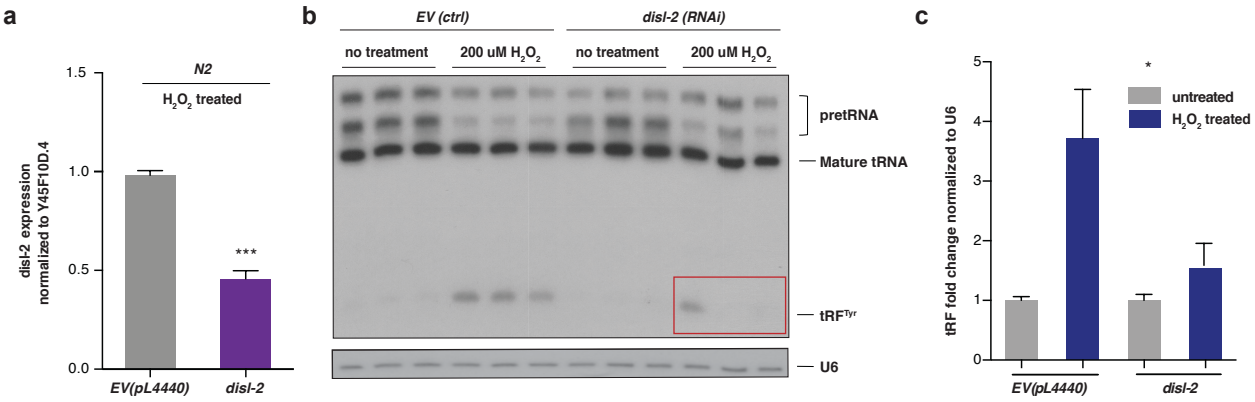

Figure 3.31. tRF-Tyr^{GUA} induction is blunted by RNAi-mediated *disl2* depletion in *C.elegans*.
a, mRNA expression levels for disl2 after RNAi treatment, as measured by qRT-PCR (n=3). A one-tailed Mann-Whitney test was used to test for statistical significance between control and knockdown gene expression values. **b**, A northern blot for tRNA-Tyr^{GUA} in wild type *N2* empty vector control and RNAi-mediated *disl-2* knockdown *C.elegans* strains after 15 minutes of oxidative stress (200µM H_2O_2). As before, a single probe complementary to *C.elegans* pre-tRNA-Tyr^{GUA}, mature tRNA-Tyr^{GUA}, and tRNA-Tyr^{GUA} was ^{32}P-labeled and used for detection. **c**, quantification of (**b**).

A similar effect was observed in worms harboring constitutive *disl2* mutation (*syb1033*) upon oxidative stress exposure. As with RNAi experiments, *disl2* depleted animals selectively impaired tRNA-Tyr^{GUA} formation in the context of oxidative stress treatment (Figure 3.32).

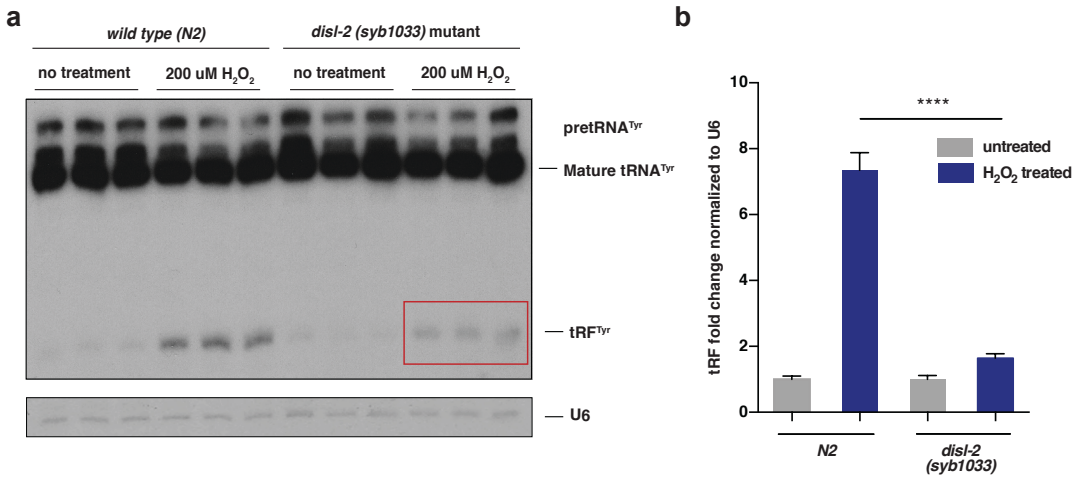

Figure 3.32. tRF-Tyr^{GUA} induction is blunted by RNAi-mediated *disl2* depletion in *C.elegans*.
a, A northern blot for tRF$^{Tyr}_{GUA}$ in wild type *N2* and homozygous *disl-2 (syb1033)* mutant *C.elegans* strains after 15 minutes of oxidative stress (200μM H_2O_2). A single probe complementary to *C.elegans* pre-tRNA$^{Tyr}_{GUA}$, mature tRNA$^{Tyr}_{GUA}$, and tRF$^{Tyr}_{GUA}$ was ^{32}P-labeled and used for detection. **b**, quantification of (**a**). Data are mean ± s.e.m. *p<0.05, **p<0.01, ***p<0.001.

To assess this in human cell lines, we utilized a 293T cell line depleted of DIS3L2 using TALENs, as well as a DIS3L2 knoockdown cell line by CRISPRi. Depletion of DIS3L2 also impaired oxidative stress-induced tRNA-Tyr^{GUA} fragment levels in two independent human cell lines (Figure 3.33a-d). DIS3L2 depletion selectively impaired tRF-Tyr^{GUA} formation upon oxidative stress, and did not cause pre-tRNA-Tyr^{GUA} accumulation—consistent with DIS3L2 mediating processing/maturation of a tRF-Tyr^{GUA} precursor rather than the pre-tRNA-Tyr^{GUA} cleavage. These findings implicate the DIS3L2 tumor suppressor in tRF-Tyr^{GUA} generation.

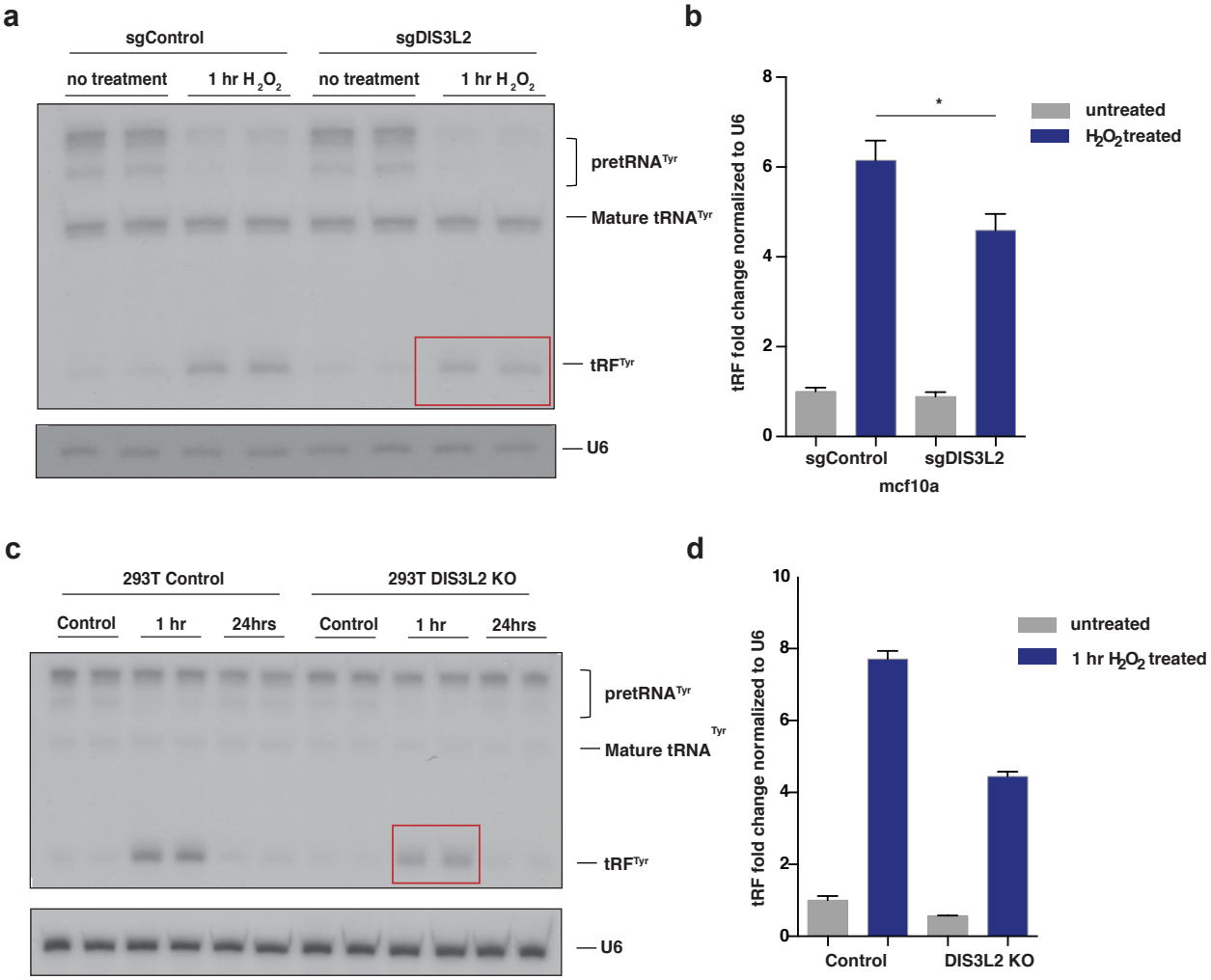

Figure 3.33. tRF$^{Tyr}_{GUA}$ induction is blunted by DIS3L2 depletion in human cell lines.
a, A northern blot for tRF$^{Tyr}_{GUA}$ in CRISPRi-mediated DIS3L2 knockdown mcf10a cells after 1 hour of oxidative stress. **b**, quantification of (**a**). n=7 across three independent experiments (normalized to U6 levels). A one-tailed Mann-Whitney test was used to test for statistical significance. **c**, A northern blot for tRF$^{Tyr}_{GUA}$ in DIS3L2 knockout HEK293T cells after 1 hour and 24 hours oxidative stress. **d**, quantification of tRNA$^{Tyr}_{GUA}$ in (**c**) after 1 hour of oxidative stress. (n=1, two replicates, normalized to U6 levels.) As before, a single probe complementary to pre-tRNA$^{Tyr}_{GUA}$, mature tRNA$^{Tyr}_{GUA}$, and tRF$^{Tyr}_{GUA}$ was ^{32}P-labeled and used for detection. Data represent mean ± s.e.m. *p < 0.05, **p < 0.01, and ***p < 0.001

3.9 Summary

We here identify and characterize an oxidative stress-mediated tRNA-Tyr^{GUA} depletion response.

Oxidative stress simultaneously depletes mature tRNA-Tyr^{GUA} to repress cell growth through

tyrosine-specific translation changes, and results in DIS3L2-dependent tRNA fragmentation to

produce tRF-Tyr^{GUA}, which acts in *trans* with two well-studied RBPs, hnRNPA1 and SSB, known to play roles in cell growth and tumor progression. These findings provide insight into the dynamic landscape of noncanonical roles of tRNAs and their associated factors in modulating translation and responses to cell stress.

CHAPTER 4. Discussion and Perspectives

4.1 Characterization of a tumor-suppressive tRNA synthetase: Implications and Perspectives

In Chapter 2, we identify LARS, a specific tRNA synthetase, as a breast cancer tumour suppressor. We show that repression of LARS reduces the charging and function of tRNA-Leu^{CAG} to suppress malignant transformation. Depletion of LARS reduced leucine rich protein translation and expression, including that of two candidate genes, EMP3 and GGT5, that we further implicated in tumour suppression and proliferation. These findings suggest that LARS regulates a tumour suppressive network. Moreover, they demonstrate that specific repression of a tRNA synthetase can modulate translation of tumour suppressors enriched in a cognate codon.

We demonstrate that LARS downregulation promotes mammary tumour formation. These findings are surprising; translational upregulation is classically thought to be a growth-promoting process, as activation of multiple oncogenes including MYC, AKT and PI3K drives transcription of ribosomal RNA and ribosomal protein genes[26,40]. Furthermore, translational upregulation by MYC has been found to be pro-oncogenic through translational upregulation of specific genes[135]. As such, in the context of global translation upregulation, specific mechanisms are needed to prevent translational enhancement of tumour suppressors. We propose that LARS serves such a purpose, given that specific tumour suppressive genes are enriched in leucine codons that are

decoded by cognate tRNAs sensitive to LARS expression. It has previously demonstrated that nutrient stress and amino acid availability can impact tRNA charging and translation[40–42,82], and specific tRNA synthetases have been implicated in promoting oncogenesis[54]. Our findings provide novel evidence in mammalian cells of tRNA synthetase-mediated suppression of translation in a cognate codon-dependent manner serving a tumour suppressive function in mammary cells.

We noted a reduction in not only charged, but also total tRNA-Leu isoacceptors by charged tRNA profiling in the context of reduced LARS expression. This finding is consistent with literature demonstrating that uncharged tRNAs are less stable than their charged counterparts, leading to tRNA degradation[99]. Therefore, LARS contributes to both reduced charging and subsequent destabilization of tRNA species. We also observe the most substantial reduction in more common tRNA-Leu species. Whether or not more common or more rare isoacceptors are affected first is thought to be dependent on cell type and state; however, these findings for leucyl-tRNA charging are consistent with previous reports that examined the role of amino acid depletion on tRNA charging, where the authors find that more common tRNA-Leu^{CAG}, tRNA-Leu^{AAG} and tRNA-Leu^{TAG} to be the first tRNAs affected in nutrient deprivation[42,82]. These findings reveal that tRNA synthetase depletion and amino acid limitation, though both rate limiting, may not affect mature tRNA populations in the same way and are instead cell type and cell state dependent. Indeed, the role of tRNA synthetases in regulating charged tRNA pools has been recently attributed to reduced ability of tRNA synthetases to bind and sequester uncharged tRNAs[136]. In sum, further research is warranted especially in the context of *in vivo* models to

examine the regulatory effects of tRNA synthetases on tRNA abundance and the maintenance of charged tRNA pools.

One important aspect of LARS-mediated tumor suppression that remains relatively unexplored is the corresponding dynamics of leucine amino acid pools. Leucine is an essential amino acid, therefore cells rely exclusively on uptake for maintenance of cellular pools. Its main cellular metabolic function is in ketogenesis, through breakdown by branched-chain keto-acid dehydrogenase (BCKD)[137]. Our *in vivo* tumor metabolite profiling of the branched chain amino acids in LARS knockdown tumors demonstrated no change in intratumoral concentrations of leucine, isoleucine or valine (Figure 2.14). A possible explanation for this is that intracellular leucine reservoirs are large relative to the amount of leucine used in maintaining charged tRNA populations, so LARS depletion fails to meaningfully impact overall pools. It is also possible that intracellular concentrations are maintained by increased export or reduced uptake in LARS depletion, to avoid excessive accumulation or depletion of free leucine. These possibilities could be explored by more in-depth metabolite profiling, for example of cellular import and export fluxes, TCA cycle uptake rates and usage by carbon tracing experiments.

We also consider the cellular rationale behind usage of leucine-rich protein translation to enact a tumor-suppressive program. Leucine is the most incorporated amino acid into the proteome and accounts for 10% of overall protein translation[63,64]; this could provide an unique opportunity for a potential regulatory handle that would impact many proteins, most of which contain some level of leucine codons for function. As a branched chain amino acid, leucine is structurally similar to isoleucine and valine as all contain small hydrophobic side chains. This structural overlap may

produce some functional redundancy, allowing for a unique role for leucine in regulating protein synthesis in relatively leu-rich or leu-poor proteins. An analysis of functional enrichment in leucine-rich proteins compared to isoleucine or valine-rich proteins could be elucidating in this realm, to assess the potential differential functional enrichment for proteins between these similar amino acids.

Another unique feature of leucine translation that could provide insight is the usage of six unique codons to incorporate it within the translatome, which are decoded by 5 distinct tRNA species. This level of redundancy is relatively unique; only arginine and serine also have 6 unique codons, and Ser codons are decoded by only four unique tRNA isoacceptors. It has been well-documented that translation efficiency and speed are slowed by rarer codon usage, or reduced tRNA abundance[68,114]. Thus, tRNA isoacceptor redundancy and multiple codon usage of leucine in particular may allow for more nuanced coordinated control of translation when incorporating Leu amino acids into proteins and may provide a distinctive regulatory handle that allows for leucine incorporation into proteins.

One mechanistic question worth exploring relates to how a specific tRNA synthetase affects tRNA charging differentially between isoacceptors. One potential explanation lies in aaRS recognition of the tRNA backbone, where structural and modification differences across different species may affect aaRS affinity. Interestingly, an exploration of sequence similarities across tRNA-Leu species highlights two distinct structural classes, with tRNA-Leu^{CAG}, tRNA-Leu^{AAG} and tRNA-Leu^{TAG} having the greatest sequence overlap, with tRNA-Leu^{CAA} and tRNA-Leu^{TAA} as more distinct species (Figure 4.1).

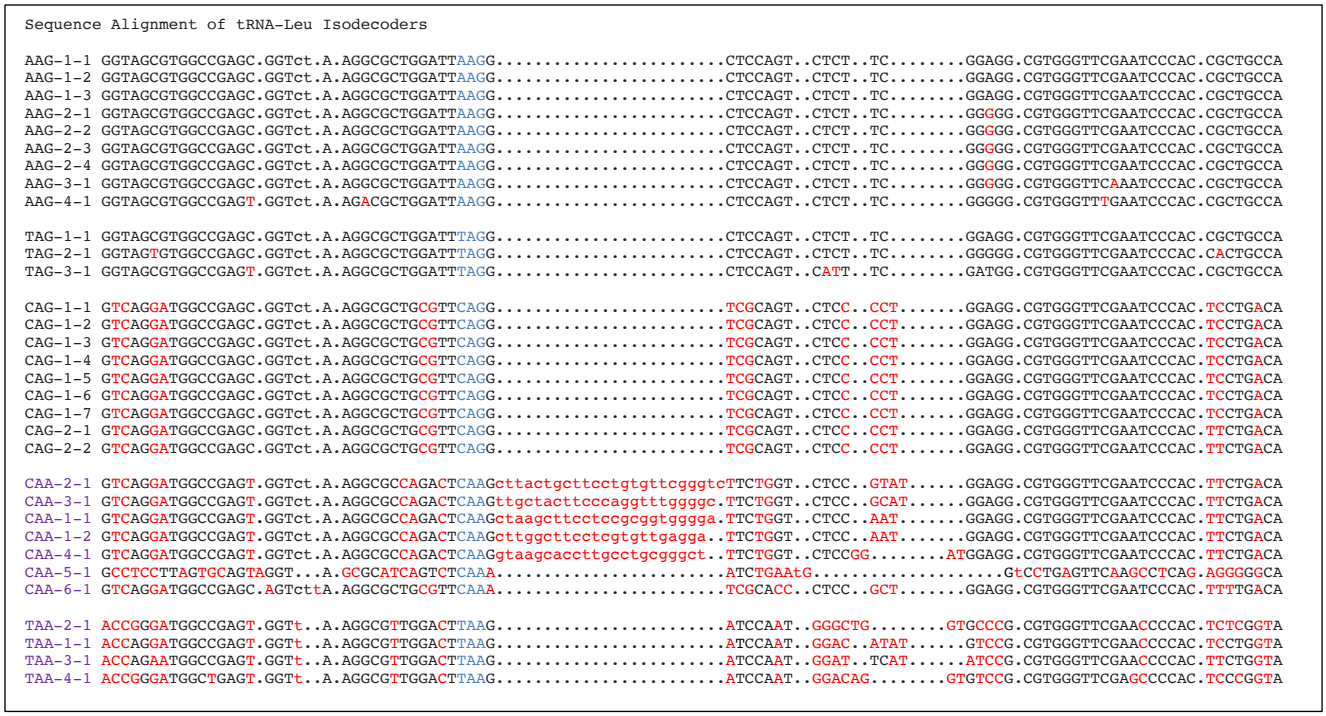

Figure 4.1. tRNA-Leu isoacceptor sequence overlaps form two distinct subtypes.

Leucine has been implicated specifically as a regulator of GCN2 kinase, a specific sensor of uncharged tRNAs that are generated through global amino acid starvation. In this mechanism, uncharged tRNAs bind to GCN2 and activate it[138]; GCN2, along with leucine specifically, can suppress translation and regulate mTORC1 activity[139–141]. These findings are intriguing in the context of our work, where we find LARS reduced leucyl-tRNA charging. However, for a number of reasons we believe our findings drive a unique gene expression program, rather than contributing to global translation changes. Most importantly, we see minimal effects on global translation. We demonstrate through polysome profiling in LARS-depleted 4T07 cells that polysome traces between these groups are not significantly different in terms of monosome and polyribosome association of transcripts (Figure 2.17). An *in vivo* experiment measuring o-propargyl-puromycin incorporation might be an interesting complementary study to elucidate potential changes in global translation, or lack thereof. Moreover, we do not observe changes in

intratumoral leucine pools, which may explain the lack of global translation repression by our proposed mechanism.

There is a growing body of work that documents a noncanonical role for LARS as an intracellular leucine sensor that directly regulates mTOR signaling upon leucine deprivation[52]. This pro-tumor role has led to speculation that LARS may act as an oncogene in some contexts, which has been probed in lung cancer[59]. These findings are in contrast to our breast cancer results, where LARS is a tumor suppressor. Several possible explanations exist. The first is, it may be that the tumoral contexts of our work already have hyperactivated mTOR signaling, rendering a further activation of mTOR by LARS comparatively ineffective in furthering growth. It is also possible that our systems harbor loss of function of TSC2, a tumor suppressor gene responsible for attenuating mTOR activity and growth promotion[142], making mTOR signaling ineffective as a regulatory checkpoint in these particular cancer contexts. Both of these possibilities are likely, given the lack of changes in endogenous S6 and S6K phosphorylation in our contexts (Figure 2.15). Consistently, we see attenuation of tumor growth when specifically inhibiting the mTOR-associated function of LARS without impairing catalytic activity, which may imply this enzyme is pleiotropic and multifunctional even in cancer (Figure 2.16). Therefore, it is important to consider the potential oncogenic role of LARS in certain cancer contexts as well.

Interestingly, we noted a number of upregulated oncogenes in the TMT-proteomics data in LARS-depleted tumors compared to control tumors, including Erbb2, Rab17a and Rell1. These data are encouraging in identifying LARS as a tumor suppressor, whose depletion may relieve

repression of oncogenic expression to further drive transformation. However, while the tumor suppressive proteins downregulated in LARS depletion were relatively Leu-enriched, these upregulated oncogenes were not correspondingly Leu-depleted. This may suggest alternative tumor suppressive mechanisms downstream of LARS, warranting further study.

While we have identified specific proteins as downstream mediators of LARS-dependent translational regulation of tumourigenesis, we uncovered a larger set of LARS-dependent translationally regulated genes that may govern additional phenotypes and processes. Future studies are needed to explore these additional pathways that may uncover unanticipated roles for LARS-mediated translation regulation in metabolic and homeostatic regulation. More broadly, our findings motivate systematic studies across tRNA synthetases as dynamic translational regulators of gene networks subserving various biological processes in health and disease.

4.2 Ribonuclease-dependent tRF generation: implications and perspectives

We identify DIS3L2, a human exoribonuclease, to be important in generation of tRF-Tyr^{GUA}. These findings are relatively surprising: DIS3L2 is thought to specifically interact with and cleave oligo- or polyuridylated RNAs[143], but has not previously been demonstrated to cleave tRNAs. DIS3L2 has been implicated in degradation of uridylated let-7 – a tumor-suppressive microRNA – in Wilms tumor, and is mutated in the overgrowth disorder Perlman syndrome[144,145]. Interestingly, DIS3L2 depletion in both mammalian cells and *C.elegans* only partially abrogated H_2O_2-mediated tRF-Tyr^{GUA} generation. This may suggest cooperative cleavage mechanisms or dependence on multiple ribonucleases in concert. This is particularly notable as, despite abrogation of tRF induction in DIS3L2 depleted cells, there is sustained reduction in pre-tRNA-Tyr^{GUA} levels comparable to control conditions (Figure 3.33). This reduction in pre-tRNA may

suggest cleavage by an alternative mechanism, with DIS3L2 serving to stabilize the tRF. In this mechanism, reduced DIS3L2 reduces the stability of the tRF and increases turnover, resulting in an overall reduction of tRF pools. Though further studies are needed to fully characterize the mechanism of tRNA-Tyr^{GUA} cleavage, the implication of DIS3L2 as a regulator of this process highlights the importance of tRF-Tyr^{GUA} generation as a tightly coordinated process.

4.3 Summary and Perspectives: tRNA modulation of translation in cellular physiology and disease

In this thesis, we describe two complementary stories of translation regulation through expression and availability of two tRNAs and their associated factors; a tRNA synthetase (LARS) and a tRNA fragment (tRF-Tyr^{GUA}). In both cases, tRNA depletion serves to reduce candidate proteins that are relatively enriched in the cognate codon, though for different tRNAs and amino acids. Both of these examples illustrate the power of translation control in altering gene expression programs, in the context of malignancy or other cellular stress. Our findings help to further characterize the broader principles of post-transcriptional gene regulation and their potential in mitigating downstream disease phenotypes.

One intriguing avenue for future study would be to establish a more generalizable pipeline for detection of amino acid or codon-specific translation differences in different cell types and states. We here implicate leucine-rich protein translation in regulating a tumor suppressive network in breast cancer, and tyrosine-rich protein translation in reducing growth-related translation under cellular stress. To identify other cellular states that may be in part regulated by codon-specific translation, a general pathway analysis within different cell types could be conducted and correlated to relative codon enrichment within all genes. Relative expression of tRNAs and

tRNA associated factors could also be correlated to this information. A pipeline could be constructed to pool genomic data, mRNA and tRNA expression data between different cell types to identify putative amino acid and codon-specific changes that may drive cellular expression programs and identify further candidates regulated by translation in this manner.

Studies of this kind are also essential in offering insights into novel therapeutic targets. Though tRNAs themselves are essential for normal physiology, the associated factors described here are more targetable and may have less deleterious side effects from a therapeutic perspective. Future studies could capitalize on this approach; for example, while we describe a tumor suppressive program regulated by LARS and select leucyl-tRNAs, other tRNA synthetases exist that exert oncogenic roles in certain tumor subtypes. It would be intriguing to target translation through suppression or pharmacological modulation of these oncogenic drivers. In the case of therapeutic approaches to tumor suppressor genes, while re-expression of tRNAs may not alleviate downregulation of LARS as a loss of tumor suppressive effects, it may be intriguing to explore a rescue with a similar tRNA synthetase, IARS or VARS. Isoleucine and valine are structurally and chemically similar to leucine, and while tRNA synthetases are thought to be highly specific for the tRNAs and amino acids they bind, compensatory or complementary mutations in critical binding pockets could be explored to generate or alter an existing tRNA synthetase that could rescue LARS downregulation in transformation. In sum, this exciting avenue offers a myriad of possibilities for future study, to highlight and target novel pathways and processes and mitigate their role in human health and disease.

CHAPTER 5. Materials and Methods

5.1 Cell Culture

MCF10A cells were cultured in DMEM/F12 media supplemented with 5% horse serum and final concentrations of 20 ng/ml of EGF, 0.5 μg/ml of hydrocortisone, 100 ng/ml of cholera toxin, and 10 μg/ml of insulin.

EO771, HCC1806 and LM2C cells were cultured in RPMI media supplemented with 10% FBS, 1mM glucose, 10 mM HEPES and 1 mM sodium pyruvate. 293T, MDA-MB-231, T47D, NMuMG 4T07, 4T1 and 67NR cells were cultured in DMEM media supplemented with 10% FBS.

HBEC30 cells were cultured in keratinocyte- SFM media with the included supplements of BPE and EGF. All human cell lines were STR tested and all lines were routinely tested for mycoplasma contamination.

Oxidative stress was induced with 200 μM H2O2 or 50 μM of menadione (Sigma) dissolved in DMSO. RNA was then isolated by TRIzol and isopropanol precipitation as described below.

5.2 Generation of stable cell lines

Lentivirus was produced in 293T cells grown in 10 cm plates. Cells were transfected with either two-vector or three-vector lentivirus production plasmids. For two-vector lentiviral production, 1.7 μg and 2.6 μg of packaging plasmids pMD2.g and psPAX2 respectively, 3.4 μg of pLKO.puro1 vector containing the appropriate shRNA, using 40 μL Lipofectamine 2000 (Invitrogen). For three-vector lentiviral production, 3 μg of each packaging vector (pRSV-Rev, pCMV-VSVG-G, and pCgpV) were transfected with 9 μg of the appropriate hairpin in a pLKO-backbone vector using 30 μl of Lipofectamine 2000 (Invitrogen). After 24 hours, the media was replaced with fresh media and virus-containing supernatant was harvested 48 and 72 hours after

transfection. The supernatant was filtered through a 0.45 μm filter before 1-2 mL of virus was used with 8ug/mL polybrene to transduce pre-plated 4T07, MCF10A or NMuMG cells at 75% confluence. Following 24 hours of transduction, selection was conducted using 4 μg/mL puromycin (4T07) or 1μg/mL puromycin (MCF10A, NMuMG). mRNA and protein knockdown were validated by qPCR and western blot, respectively.

5.3 Generation of CRISPRi cell lines

A non-targeting control sgRNA and 4-5 target specific sgRNAs targeting DIS3L2 (generated using the ChopChop tool[146]) or tRNAs (generated from all PAM sequences within 200bp of tRNA transcription start site that were unique among isoacceptors) were cloned into lentiGuide-Puro (Addgene #52963). The individual sgRNAs were subsequently transduced into MCF10A cells stably expressing pHR-SFFV-dCas9- BFP-KRAB (Addgene #46911), and the cells expressing the sgRNAs were enriched for using 1 or 1.2ug/ml puromycin selection. Cells with the strongest knockdown of DIS3L2 (>90%) by Western blot or of tRNA by Northern blot were subsequently used for experiments, with the following guide sequences: sgRNA- DIS3L2-A: CGCGGCGTTCTAGAGAGCGA, sgRNA- LeuCAG-1: ACGCAGCGCCTTAGACCGCT, sgRNA- LeuCAG-2: CAGGATGGCCGAGCGGTCTA.

5.4 PyMT transformation

Mammary epithelial cell lines were seeded to 70% confluence and transduced the following day with lentivirus expressing pH3-PyMT as described above. After 24 hours of transduction, blasticidin selection was performed for 3 days and cells were treated with 10 μM pifithrin-α (Sigma) for 5 days.

5.5 Colony formation assays

600 cells were plated in 24-well plates, (or 3,000 cells in 6-well plates), in 0.6% Noble agar in standard tissue culture media, atop an underlay of 1% Noble ager and 2X cell culture media. Cells were cultured at 37ºC for 18 days and colonies were stained with 0.005% crystal violet and visualized on ChemiDoc Chemiluminescence reader. Colonies formed per 600 cells were counted manually.

5.6 Transient tRNA-Tyr^{GUA} overexpression

Overexpression constructs for tRNATyr^{GUA} were made as follows: 3 copies of tRNATyr^{GUA}, per plasmid, were synthesized (Genewiz) into the pUC57-KAN vector. Each copy had 150nt upstream and 90nt downstream genome sequences included but did not include the intron sequence. This vector or an empty pUC57-KAN vector were transiently transfected using Lipofectamine 3000 (Invitrogen).

5.7 Using tRF-Tyr^{GUA} mimetic to identify interacting proteins

A 5' biotinylated 37-nucleotide tRF-Tyr^{GUA} mimetic (CCUUCGAUAG-CUCAGCTGGUAGAGCGGAGGACUGUAG) and a scrambled control oligo (GAGACCAGGGUACGCAAUCGAGUUGUUGGGCACUCUG) were synthesized (IDT). Each mimetic was incubated at 4°C with equal amounts of MCF10A cell lysate containing protease inhibitor that had been pre-cleared for debris and by the control oligo. Proteins bound to our mimetic were co-precipitated by MyOne-C1 Streptavidin Dynabeads (Invitrogen) and washed twice with a low salt wash buffer (50 mM Tris– HCl pH 7.5, 150 mM NaCl) and twice with a high salt wash buffer (50 mM Tris–HCl pH 7.5, 400 mM NaCl) before being submitted to the Rockefeller University Proteomics Resource Center.

5.8 RNA stability of hnRNPA1 bound transcripts

MCF10A cells were reverse transfected with a control siRNA or siRNA targeting hnRNPA1 with either a tRFTyrGUA mimetic or a scrambled mimetic using Lipofectamine RNAimax (Invitrogen). For the converse experiment, siRNA was reverse transfected as above into MCF10A cells using Lipofectamine RNAimax. A miRNA inhibitor (LNA) targeting tRFTyrGUA (GAUAGCUCAGUUGGUAGAGCG- GAGGA) or non-targeting control (UCGUUAAUCGGCUAUAAU ACGC) was directly transfected 24 h later. After 48 h, half of the samples were treated with a-amanitin (10 mg/ml, Sigma) and incubated for 8 h while the other half were processed as the 0 h time point. RNA was extracted using TRIzol and RNA-seq libraries were prepared using QuantSeq 30 mRNA-seq kit (Lexogen) or TruSeq RNA Library Prep (Illumina) following the manufacturers' instructions.

5.9 SSB HITS-CLIP with and without RNase

HITS-CLIP for endogenous SSB was done as previously described[124], with the modifications previously used for YBX1 small RNA CLIP[88]. MDA-MB-231 cells were UV-crosslinked at 400 mJ/cm^2 before cell lysis. Samples with and without RNase treatment were immunoprecipitated with an anti-SSB antibody for protein-RNA complexes. Polyphosphatase (Lucigen) was incubated with smRNA samples before ligation and PCR amplification with previously described primers[88]. Constructed libraries were sequenced on the Illumina HiSeq2000 at the Rockefeller University Genomics Center.

5.10 RNA isolation and purification

RNA was extracted from cells with either Norgen BioTek Total RNA isolation kit following the manufacturers instructions, or using TRIzol reagent (Life Sciences) followed by isopropanol precipitation at -20ºC. After centrifugation at maximum speed (~21,000 x g) in a pre-chilled

tabletop microcentrifuge, RNA pellet was washed twice with cold 75% ethanol following resuspension in RNase free water.

5.11 Northern Blot

Purified RNA was run on a 10% Urea-PAGE gel before being transferred onto a nylon membrane and UV crosslinked (240 mJ/cm^2). The membrane was pre-hybridized in UltraHyb-Oligo buffer (Ambion) at 42°C. DNA oligos were radiolabeled with [γ-^{32}P] ATP using T4 PNK (NEB) and further purified by G-50 columns before incubating with the blot overnight. After hybridization, the blot was washed twice with SSC and SDS buffers before being developed. Quantification was done using FIJI (ImageJ) where the intensity of each band over background was measured and normalized to U6 levels.

Table 5.1. ^{32}P labeled probes used for detection by northern blot

Target	Species	Sequence
tRNA-Leu^{CAG}	*H.sapiens, M.musculus*	AGGGGAGACTGCGACCTGAACG
tRNA-Leu^{TAG}	*H.sapiens, M.musculus*	CTCCGAAGAGACTGGAGCCTAAA
tRNA-Leu^{AAG}	*H.sapiens, M.musculus*	CCCCGAAGAGACTGGAGCCTTAA
U6	*H.sapiens*	CACGAATTTGCGTGTCATCCTT
U6	*M.musculus*	GCCATGCTAATCTTCTCTGTATCGTTCCAAT
tRNA-Tyr^{GUA}	*H.sapiens*	ACAGTCCTCCGCTCTA CCAGCTGA
tRNA-Tyr^{GUA}	*C.elegans*	ACAGTCCTCCGCTCTACCAACTGA
tRNA-Leu^{HAG}	*H.sapiens*	CAGCGCCTTAGACCGCTCGGCCA
tRNA-His^{GUG}	*H.sapiens*	AACGCAGAGTACTAACCACTATACG
tRNA-Glu^{YUC}	*H.sapiens*	GCGCCGAATCCTAACCACTAGACCA
U1	*H.sapiens*	CAAATTATGCAGTCGAGTTTCCCACATTTG

5.12 Charged tRNA profiling

5.12.1 Acidic RNA extraction

1 day prior to RNA extraction, MCF10A, HCC1806 and HCC1806 LM2C cells were plated to be 80% confluent at time of RNA harvest. On the day of harvest, cells pellets were lysed in 600 μl cold lysis buffer (0.3 M NaOAc, pH 4.5, 10 mM EDTA pH 8), and extracted twice with

equivalent volume acidic phenol chloroform (pH 4.5, ThermoFisher). During each extraction, samples were vortexed 3 times for 30 seconds prior to centrifugation for 10 minutes at maximum speed in a cold microcentrifuge, and the aqueous layer was transferred to anew tube. Nucleic acids were precipitated with 2.5 volumes of ethanol and 2 μl GlycoBlue (Invitrogen) overnight. Following nucleic acid recovery by 20 minute cold centrifugation at maximum speed, a second precipitation was conducted in 2.5 volumes of ethanol and 2 μL GlycoBlue. Precipitations were centrifuged for 20 minutes at maximum speed at 4ºC, and nucleic acids were resuspended in 30 μL of 10 mM NaOAc (pH 4.5).

5.12.2 Sodium periodate oxidation and precipitation

To oxidize free 3'OH on uncharged tRNAs, for each sample, 20μg RNA (at concentration 0.1 μg/μL) was treated with 50 mM $NaIO_4$ (or 50 mM NaCl as a control), in the presence of 100mM KOAc (pH 4.8). Samples were incubated at 22ºC for 30 minutes, and 100 mM glucose added to quench the reaction for an additional 5 minutes. To clean up and enrich for tRNAs, samples were filtered through microRNA enrichment columns (microRNA Purification Kit, Norgen Biotek) according to the manufacturer's instructions. Following ethanol precipitation, samples were filtered through a Sephadex G25 column (GE Life Sciences) to remove excess $NaIO_4$ and precipitated twice with ethanol premixed with 0.1x NaOAc (3M, pH 4.5) and 2 μL GlycoBlue.

5.12.3 tRNA profiling

tRNA profiling was conducted as previously described[66]. Briefly, samples were deacylated with 0.1 M Tris-HCl (pH 9) at 37ºC for 30 minutes followed by ethanol:isopropanol precipitation. 0.75 μg of each sample was biotinylated using Pierce RNA 3' End Biotinylation Kit (Thermo Fisher), with 0.66 pmol of yeast tRNA-Phe added as a spike-in standard. Following chloroform

extraction, biotinylated RNA was hybridized to DNA probe pairs complementary to the 3' and 5' arms of each tRNA isoacceptor. Nicks at the anticodon loop of DNA-RNA hybrids were ligated using SplintR ligase followed by T4 DNA ligase (NEB). DNA-RNA hybrids were purified using My-One-C1 Streptavidin Dynabeads (Invitrogen), and ligated probes were eluted after RNase H and RNase A treatment. Probes were PCR amplified and sequenced using Illumina NextSeq (MidOutput, 150 SR) at the Rockefeller University Genomics Center. For computational analysis, fastq files were aligned to tRNA probe sequences using bowtie2, and reads were further sorted, indexed, and counts were generated with samtools. Raw counts were imported into R 4.0.2 and differentially expressed transcripts determined using DESeq2.

5.13 Quantitative RT-PCR

To measure mRNA transcript levels, RNA was converted to cDNA (SuperScript III, Life Technologies) followed by Fast SYBR™ Green quantification (Life Technologies) according to manufacturer's instructions. Expression levels of mRNA were performed with either an ABI Prism 7900HT Real-Time PCR System (Applied Biosystems) or a QuantStudio 5 Real-Time PCR System (Applied Biosystems) using target-specific primers.

Table 5.2. Target-specific primers used for qRT-PCR.

Target Gene	Organism	Sequence
LARS	*H.sapiens*	GGACAGCCTTGCATGGATCAT
		TAGATGGGTATGGCTCAAGCA
GAPDH	*H.sapiens*	AGCCACATCGCTCAGACAC
		GCCCAATACGACCAAATCC
AARS	*H.sapiens*	GGGGCAAACATAATGACCTGG
		GCCAAACTCTTGGGTGAGGA
CARS	*H.sapiens*	CCATGCAGACTCCACCTTTAC
		GCAATACCACGTCACCTTTTTC
DARS	*H.sapiens*	ATCGAGTTTTGGTTCGGGTTAG
		TCCCTTTAGCTCTGCTTGTATGA
EPRS	*H.sapiens*	GTGTTTGGGCCACCCTAAAAG

		CTGGAGGAAATCTGACGGTAAC
FARSA	*H.sapiens*	CCCAGAGCGAGCTTATGCG
		CACCCGAATCCACTTGTTGG
FARSB	*H.sapiens*	AAGGATTGGTTCGAGGACTTCA
		CCATCAGGCATTACCCGTTTAT
GARS	*H.sapiens*	ATGGAGGTGTTAGTGGTCTGT
		CTGTTCCTCTTGGATAAAGTGCT
HARS	*H.sapiens*	GTGGCGAAACTCCTGAAACTG
		AAGCAACGGATGATTACGTCAA
IARS	*H.sapiens*	CTGTTAGCAGACTTGGCCGAT
		AGAAGGGCATGACTTTCACAC
KARS	*H.sapiens*	GAGCTGAGCATCATTCCGTATG
		GGCGATACCTTGTTTCCTTGT
MARS	*H.sapiens*	ATCTGGCTGGGAGCAAGATGA
		GGACCACTAAATAGTACAGGGCA
NARS	*H.sapiens*	ACCATCTCGCAACACCAGAAA
		CTGGTGTTGCGAGATGGTACA
QARS	*H.sapiens*	TCCCGACTCAGGGATACCC
		CTCCGCACATACTCAAGGGC
RARS	*H.sapiens*	ACTGTGGCTGTTTAGGAGCTT
		ACCTCTTGTAGGCGGCTAATAA
SARS	*H.sapiens*	CAGCCCTCATCCGAGAGAC
		TCTGCCCGAAATCTACATCGT
TARS	*H.sapiens*	GGAGAAGCCGATTGGTGCT
		TCAACTCAGCTCGACCTCCAT
VARS	*H.sapiens*	TACGCCGACACGGAGTTAATA
		TCTAGGACGTATCGGAAAGGC
WARS	*H.sapiens*	AGCACCTACCAGTAATCATGGC
		TCCAAACCGAACAATGAGCTT
YARS	*H.sapiens*	ACCTCCACGCATACCTGGATA
		TTGCTGAGCTGGTAATCAGTG
Lars	*M.musculus*	GAGCAGCAAGGGCAAATACTT
		GAAAACGTGTGTCCCAAATGAAG
Gapdh	*M.musculus*	GAGAGTGTTTCCTCGTCCCG
		ACTGTGCCGTTGAATTTGCC
Emp3	*M.musculus*	TCTCCGGGGCACTCATCTATG
		GCGAAGCAGTAACCGAAGC
Ggt5	*M.musculus*	TGCTGGGTGTAGGTCTAGGTC
		TGCTGGGTGTAGGTCTAGGTC

5.14 Polysome profiling and sequencing

5.14.1 Lysate preparation and fractionation

Polysome profiling was adapted from previously described protocols[147]. Cells were plated for harvest at 80% confluence to optimize polysome content (n=3 per condition). Prior to lysis, plates were treated for 5-7 minutes with media containing 100 μg/mL cycloheximide (Alfa Aesar). Following PBS wash, plates were flash frozen in liquid nitrogen and lysed via scraping using 425 μL polysome lysis buffer (5 mM Tris HCl pH 7.5, 2.5 mM MgCl2, 1.5 mM KCl, 100 μg/mL cycloheximide, 2 mM DTT, 0.5% Triton X-100, 0.5% sodium deoxycholate, 100 units of SUPERase*In RNase Inhibitor (Invitrogen), and 1x Protease Inhibitors EDTA-free). Lysates were then spun at high speed at 4^{o}C for 7 minutes to pellet nuclei. Supernatant was transferred to a new tube and the RNA concentration was measured using the Quant-iT RiboGreen assay (Life Technologies). 10-50% sucrose gradients were mixed using a Biocomp gradient master with the following conditions: Short Cap, 10% - 50% WV Step 1, 1:50 minutes, 80^{o} angle, 21 speed. Following loading of 150 μg of each lysate, gradients were spun using SW41 rotor at 38,000 RPM for 2 hours at 4ºC. Gradients were fractionated into 16 fractions, using a Triax FlowCell Gradient Fractionator according to the manufacturer's instructions.

5.14.2 Fraction pooling and sequencing analysis

Based on A280 UV peaks, fractions were pooled based on highly translated (3+ ribosomes) and lowly translated (1-2 ribosomes) and RNA was extracted using Trizol LS reagent (Life sciences) according to the manufacturer's instructions. 1 μg of RNA was used as input for RNA sequencing library preparation using TruSeq RNA Library Prep (Illumina). Constructed libraries were sequenced using Illumina NextSeq (High Output, 75 SR) at the Rockefeller University Genomics Center. For analysis, fastq files were aligned to mouse genome (mm10) using STAR

(v2.5.2a) and reads that were aligned to coding sequences were counted using featureCounts. Raw counts were imported into R and differentially expressed transcripts determined using DESeq2.

5.15 RiboTag immunoprecipitation and sequencing

Tumours were extracted from 24-week old animals and processed as previously described[96,104]. Briefly, 50 mg of isolated flash frozen tumours were lysed in 10% w/v homogenization buffer (1% NP-40, 100 mM KCl, 50 mM Tris pH 7.4, 12 mM $MgCl_2$, 1 mM DTT, 200 U/mL Promega RNasin (Promega), 1 mg/mL heparin, 100 μg/mL cycloheximide, protease inhibitor (Sigma)) using a microtube homogenizer (Cole-Parmer). Following 10 minute spin at maximum speed in a cold microcentrifuge, cleared samples were incubated with 100 μL of conjugated anti-HA magnetic beads (ThermoFisher, #88836) for 1 hour rotating at 4ºC. Samples were magnetized and bead pellets were washed three times in high salt buffer (50 mM Tris, pH 7.4, 300 mM KCl, 12 mM $MgCl_2$, 1% NP-40, 1 mM DTT, 100 μg/mL cycloheximide). RNA isolation was conducted using 350 μL Qiagen RLT buffer supplemented with 2-mercaptoethanol added directly to washed beads. Total RNA extraction was completed using RNeasy Micro Plus kit (Qiagen) according to the manufacturer's instructions. 500 ng of RNA was used for RNA sequencing library preparation using TruSeq RNA Library Prep (Illumina). Constructed libraries were sequenced using Illumina NextSeq (High Output, 75 SR) at the Rockefeller University Genomics Center. For analysis, fastq files were aligned to mouse genome (mm10) using STAR (v2.5.2a) and reads that were aligned to coding sequences were counted using featureCounts. Raw counts were imported into R 4.0.2 and differentially expressed transcripts determined using DESeq2.

5.16 Ribo-Seq

5.16.1 Sample isolation and library preparation

Ribosome profiling was conducted as previously described[105]. Briefly, cells were washed and flash frozen with liquid nitrogen before being lysed with lysis buffer containing cycloheximide (Alfa Aesar). Lysate was digested with RNase I (Lucigen) before ribosomes were isolated through ultracentrifugation through a sucrose cushion. The ribosome pellet was resuspended in a solubilization buffer containing 0.5% SDS and 1mM EDTA and TRIzol before RNA was extracted using the Direct-zol kit (Zymo Research). RNA was separated on a 15% TBE-Urea gel before RNA between 17nt and 34nt were gel extracted. Barcoded pre-adenylated linkers were ligated using T4 RNA ligase 2 truncated K227Q (NEB) and rRNA was depleted using the Ribo-Zero gold kit (Illumina) according to the manufacturer's protocol. RNA was converted to cDNA using SuperScript III (Life Technologies) and the RT product was circularized by CircLigase II (Epicentre). A PCR library was amplified and sequenced using Illumina Nextseq (High Output, 75 SR) at the Rockefeller University Genomics Center.

5.16.2 Ribosome dwell time analysis

To assess the quality of ribo-seq data, we checked read length distribution and frame periodicity – overall and stratified by read length –using the R package riboWaltz[114]. Reads in the length range of 28:36 were retained. We next calculated P-site offsets, and assigned reads to codon positions to determine codon usage.

We compared ribosome dwell times at specific codons along transcripts with at least 10 reads in all samples. Background translation rate for each transcript was determined as the median of

non-zero rpf read counts among the codons after loess smoothing of observed counts. An excess ratio was calculated at each codon position as the ratio of smoothed rpf counts at that position divided by the transcript background. We named the geometric mean of excess ratios across replicates “stalling bias coefficient” – which is proportional to ribosomal dwell time and inversely proportional to codon decoding rate or local translation rate. Then, we compared the relative dwell times at each codon type across cell lines using linear models in R and plotted the results using the jtools package. shLars-3 and shLars-4 were compared to shCtrl as the reference line.

5.16.3 Sequence discrepancy analysis

To assess the effect of clusters of Leu codons on local translation rates, we used a measure called "sequence discrepancy" implemented in the R package DiceDesign which was developed based on the theory expounded by Hickernell[148]. Sequence discrepancy is in the range [0-1] with values close to 0 corresponding to uniform (even) distribution and values close to 1 indicating strong clustering of points. For each transcript, we calculated sequence discrepancy of Leu residues. Discrepancy indices were $\log_2$ transformed to reduce skewness. We regressed the average dwell time (stalling bias coefficient) of Leu codons of each transcript against its $\log_2$ transformed Leu discrepancy. We also checked for potential confounding effects of transcript length and the total number of Leu residues.

5.17 Protein isolation

5.17.1 Protein isolation in cultured cells

Pelleted cells were lysed using RIPA buffer (Life Sciences) using HALT protease inhibitor cocktail (Sigma). Genomic DNA was sheared through a 27G needle, followed by centrifugation

to clear cellular debris. Concentration of cleared protein lysates were quantified using BCA protein assay kit (Thermo Fisher) according to the manufacturer's instructions.

5.17.2 Protein isolation from flash frozen tissue samples

Flash frozen tissue samples of 50-100 mg were isolated over dry ice and lysed using 100-200 μL RIPA buffer with HALT protease inhibitor cocktail. Tissue homogenization was conducted using a microtube homogenizer (Cole-Parmer), followed by centrifugation and quantification of cleared protein lysate as above.

5.17.3 Protein isolation from organoid samples

Organoid samples were digested from reduced growth factor Matrigel in 10mM EDTA in PBS for 1 hour at 4ºC, After centrifugation and resuspension in 20-40 μL RIPA buffer, protein lysate samples were cleared and quantified as above.

5.18 Western blot

Samples were heated with LDS buffer and reducing agent (Life sciences) before running on an SDS-PAGE gel and transferred to a PVDF membrane (Bio-Rad). Membranes were blocked using 5% BSA or Odyssey blocking buffer (PBS) and then incubated with target-specific antibodies.

Table 5.3. Target-specific antibodies used for Western blot.

Target	Company	Product Number	Dilution
LARS	Cell Signaling	13868S	1:1000
HSC70 (B6)	Santa Cruz	sc-7298	1:3000
PyMT	Novus Biologicals	NB100-2749	1:2500
EMP3	Abcam	Ab236671	1:500
GGT5	GeneTex	GTX81477	1:500
α-tubulin	Cell Signaling	3873S	1:1000
HARS	Proteintech	16375-1-AP	1:1000
NARS	Aviva Systems Biology	OAAB07325	1:1000

IARS	ThermoFisher	PA5-44246	1:1000
HA	BioLegend	901501	1:1000
Luciferase	Proteintech	27986-1-AP	1:1000
YARS	Abcam	Ab150429	1:1000
EPCAM	Proteintech	21050-1-AP	1:1000
SCD	Proteintech	23393-1-AP	1:1000
USP3	Proteintech	12490-1-AP	1:1000
SSB	MBL	RN074PW	1:1000
hnRNPA1	Santa Cruz	Sc-32301	1:1000
hnRNPA0	Bethyl Laboratories	A303-941A	1:1000
DIS3L2	Novus Biologicals	NBP2-38264	1:1000
Myc	Cell Signaling	2276S	1:1000

5.19 Tandem mass tag proteomics

Flash frozen tissue samples were lysed as above in detergent free lysis buffer containing 20 mM Tris-HCl pH 7.4, 100 mM KCl, 1 mM EDTA pH 8, 0.5% NP-40 and cOmplete protease inhibitor (Sigma) and homogenized using a microtube homogenizer (Cole-Parmer). For proteomic analysis, 100 μg of lysate was acetone precipitated and dissolved in 100 μl 8 M Urea/50 mM triethyl ammonium bicarbonate/10 mM DTT. After 1 hour of incubation at room temperature, reduced cysteines were alkylated with iodoacetamide (Sigma) in the dark for 1 hour. Proteins were extracted by chloroform/water/methanol precipitation, and then were digested overnight using LysC endopeptidase and trypsin (NEB). TMT reagents (ThermoFisher Scientific) were dissolved in neat acetonitrile and samples were labeled for 1 hour at room temperature before quenching with 5% hydroxylamine. A label check was conducted to verify labeling efficiency and stoichiometry. Samples were mixed based on the results from the label check and the pooled sample was purified using a high-capacity Oasis HLB cartridge. Purified peptides were fractionated using a reversed-phase high pH fractionation spin column (Pierce). Each fraction was separated by low-pH reversed-phase nano-flow chromatography across a 120-minute linear gradient and analyzed by SPS-MS3 acquisition using a Fusion Lumos

mass spectrometer (Thermo Scientific). Spectra were queried against the Mus musculus proteome using Sequest HT through Proteome Discoverer v. 2.5 (Thermo Scientific). Further statistical processing was performed using Perseus v.1.6.5.0[149].

5.20 Animal studies

All animal work was conducted in accordance with protocols approved by the Institutional Animal Care and Use Committee at The Rockefeller University. $Lars^{tm1a(KOMP)Wtsi}$ knockout mice were obtained from KOMP Repository at UC Davis[95]. FlpE animals were obtained from the Michel Nussenszweig laboratory. RPL22 floxed (Ribotag) mice were obtained from the Jackson laboratory[25].

5.21 Genetically initiated models of breast cancer

5.21.1 MMTV-PyMT LARS knockout model

Within the laboratory, C57BL/6 mice were crossed with MMTV-PyMT[24], MMTV-Cre[150] positive mice for at least 8 generations to maintain a C57BL/6 background. Following FlpE-mediated recombination, animals homozygous for $Lars^{tm1a}$ were crossed to MMTV-Cre/MMTV-PyMT hemizygous mice to generate heterozygous *Lars* deletion in the mammary tumour compartment. Overall tumour burden was measured weekly beginning at week 12, when primary tumours spontaneously begin to form, using digital calipers and calculating individual tumour volumes as $(\text{smaller diameter})^2 \times (\text{larger diameter}) \times \pi / 6$. Animals were sacrificed at 24 weeks of age (or at first sign of distress from excessive tumour burden), and mammary tumours were isolated for histology, organoid generation, and flash frozen for RNA and protein extraction, while lungs were isolated for paraffin fixation, all as described above.

5.21.2 RiboTag

Homozygous RPL22 floxed (Ribotag) mice were crossed to MMTV-PyMT+; MMTV-Cre+; heterozygous Lars knockout mice to generate animals heterozygous for HA-RPL22 in the mammary tumour compartment, either heterozygous deletion of *Lars* or wild-type *Lars* expression. Size-matched tumours were extracted from age-matched littermates at 24 weeks of age for use in RiboTag studies.

Table 5.4. Genotyping primers and expected product sizes

Target	Expected Size	Primer Name	Sequence
MMTV-PyMT	MMTV-PyMT 556 bp Control 200 bp	PyMT Forward	GGAAGCAAGTACTTCACAAGGG
		PyMT Reverse	GGAAAGTCACTAGGAGCAGGG
		PyMT Control-Forward	CAAATGTTGCTTGTCTGGTG
		PyMT Control-Reverse	GTCAGTCGAGTGCACAGTTT
MMTV-Cre	MMTV-Cre 250 bp	Forward	CTGATCTGAGCTCTGAGTG
		Reverse	CATCACTCGTTGCATCGACC
FlpE	FlpE 100 bp Control 324 bp	FlpE Forward	TGCCGGTCCTATTTACTCGT
		FlpE Reverse	TACTTCTTTAGCGCAAGGGGTAG
		FlpE Control-Forward	CTAGGCCACAGAATTGAAAGATCT
		FlpE Control-Reverse	GTAGGTGGAAATTCTAGCATCATCC
LARS	LARS pre-flp 630 bp LARS post-flp 545 bp WT 368	CSD-NeoF	GGGATCTCATGCTGGAGTTCTTCG
		CSD-ttR	AAACCAAAGCTAACTGAACCGCTGG
		CSD-LARS-F	ACCTTGTGTGTATGCGTGTGACTATG
		CSD-LARS-R	TGCATGAGTGTTCTATTGAGCAGGC
RPL22 HA	Floxed 290 bp WT 243 bp	RiboTag LoxP Forward	GGGAGGCTTGCTGGATATG
		RiboTag LoxP Reverse	TTTCCAGACACAGGCTAAGTACAC

5.22 Tumor formation studies

500,000 NMuMG cells expressing the PyMT oncogene or empty control were injected into the fourth mammary gland of 8-12-week-old age-matched female NSG mice (4-5 mice per group.) Tumor size was measured biweekly.

5.23 In vivo metabolite profiling

1,000 4T07 cells expressing control shRNA or shRNA targeting LARS were injected into the fourth mammary gland of 8–10-week-old age-matched female balb/cJ mice (5 mice per group). Tumour size was measured biweekly, animals were euthanized and tumours were harvested 14 days post inoculation for metabolomic studies. 10-30 mg flash frozen tissue samples were homogenized using tissue homogenizer in 80% LC-MS grade methanol/water (v/v). samples were vortexed and centrifuged at maximum speed at 4ºC for 10 minutes. Supernatant was transferred to new tubes. Samples were dried to completion using a nitrogen dryer and then reconstituted in 30 µl 2:1:1 LC-MS water:methanol:acetonitrile for Liquid-chromatography coupled to High-Resolution Mass Spectrometry (LC-HRMS). The injection volume for polar metabolite analysis was 5 µl.

5.24 Histology

Mouse lung and mammary fat pad samples were prepared by perfusion fixation with 4% paraformaldehyde through the right ventricle and incubated in 4% paraformaldehyde overnight. Samples were dehydrated and stored in 70% ethanol, and paraffin embedded and sectioned in 5 μm slices for staining with hematoxylin and eosin (H&E) and by immunofluorescence as described below.

5.25 Immunofluorescence

Paraffin embedded slides were deparaffinized using five-minute washes in xylenes (x2), 100% ethanol, 95%, 80% and 70% ethanol. Following deparaffinization, slides were washed in 1X PBS and antigen retrieval was conducted in boiling 1X citrate buffer pH 6 (Sigma) for 20 minutes. Slides were cooled to room temperature and then blocked in 5% goat serum (Sigma Aldrich) in PBS with 0.05% Tween-20 for 30 minutes in a humid chamber. Primary antibody

against Ki-67 (Abcam, ab16667, 1:1000) was diluted in blocking solution and samples were incubated overnight at 4ºC. Slides were washed three times with PBS-Tween for 5 minutes prior to secondary antibody incubation at 1:200 in blocking solution and incubation at room temperature for 1 hour.

Slides were again washed with PBS-Tween three times, with the final wash containing 5 ug/mL DAPI nuclear stain (Roche). Slides were washed once more, dried and mounted using ProlonGold Antifade (Invitrogen). Fluorescence intensity was measured on a Zeiss inverted LSM 780 laser scanning confocal microscope at the Bioimaging Resource Center at Rockefeller University. Images were analyzed using ImageJ, by calculating mean fluorescence intensity of sample to normalized DAPI signal.

5.26 Organoid assays

5.26.1 Generation and culture

Organoids were isolated from MMTV-PyMT animal tumours as previously described[22]. Briefly, size-matched mammary tumours were isolated and minced with scalpel followed by collagenase digestion at 37ºC. Digested tumours were DNase treated, and differential centrifugation cycles were conducted at 170 x g for 4 seconds each to isolate organoids from single cell contaminants. Organoids were counted and resuspended at 100-300 organoids per well in reduced growth factor Matrigel (Corning). Following gel solidification, ß-FGF-containing growth factor media was added to all wells.

Plated organoids were passaged or frozen by mechanical digestion of reduced growth factor Matrigel in 10mM EDTA in PBS for 1 hour at 4ºC, followed by centrifugation and resuspension in reduced growth factor Matrigel (passage) or 90% fetal bovine serum with 10% DMSO (freezing).

5.26.2 Lentiviral transduction

Small organoids were collected following generation by pulsing to 300 rpm for 3 seconds and collecting organoids within the supernatant. Lentivirus collected from 10 cm plates and concentrated overnight using Lenti-X concentrator (TaKaRa) was used to transduce organoids by either magnetofection using ViroMagR/L reagent (OZ Biosciences) according to the manufacturer's recommendation, or by spinfection in ultra-low attachment 96-well plates with 4ug/ml polybrene at 1500 x *g* for 1 hour. 800 organoids were cultured with 25% of 10-cm plate concentrated virus into either 50 or 125 μL total volume. Following overnight incubation at 37ºC, media was refreshed and puromycin selection was conducted 24 hours later at 1 μg/mL for 3 days.

5.26.3 Growth assays

250 organoids were plated in reduced factor Matrigel (Corning) in glass-bottom plates (USA Scientific). 2D images were acquired of individual organoids on day 1, 3, 5 and 8 after plating using either a Zeiss CellDiscoverer 7 microscope or a Nikon TiE inverted microscope with Andor Neo sCMOS camera. Images were quantified using ImageJ to outline individual organoids. Growth was calculated as a ratio of the 2D projected area of individual organoids on Day 5-8 compared to Day 1 area.

5.26.4 Inhibitor studies

250 organoids were plated in reduced growth factor Matrigel (Corning) in glass-bottom or polystyrene plates. Organoid growth media was supplemented with 12.5μM, 25 μM or 50μM BC-LI-0186 compound, and media was refreshed every 48 hours. Growth assays were conducted by 2D images acquision as described above.

5.27 Codon reporter assays

HA-tagged constructs were synthesized by IDT and cloned into the psiCHECK2 vector (Promega), replacing the synthetic Renilla luciferase gene. A 6x glycine linker was placed between the HA tag and the gene. Constructs included wild-type EMP3 gene or EMP3 gene with sets of 10 Leu CTC and CTG codons mutated to Leu TTG residues. 500,000 NMuMg shLars knockdown cells were seeded overnight for transient transfection in 6-well plates. Transfections were performed using 3 μg DNA and 9 μL Lipofectamine 2000 per well (Invitrogen). Cells were harvested 48 hours post transfection for analysis of reporter expression levels by quantitative western blot.

CHAPTER 6. References

Parts of this thesis are based on published work. Permission to use this work in the thesis has been obtained from the publisher:

Huh, D., **Passarelli MC**, et al. A stress-induced tyrosine-tRNA depletion response mediates codon-based translational repression and growth suppression. EMBO J. 40, 1‑16 (2021).

1. Surveillance Research Program, N. C. I. SEER*Explorer: An interactive website for SEER cancer statistics.
2. Fouad, Y. A. & Aanei, C. Revisiting the Hallmarks of Cancer. *Am. J. Cancer Res.* **7**, 1016–1036 (2017).
3. Hanahan, D. & Weinberg, R. A. Hallmarks of cancer: The next generation. *Cell* **144**, 646–674 (2011).
4. Tabassum, D. P. & Polyak, K. Tumorigenesis: It takes a village. *Nat. Rev. Cancer* **15**, 473–483 (2015).
5. Denis, D., Rouleau, C. & Schaffhausen, B. S. A Transformation-Defective Polyomavirus Middle T Antigen with a Novel Defect in PI3 Kinase Signaling. *J. Virol.* **91**, 1–14 (2017).
6. Dimri, G., Band, H. & Band, V. Mammary epithelial cell transformation: Insights from cell culture and mouse models. *Breast Cancer Res.* **7**, 171–179 (2005).
7. Yusuf, R. & Frenkel, K. Morphologic transformation of human breast epithelial cells MCF-10A: dependence on an oxidative microenvironment and estrogen/epidermal growth factor receptors. *Cancer Cell Int.* **10**, 15–20 (2010).
8. Zientek-Targosz, H. *et al.* Transformation of MCF-10A cells by random mutagenesis with frameshift mutagen ICR191: A model for identifying candidate breast-tumor suppressors.

Mol. Cancer **7**, 1–12 (2008).

9. Kadota, M. *et al.* Delineating genetic alterations for tumor progression in the MCF10A series of breast cancer cell lines. *PLoS One* **5**, 1–10 (2010).
10. Clevers, H. Modeling Development and Disease with Organoids. *Cell* **165**, 1586–1597 (2016).
11. Nguyen-Ngoc, K.-V. *et al.* 3D Culture Assays of Murine Mammary Branching Morphogenesis and Epithelial Invasion. *Methods Mol Biol* **1189**, 135–162 (2015).
12. Padmanaban, V. *et al.* E-cadherin is required for metastasis in multiple models of breast cancer. *Nature* **573**, 439–444 (2019).
13. Simian, M. & Bissell, M. J. Organoids: A historical perspective of thinking in three dimensions. *J. Cell Biol.* **216**, 31–40 (2017).
14. Linnemann, J. R. *et al.* Quantification of regenerative potential in primary human mammary epithelial cells. *Dev.* **142**, 3239–3251 (2015).
15. Ootani, A. *et al.* Sustained in vitro intestinal epithelial culture within a Wnt-dependent stem cell niche. *Nat. Med.* **15**, 701–706 (2009).
16. Gao, D. *et al.* Organoid cultures derived from patients with advanced prostate cancer. *Cell* **159**, 176–187 (2014).
17. Van De Wetering, M. *et al.* Prospective derivation of a living organoid biobank of colorectal cancer patients. *Cell* **161**, 933–945 (2015).
18. Boj, S. F. *et al.* Organoid models of human and mouse ductal pancreatic cancer. *Cell* **160**, 324–338 (2015).
19. Sachs, N. *et al.* A Living Biobank of Breast Cancer Organoids Captures Disease Heterogeneity. *Cell* **172**, 373-386.e10 (2018).

20. Georgess, D. *et al.* Twist1-induced epithelial dissemination requires PRKD1 signaling. *Cancer Res.* **80**, 204–218 (2020).

21. Fantozzi, A. & Christofori, G. Mouse models of breast cancer metastasis. *Breast Cancer Res.* **8**, (2006).

22. Aktary, Z., Corvelo, A., Estrin, C. & Larue, L. Sequencing two Tyr::CreERT2 transgenic mouse lines. *Pigment Cell Melanoma Res.* **33**, 426–434 (2020).

23. Dankort, D. *et al.* Braf(V600E) cooperates with Pten loss to induce metastatic melanoma. *Nat. Gen* **41**, 544–552 (2009).

24. Guy, C. T., Cardiff, R. D. & Muller, W. J. Induction of Mammary Tumors by Expression of Polyomavirus Middle T Oncogene : A Transgenic Mouse Model for Metastatic Disease. *Mol. Cell. Biol.* **12**, 954–961 (1992).

25. Astolfi, A. *et al.* Gene Expression Analysis of Immune-Mediated Arrest of Tumorigenesis in a Transgenic Mouse Model of HER-2 / neu-Positive Basal-Like Mammary Carcinoma. **166**, 1205–1216 (2005).

26. Ruggero, D. Translational control in cancer etiology. *Cold Spring Harb. Perspect. Biol.* **5**, (2013).

27. Silvera, D., Formenti, S. C. & Schneider, R. J. Translational control in cancer. *Nat. Rev. Cancer* **10**, 254–266 (2010).

28. Robichaud, N., Sonenberg, N., Ruggero, D. & Schneider, R. J. Translational control in cancer. *Cold Spring Harb. Perspect. Biol.* **11**, (2019).

29. Hsieh, A. C. *et al.* The translational landscape of mTOR signalling steers cancer initiation and metastasis. *Nature* **485**, 55–61 (2012).

30. Barna, M. *et al.* Suppression of Myc oncogenic activity by ribosomal protein

haploinsufficiency. *Nature* **456**, 971–975 (2008).

31. Miluzio, A. *et al.* Impairment of cytoplasmic eIF6 activity restricts lymphomagenesis and tumor progression without affecting normal growth. *Cancer Cell* **19**, 765–775 (2011).

32. Wolfe, A. L. *et al.* RNA G-quadruplexes cause eIF4A-dependent oncogene translation in cancer. *Nature* **513**, 65–70 (2014).

33. Furic, L. *et al.* EIF4E phosphorylation promotes tumorigenesis and is associated with prostate cancer progression. *Proc. Natl. Acad. Sci. U. S. A.* **107**, 14134–14139 (2010).

34. Ebright, R. Y. *et al.* Deregulation of ribosomal protein expression and translation promotes breast cancer metastasis. *Science (80-.).* **367**, 1468–1473 (2020).

35. Faller, W. J. *et al.* MTORC1-mediated translational elongation limits intestinal tumour initiation and growth. *Nature* **517**, 497–500 (2015).

36. Gingold, H. *et al.* A dual program for translation regulation in cellular proliferation and differentiation. *Cell* **158**, 1281–1292 (2014).

37. Wilusz, J. E. Controlling translation via modulation of tRNA levels. *Wiley Interdiscip. Rev. RNA* **6**, 453–470 (2015).

38. Gobet, C. *et al.* Robust landscapes of ribosome dwell times and aminoacyl-tRNAs in response to nutrient stress in liver. *PNAS* 1–12 (2020) doi:10.1073/pnas.1918145117.

39. Pavlova, N. N. *et al.* Translation in amino-acid-poor environments is limited by tRNA Gln charging. *Elife* 1–27 (2020) doi:https://doi.org/10.7554/eLife.62307.

40. Loayza-Puch, F. *et al.* Tumour-specific proline vulnerability uncovered by differential ribosome codon reading. *Nature* **530**, 490–494 (2016).

41. Knott, S. R. V. *et al.* Asparagine bioavailability governs metastasis in a model of breast cancer. *Nature* **554**, 378–381 (2018).

42. Darnell, A. M., Subramaniam, A. R. & O'Shea, E. K. Translational Control through Differential Ribosome Pausing during Amino Acid Limitation in Mammalian Cells. *Mol. Cell* **71**, 229-243.e11 (2018).

43. Pang, Y. L. J., Poruri, K. & Martinis, S. A. tRNA Synthetase: tRNA Aminoacylation and beyond. *Wiley Interdiscip Rev RNA* **5**, 461–480 (2015).

44. Yadavalli, S. S. & Ibba, M. Selection of tRNA charging quality control mechanisms that increase mistranslation of the genetic code. *Nucleic Acids Res.* **41**, 1104–1112 (2013).

45. Cusack, S., Yaremchuk, A. & Tukalo, M. The 2 Å crystal structure of leucyl-tRNA synthetase and its complex with a leucyl-adenylate analogue. *EMBO J.* **19**, 2351–2361 (2000).

46. Gomez, M. A. R. & Ibba, M. Aminoacyl-tRNA Synthetases. *RNA* **26**, 910–936 (2020).

47. Khan, K., Baleanu-Gogonea, C., Willard, B., Gogonea, V. & Fox, P. L. 3-Dimensional architecture of the human multi-tRNA synthetase complex. *Nucleic Acids Res.* **48**, 8740–8754 (2020).

48. Guo, M. & Schimmel, P. Essential nontranslational functions of tRNA synthetases. *Nat. Chem. Biol.* **9**, 145–153 (2013).

49. Lo, W. S. *et al.* Human tRNA synthetase catalytic nulls with diverse functions. *Science (80-.).* **345**, 328–332 (2014).

50. Yao, P. & Fox, P. L. Aminoacyl-tRNA synthetases in medicine and disease. *EMBO Mol. Med.* **5**, 332–343 (2013).

51. Tzima, E. *et al.* VE-cadherin links tRNA synthetase cytokine to anti-angiogenic function. *J. Biol. Chem.* **280**, 2405–2408 (2005).

52. Han, J. M. *et al.* Leucyl-tRNA synthetase is an intracellular leucine sensor for the

mTORC1-signaling pathway. *Cell* **149**, 410–424 (2012).

53. Park, S. G., Schimmel, P. & Kim, S. Aminoacyl tRNA Synthetases and Their Connections To Disease. **105**, 11043–11049 (2008).

54. Zhou, Z., Sun, B., Nie, A., Yu, D. & Bian, M. Roles of Aminoacyl-tRNA Synthetases in Cancer. *Front. Cell Dev. Biol.* **8**, 1–12 (2020).

55. Antonellis, A. *et al.* Glycyl tRNA synthetase mutations in Charcot-Marie-Tooth disease type 2D and distal spinal muscular atrophy type V. *Am. J. Hum. Genet.* **72**, 1293–1299 (2003).

56. Vo, M.-N. *et al.* ANKRD16 prevents neuron loss caused by an editing-defective tRNA synthetase. *Nature* **557**, 510–515 (2018).

57. Lee, J. M. *et al.* Methionyl-tRNA Synthetase is a Useful Diagnostic Marker for Lymph Node Metastasis in Non-Small Cell Lung Cancer. *Yonsei Med. J.* **60**, 1005–1012 (2019).

58. Zhang, C. *et al.* YARS as an oncogenic protein that promotes gastric cancer progression through activating PI3K-Akt signaling. *J. Cancer Res. Clin. Oncol.* **146**, 329–342 (2020).

59. Shin, S.-H. *et al.* Implication of leucyl-tRNA synthetase 1 (LARS1) over-expression in growth and migration of lung cancer cells detected by siRNA targeted knock-down analysis. *Exp. Mol. Med.* **40**, 229–236 (2008).

60. Novoa, E. M. & Ribas de Pouplana, L. Speeding with control: Codon usage, tRNAs, and ribosomes. *Trends Genet.* **28**, 574–581 (2012).

61. Schimmel, P. The emerging complexity of the tRNA world: mammalian tRNAs beyond protein synthesis. *Nat. Rev. Mol. Cell Biol.* (2017) doi:10.1038/nrm.2017.77.

62. Pan, T. Modifications and functional genomics of human transfer RNA. *Cell Res.* 1–10 (2018) doi:10.1038/s41422-018-0013-y.

63. Chan, P. P. & Lowe, T. M. GtRNAdb: A database of transfer RNA genes detected in genomic sequence. *Nucleic Acids Res.* **37**, 93–97 (2009).

64. Chan, P. P. & Lowe, T. M. GtRNAdb 2.0: An expanded database of transfer RNA genes identified in complete and draft genomes. *Nucleic Acids Res.* **44**, D184–D189 (2016).

65. Novoa, E. M., Pavon-Eternod, M., Pan, T. & Ribas De Pouplana, L. A role for tRNA modifications in genome structure and codon usage. *Cell* **149**, 202–213 (2012).

66. Goodarzi, H. *et al.* Modulated Expression of Specific tRNAs Drives Gene Expression and Cancer Progression. *Cell* **165**, 1416–1427 (2016).

67. Pavon-Eternod, M. *et al.* tRNA over-expression in breast cancer and functional consequences. *Nucleic Acids Res.* **37**, 7268–7280 (2009).

68. Presnyak, V. *et al.* Codon optimality is a major determinant of mRNA stability. *Cell* **160**, 1111–1124 (2015).

69. Gogakos, T. *et al.* Characterizing Expression and Processing of Precursor and Mature Human tRNAs by Hydro-tRNAseq and PAR-CLIP. *Cell Rep.* **20**, (2017).

70. Cozen, A. E. *et al.* ARM-seq: AlkB-facilitated RNA methylation sequencing reveals a complex landscape of modified tRNA fragments. *Nat. Methods* **12**, 879–884 (2015).

71. Zheng, G. *et al.* Efficient and quantitative high-throughput tRNA sequencing. *Nat. Methods* **12**, 835–837 (2015).

72. Akat, K. M. *et al.* Detection of circulating extracellular mRNAs by modified small-RNA-sequencing analysis. *JCI Insight* **4**, (2019).

73. Shi, J. *et al.* PANDORA-seq expands the repertoire of regulatory small RNAs by overcoming RNA modifications. *Nat. Cell Biol.* **23**, 424–436 (2021).

74. Shigematsu, M. *et al.* YAMAT-seq: An efficient method for high-throughput sequencing

of mature transfer RNAs. *Nucleic Acids Res.* **45**, e70 (2017).

75. Erber, L. *et al.* LOTTE-seq (Long hairpin oligonucleotide based tRNA high-throughput sequencing): specific selection of tRNAs with 3'-CCA end for high-throughput sequencing. *RNA Biol.* **17**, 23–32 (2020).

76. Pang, Y. L. J., Abo, R., Levine, S. S. & Dedon, P. C. Diverse cell stresses induce unique patterns of tRNA up- and down-regulation: tRNA-seq for quantifying changes in tRNA copy number. *Nucleic Acids Res.* **42**, (2014).

77. Katibah, G. E. *et al.* Broad and adaptable RNA structure recognition by the human interferon-induced tetratricopeptide repeat protein IFIT5. *Proc. Natl. Acad. Sci. U. S. A.* **111**, 12025–12030 (2014).

78. Qin, Y. *et al.* High-throughput sequencing of human plasma RNA by using thermostable group II intron reverse transcriptases. *Rna* **22**, 111–128 (2016).

79. Behrens, A., Rodschinka, G. & Nedialkova, D. D. High-resolution quantitative profiling of tRNA abundance and modification status in eukaryotes by mim-tRNAseq. *Mol. Cell* **81**, 1802-1815.e7 (2021).

80. Dittmar, K. A., Goodenbour, J. M. & Pan, T. Tissue-specific differences in human transfer RNA expression. *PLoS Genet.* **2**, 2107–2115 (2006).

81. Evans, M. E., Clark, W. C., Zheng, G. & Pan, T. Determination of tRNA aminoacylation levels by high-throughput sequencing. *Nucleic Acids Res.* **45**, e133 (2017).

82. Dittmar, K. A., Sørensen, M. A., Elf, J., Ehrenberg, M. & Pan, T. Selective charging of tRNA isoacceptors induced by amino-acid starvation. *EMBO Rep.* **6**, 151–157 (2005).

83. Zaborske, J. M. *et al.* Genome-wide analysis of tRNA charging and activation of the eIF2 kinase Gcn2p. *J. Biol. Chem.* **284**, 25254–25267 (2009).

84. Lee, S. R. & Collins, K. Starvation-induced cleavage of the tRNA anticodon loop in Tetrahymena thermophila. *J. Biol. Chem.* **280**, 42744–42749 (2005).

85. Fu, H. *et al.* Stress induces tRNA cleavage by angiogenin in mammalian cells. *FEBS Lett.* **583**, 437–42 (2009).

86. Thompson, D. M., Lu, C., Green, P. J. & Parker, R. tRNA cleavage is a conserved response to oxidative stress in eukaryotes. *RNA* **14**, 2095–2103 (2008).

87. Thompson, D. M. & Parker, R. Stressing Out over tRNA Cleavage. *Cell* **138**, 215–219 (2009).

88. Goodarzi, H. *et al.* Endogenous tRNA-derived fragments suppress breast cancer progression via YBX1 displacement. *Cell* **161**, 790–802 (2015).

89. Yu, X. *et al.* tRNA-derived fragments: Mechanisms underlying their regulation of gene expression and potential applications as therapeutic targets in cancers and virus infections. *Theranostics* **11**, 461–469 (2020).

90. Huh, D. *et al.* A stress-induced tyrosine-tRNA depletion response mediates codon-based translational repression and growth suppression. *EMBO J.* **40**, 1–16 (2021).

91. Kim, H. K. *et al.* A transfer-RNA-derived small RNA regulates ribosome biogenesis. *Nature* **552**, 57–62 (2017).

92. Ivanov, P., Emara, M. m, Villen, J., Gygi, S. P. & Anderson, P. Angiogenin-induced tRNA fragments inhibit translation initiation. *Mol. Cell* **43**, 613–623 (2011).

93. Li, M. *et al.* DNA damage-induced cell death relies on SLFN11-dependent cleavage of distinct type II tRNAs. *Nat. Struct. Mol. Biol.* **25**, (2018).

94. Komarov, P. G. *et al.* A Chemical Inhibitor of p53 That Protects Mice from the Side Effects of Cancer Therapy. *Science (80-.).* **285**, 1733 LP – 1737 (1999).

95. Testa, G. *et al.* A Reliable lacZ Expression Reporter Cassette for Multipurpose, Knockout-First Alleles. *Genesis* **38**, 151–158 (2004).

96. Tavora, B. *et al.* Tumoural activation of TLR3–SLIT2 axis in endothelium drives metastasis. *Nature* **586**, 299–304 (2020).

97. Padmanaban, V. *et al.* Organotypic culture assays for murine and human primary and metastatic-site tumors. *Nat. Protoc.* **15**, 2413–2442 (2020).

98. Lund, Elsebet, Dahlberg, J. E. Proofreading and Aminoacylation of tRNAs before Export from the Nucleus. *Science (80-.).* **282**, 2082–2085 (1998).

99. Elf, J., Nilsson, D., Tenson, T. & Ehrenberg, M. Selective charging of tRNA isoacceptors explains patterns of codon usage. *Science (80-.).* **300**, 1718–1722 (2003).

100. Gilbert, L. A. *et al.* Genome-Scale CRISPR-Mediated Control of Gene Repression and Activation Luke. **159**, 647–661 (2014).

101. Hornberger, Troy Alan, Sukhija, K. B., Wang, X.-R. & Chien, S. mTOR is the Rapamycin-Sensitive Kinase that Confers Mechanically-Induced Phosphorylation of the Hydrophobic Motif Site Thr(389) in p70S6k Troy. *FEBS Lett.* **581**, 4562–4566 (2007).

102. Hutchinson, J. A., Shanware, N. P., Chang, H. & Tibbetts, R. S. Regulation of ribosomal protein S6 phosphorylation by casein kinase 1 and protein phosphatase 1. *J. Biol. Chem.* **286**, 8688–8696 (2011).

103. Kim, J. H. *et al.* Control of leucine-dependent mTORC1 pathway through chemical intervention of leucyl-tRNA synthetase and RagD interaction. *Nat. Commun.* **8**, 1–16 (2017).

104. Sanz, E. *et al.* Cell-type-specific isolation of ribosome-associated mRNA from complex tissues. *Proc. Natl. Acad. Sci.* **106**, 13939–13944 (2009).

105. McGlincy, N. J. & Ingolia, N. T. Transcriptome-wide measurement of translation by ribosome profiling. *Methods* **126**, 112–129 (2017).

106. Zecha, J. *et al.* TMT labeling for the masses: A robust and cost-efficient, in-solution labeling approach. *Mol. Cell. Proteomics* **18**, 1468–1478 (2019).

107. Wang, Y. W., Cheng, H. L., Ding, Y. R., Chou, L. H. & Chow, N. H. EMP1, EMP 2, and EMP3 as novel therapeutic targets in human cancer. *Biochim. Biophys. Acta - Rev. Cancer* **1868**, 199–211 (2017).

108. Alaminos, M. *et al.* EMP3, a myelin-related gene located in the critical 19q13.3 region, is epigenetically silenced and exhibits features of a candidate tumor suppressor in glioma and neuroblastoma. *Cancer Res.* **65**, 2565–2571 (2005).

109. Wang, W. *et al.* Effector T Cells Abrogate Stroma-Mediated Chemoresistance in Ovarian Cancer. *Cell* **165**, 1092–1105 (2016).

110. Ashburner, M. *et al.* Gene Ontology: tool for the unification of biology. *Nat. Genet.* **25**, 25–29 (2000).

111. Nicassio, F. *et al.* Human USP3 is a chromatin modifier required for S phase progression and genome stability. *Curr. Biol.* **17**, 1972–1977 (2007).

112. Munz, M., Baeuerle, P. & Gires, O. The emerging role of EpCAM in cancer and stem cell signaling. *Cancer Res.* **69**, 5627–5629 (2009).

113. Paton, C. M. & Ntambi, J. Loss of stearoyl-CoA desaturase activity leads to free cholesterol synthesis through increased Xbp-1 splicing. *Am J Physiol Endocrinol Metab* **299**, E1066-e1075 (2010).

114. Lauria, F. *et al.* riboWaltz: Optimization of ribosome P-site positioning in ribosome profiling data. *PLoS Comput. Biol.* **14**, 1–20 (2018).

115. Wu, C. C., Zinshteyn, B., Wehner, K. A. & Green, R. High-resolution ribosome profiling defines discrete ribosome elongation states and translational regulation during cellular stress. *Mol. Cell* **73**, 959–970 (2019).

116. Paushkin, S. V., Patel, M., Furia, B. S., Peltz, S. W. & Trotta, C. R. Identification of a human endonuclease complex reveals a link between tRNA splicing and pre-mRNA 3′ end formation. *Cell* **117**, 311–321 (2004).

117. Hopper, A. K. & Nostramo, R. T. TRNA processing and subcellular trafficking proteins multitask in pathways for other RNAs. *Front. Genet.* **10**, 1–14 (2019).

118. Weitzer, S. & Martinez, J. The human RNA kinase hClp1 is active on 3′ transfer RNA exons and short interfering RNAs. *Nature* **447**, 222–226 (2007).

119. Haussecker, D. *et al.* Human tRNA-derived small RNAs in the global regulation of RNA silencing. *Rna* **16**, 673–695 (2010).

120. Couvillion, M. T., Sachidanandam, R. & Collins, K. A growth-essential Tetrahymena Piwi protein carries tRNA fragment cargo. *Genes Dev.* **24**, 2742–2747 (2010).

121. Mili, S. & Steitz, J. A. Evidence for reassociation of RNA-binding proteins after cell lysis: Implications for the interpretation of immunoprecipitation analyses. *Rna* **10**, 1692–1694 (2004).

122. Ule, J. *et al.* CLIP Identifies Nova-Regulated RNA Networks in the Brain. *Science (80-.).* **302**, 1212–1215 (2003).

123. Hafner, M. *et al.* Transcriptome-wide identification of RNA-binding protein and microRNA target sites by PAR-CLIP. *Cell* **141**, 129–141 (2010).

124. Licatalosi, D. D. *et al.* HITS-CLIP yields genome-wide insights into brain alternative RNA processing. *Nature* **456**, 464–469 (2008).

125. Chi, S. W., Zang, J. B., Mele, A. & Darnell, R. B. Argonaute HITS-CLIP decodes microRNA-mRNA interaction maps. *Nature* **460**, 479–486 (2009).

126. Huelga, S. C. *et al.* Integrative Genome-wide Analysis Reveals Cooperative Regulation of Alternative Splicing by hnRNP Proteins. *Cell Rep.* **1**, 167–178 (2012).

127. Glisovic, T., Söderberg, M., Christian, K., Lang, M. & Raffalli-Mathieu, F. Interplay between transcriptional and post-transcriptional regulation of Cyp2a5 expression. *Biochem. Pharmacol.* **65**, 1653–1661 (2003).

128. Wang, H. *et al.* hnRNP A1 antagonizes cellular senescence and senescence-associated secretory phenotype via regulation of SIRT1 mRNA stability. *Aging Cell* **15**, 1063–1073 (2016).

129. Biamonti, G. *et al.* Human hnRNP protein A1 gene expression. Structural and functional characterization of the promoter. *J. Mol. Biol.* **230**, 77–89 (1993).

130. Roy, R., Huang, Y., Seckl, M. J. & Pardo, O. E. Emerging roles of hnRNPA1 in modulating malignant transformation. *Wiley Interdiscip. Rev. RNA* **8**, (2017).

131. Yoo, C. J. & Wolin, S. L. The yeast La protein is required for the 3' endonucleolytic cleavage that matures tRNA precursors. *Cell* **89**, 393–402 (1997).

132. Gottlieb, E. & Steitz, J. A. Function of the mammalian La protein: evidence for its action in transcription termination by RNA polymerase III. *EMBO J.* **8**, 851–861 (1989).

133. Maraia, R. J., Kenan, D. J. & Keene, J. D. Eukaryotic transcription termination factor La mediates transcript release and facilitates reinitiation by RNA polymerase III. *Mol. Cell. Biol.* **14**, 2147–2158 (1994).

134. Hanada, T. *et al.* The RNA kinase CLP1 links tRNA metabolism to progressive motor neuron loss. *Nature* **495**, 474–480 (2013).

135. Xu, Y. *et al.* Translation control of the immune checkpoint in cancer and its therapeutic targeting. *Nat. Med.* **25**, 301–311 (2019).

136. McFarland, M. R. *et al.* The molecular aetiology of tRNA synthetase depletion: induction of a GCN4 amino acid starvation response despite homeostatic maintenance of charged tRNA levels. *Nucleic Acids Res.* **48**, 3071–3088 (2020).

137. Holecek, M. Branched-chain amino acids in health and disease: metabolism, alterations in blood plasma, and as supplements. *Nutr. Metab. (Lond).* **15**, (2018).

138. Dong, J., Qiu, H., Garcia-Barrio, M., Anderson, J. & Hinnebusch, A. G. Uncharged tRNA activates GCN2 by displacing the protein kinase moiety from a bipartite tRNA-binding domain. *Mol. Cell* **6**, 269–279 (2000).

139. Anthony, T. G. *et al.* Preservation of liver protein synthesis during dietary leucine deprivation occurs at the expense of skeletal muscle mass in mice deleted for eIF2 kinase GCN2. *J. Biol. Chem.* **279**, 36553–36561 (2004).

140. Averous, J. *et al.* GCN2 contributes to mTORC1 inhibition by leucine deprivation through an ATF4 independent mechanism. *Sci. Rep.* **6**, 1–10 (2016).

141. Xiao, F. *et al.* Leucine deprivation increases hepatic insulin sensitivity via GCN2/mTOR/S6K1 and AMPK pathways. *Diabetes* **60**, 746–756 (2011).

142. Li, Y., Corradetti, M. N., Inoki, K. & Guan, K.-L. TSC2: filling the GAP in the mTOR signaling pathway. *Trends Biochem. Sci.* **29**, 32–38 (2004).

143. Chang, H., Triboulet, R., Thornton, J. E. & Gregory, R. I. A role for the Perlman syndrome exonuclease Dis3l2 in the Lin28-let-7 pathway. *Nature* **497**, 244–248 (2013).

144. Towler, B. P. *et al.* Dis3L2 regulates cell proliferation and tissue growth though a conserved mechanism. *PLoS Genet.* **16**, 1–29 (2020).

145. Hunter, R. W. *et al.* Loss of Dis3l2 partially phenocopies perlman syndrome in mice and results in upregulation of Igf2 in nephron progenitor cells. *Genes Dev.* **32**, 903–908 (2018).

146. Labun, K. *et al.* CHOPCHOP v3: Expanding the CRISPR web toolbox beyond genome editing. *Nucleic Acids Res.* **47**, W171–W174 (2019).

147. Gandin, V. *et al.* Polysome fractionation and analysis of mammalian translatomes on a genome-wide scale. *J. Vis. Exp.* 1–9 (2014) doi:10.3791/51455.

148. Hickernell, F. J. Quadrature Error Bound. *Math. Comput.* **67**, 299–322 (1998).

149. Tyanova, S. *et al.* The Perseus computational platform for comprehensive analysis of (prote)omics data. *Nat. Methods* **13**, 731–740 (2016).

150. Wagner, K. U. *et al.* Cre-mediated gene deletion in the mammary gland. *Nucleic Acids Res.* **25**, 4323–4330 (1997).